Global analysis of time-resolved fluorescence microspectroscopy and applications in biomolecular studies

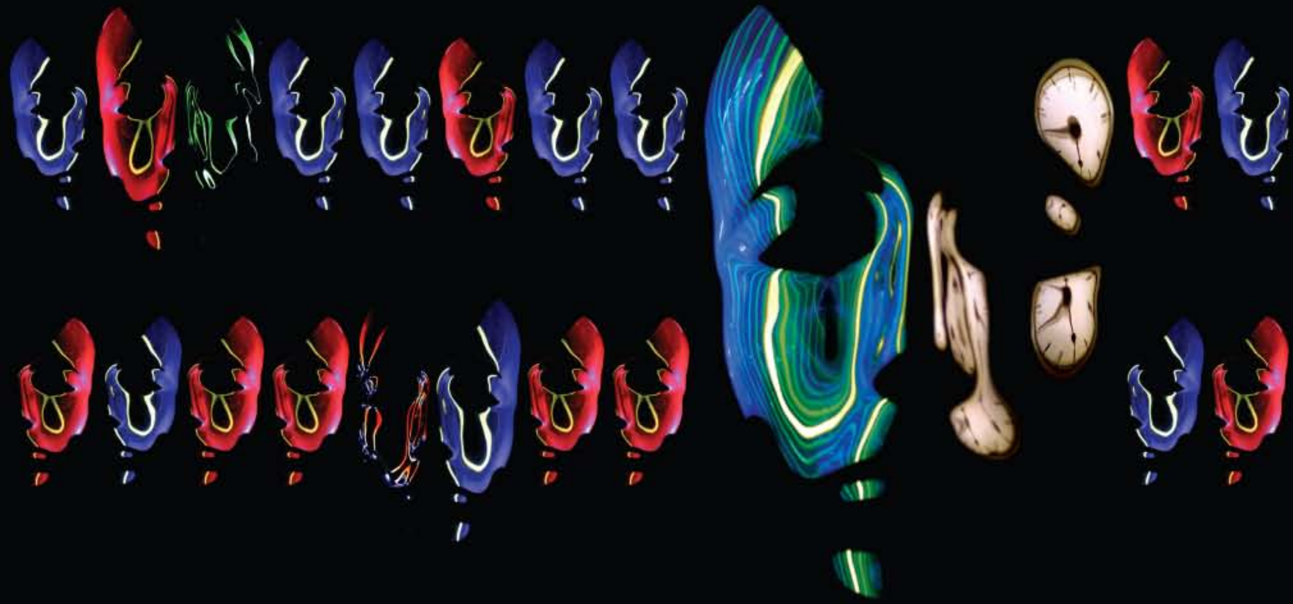

Sergey P. Laptenok

Global analysis of time-resolved fluorescence microspectroscopy
and
applications in biomolecular studies

Promotoren:
Prof. Dr. H. van Amerongen
Hoogleraar Biofysica
Wageningen Universiteit, Nederland

Prof. Dr. A.J.W.G. Visser
Emeritus hoogleraar in de Biochemische Microspectroscopie
Wageningen Universiteit, Nederland

Co-promotor:
Dr. I.H.M. van Stokkum
Universitair Docent
Vrije Universiteit Amsterdam, Nederland

Promotiecommissie:
Prof. Dr. L.J. van Vliet (Technische Universiteit Delft, Nederland)
Prof. Dr. M. Janson (Wageningen Universiteit, Nederland)
Prof. Dr. V.V. Apanasovich (Belarussian State University, Belarus)
Dr. M.A.M.J. van Zandvoort (Universiteit Maastricht, Nederland)

Dit onderzoek is uitgevoerd binnen de onderzoeksschool VLAG.

Global analysis of time-resolved fluorescence microspectroscopy and applications in biomolecular studies

Sergey P. Laptenok

Proefschrift
ter verkrijging van de graad van doctor
op gezag van de rector magnificus
van Wageningen Universiteit,
Prof. Dr. M. J. Kropff,
in het openbaar te verdedigen
op donderdag 11 juni 2009
des voormiddags te elf uur in de Aula

Sergey P. Laptenok, 2009
Global analysis of time-resolved fluorescence microspectroscopy and applications in biomolecular studies
PhD thesis, Wageningen Universiteit, Nederland
met een samenvatting in het Nederlands

ISBN: 978-90-8585-389-3

“Do not allow your soul to idle
In order not to mill the wind
The soul is bound to labor
Day and night, day and night “

Nikolai Zabolotsky

Contents

Chapter 1 1
General Introduction

Chapter 2 19
Structural changes of yellow cameleon domains observed by quantitative FRET analysis and polarized fluorescence correlation spectroscopy

Chapter 3 49
Picosecond fluorescence spectroscopy of the calcium sensor YC3.60

Chapter 4 61
Fluorescence Lifetime Imaging Microscopy (FLIM) data analysis with TIMP

Chapter 5 81
Global analysis of Förster resonance energy transfer in live cells measured by fluorescence lifetime imaging microscopy exploiting the rise time of acceptor fluorescence

Chapter 6 101
Summarizing discussion

Acknowledgements 110

Curriculum Vitae 112

Overview of completed training activities 113

Chapter 1

General Introduction

Background and aim

Understanding the properties of biomolecular networks is of central importance in life sciences. Optical microscopy has been very useful to determine the sub-cellular localisation of proteins but it cannot reveal whether proteins interact with one another. Micro-spectroscopic techniques (combining microscopy with spectroscopy) can provide direct information on molecular interactions and dynamic events involving biomolecules with minimal perturbation of cellular integrity and function and they are particularly useful for studying live cells. Over the last few years the spatial-temporal resolution and sensitivity of these techniques have improved considerably. Detecting protein-protein interactions within a biological cell can lead to a greater understanding of the key mechanisms that regulate the fundamental processes of the cell. However, analysis of fluorescence microspectroscopy data is not a trivial task. Well-designed data analysis techniques could significantly improve the interpretation of parameters and characteristics of photophysical processes in complex molecular systems. The most commonly used methods of time-resolved spectroscopic data analysis are, respectively, nonlinear least squares, deconvolution, global analysis and maximum entropy. These methods often lead to a good description of the data but do not necessarily provide physically relevant parameters. The aim of this thesis is to develop new multidimensional fluorescence analysis methods dedicated to improve the visualization and the quantitative analysis and physical interpretation of complex spectral, spatial and time-resolved data sets.

The purpose of this chapter is to provide an introduction to different microspectroscopic techniques and their applications as well as to basic principles of the analysis of the various time-resolved fluorescence data.

1.1 Basic principles and parameters of fluorescence

Fluorescence spectroscopy and microscopy provide powerful tools, which allow to study the structure and dynamics of molecular systems. These techniques use the sensitivity of fluorescence properties to the micro-environment of the fluorophore to obtain important information about the investigated system. The diversity of the physical parameters, which can be studied by fluorescence, is remarkable: inter- and intra-molecular distances, polarity, viscosity, structural ordering, molecular mobility, electric potential (Valeur 2002).

Schematically, the processes that can occur in the chromophore after absorption of a photon can be illustrated in a Jablonski energy diagram (Jabłoński 1935). This diagram shows different energetic states of a chromophore where transitions between different states are depicted with arrows (Figure 1).

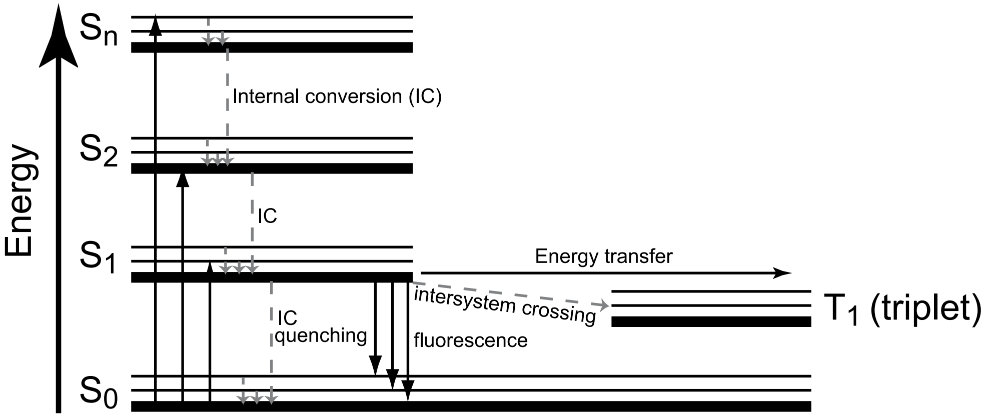

Figure 1. *The Jablonski energy diagram. Light absorption and emission are represented by vertical, black arrows. Vibrational relaxation, internal conversion and intersystem crossing are indicated by light gray dashed arrows.*

Absorption of a photon by a fluorophore leads to the transition of an electron from the ground state (S_0) to an excited state (S_n). The excitation then rapidly (10^{-13} s) relaxes non-radiatively to the lowest excited state (S_1) via vibrational relaxation and internal conversion (IC). From S_1 the fluorophore can then relax to S_0 in several ways: non-radiatively by IC, by intersystem crossing forming a triplet state, by photochemical quenching, by energy transfer to another fluorophore or by fluorescence (emission of a photon). The energy spacing between the ground state and the first electronic excited state determines the wavelengths of absorption and emission. Another photophysical property of these fluorophores is the average time in the excited state, called the fluorescence lifetime (τ) and is given as a function of the radiative (k_r), non-radiative (k_{nr}) and energy transfer (k_t) rate constants. The fluorescence lifetime is strongly affected by the properties of the local environment, for example the refractive index (Borst et al. 2005), or by interaction with another molecule through quenching or Förster resonance energy transfer (FRET) (Lakowicz 1999; Valeur 2002). Therefore, fluorescence lifetime measurements can be used to obtain information on the rate constants of the processes shown in figure 1.

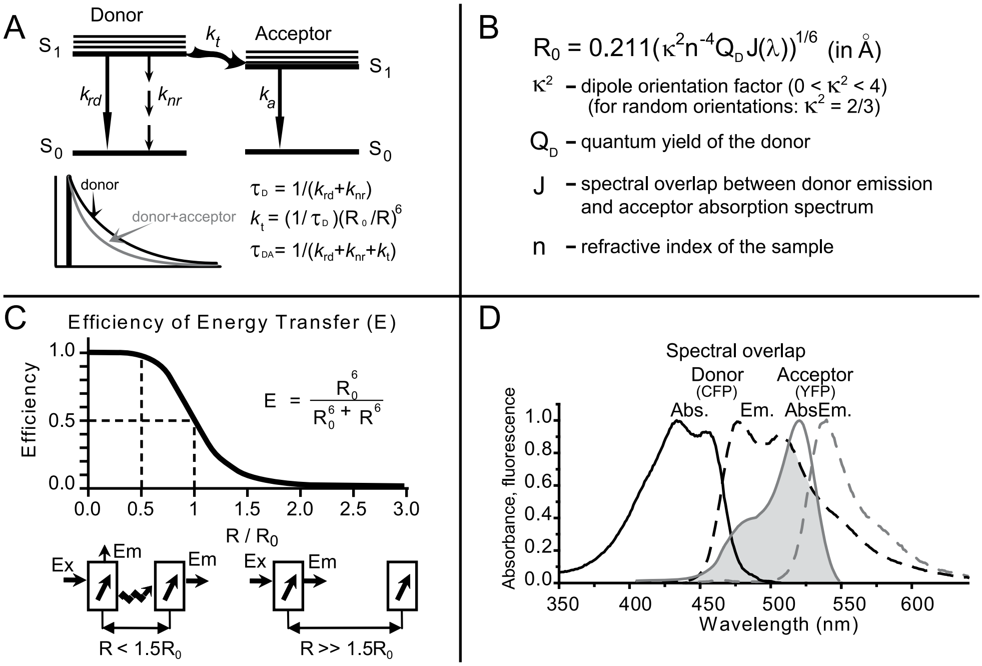
A
Donor
Acceptor
S_1
S_0
k_t
k_{rd}
k_{nr}
k_a
donor
donor+acceptor
$\tau_D = 1/(k_{rd}+k_{nr})$
$k_t = (1/\tau_D)(R_0/R)^6$
$\tau_{DA} = 1/(k_{rd}+k_{nr}+k_t)$
B
$R_0 = 0.211(\kappa^2 n^{-4} Q_D J(\lambda))^{1/6}$ (in Å)
κ^2 – dipole orientation factor ($0 \leq \kappa^2 < 4$)
(for random orientations: $\kappa^2 = 2/3$)
Q_D – quantum yield of the donor
J – spectral overlap between donor emission and acceptor absorption spectrum
n – refractive index of the sample
C
Efficiency of Energy Transfer (E)
Efficiency
1.0
0.5
0.0
0.0 0.5 1 1.5 2.0 2.5 3.0
R / R_0
$E = \frac{R_0^6}{R_0^6 + R^6}$
Ex
Em
Em
Ex
Em
$R < 1.5R_0$
$R >> 1.5R_0$
D
Spectral overlap
Donor (CFP)
Acceptor (YFP)
Abs.
Em.
AbsEm.
Absorbance, fluorescence
1.0
0.8
0.6
0.4
0.2
0.0
350 400 450 500 550 600
Wavelength (nm)

***Figure 2**. Summary of the FRET principles. When donor and acceptor are in a close proximity energy transfer can take place which leads to an additional possible relaxation path for the excited donor molecule (k_t). The transfer rate can be related to the distance r between donor and acceptor. (A). The Förster distance (R_0) is determined by the relevant spectroscopic properties of the participating fluorophores (B). The requirements for FRET to occur are: a small distance R between donor and acceptor and a finite value of the orientation factor (C), spectral overlap between fluorescence emission spectrum of donor fluorophore and absorption spectrum of the acceptor fluorophore (D).*

FRET measurements allow one to obtain a spatial resolution that is far below the optical diffraction limit. The theory for resonance energy transfer was developed by Theodor Förster and was published in 1948 (Förster 1948). FRET is a photophysical process in which the excited-state energy of a donor fluorophore is non-radiatively transferred with rate constant (k_t) to an acceptor molecule in its ground state via dipole-dipole interaction. There are several requirements for FRET to occur. One is spectral overlap between the fluorescence emission spectrum of the donor fluorophore and the absorption spectrum of the acceptor fluorophore. Furthermore transfer only occurs when interacting molecules are within a small distance of each other, typically less than 10 nm. The transfer rate is proportional to the inverse 6th power of the distance *R* between donor and acceptor, which makes it an extremely sensitive parameter for obtaining distances between 1 and 10 nm. The distance at which the excitation is transferred to the acceptor with probability 0.5, i.e. $k_t = k_D$, is called the Förster distance R_0, and can be calculated using the relevant spectroscopic properties of the participating fluorophores. The theory of FRET is summarized in figure 2.

Another fluorescence parameter, which is sensitive to the orientation of the fluorophore is the fluorescence anisotropy. The experimental setups for anisotropy measurements make use of excitation with polarized light and detection of the fluorescence via a polarizer, the polarization of which is oriented either parallel or perpendicular with respect to the polarization of the excitation. Fluorescence anisotropy is defined as the ratio of the difference between the fluorescence emission intensity detected parallel (I_{par}) and perpendicular (I_{per}) with respect to the excitation light polarization (I_{par} - I_{per}), divided by (I_{par} + $2I_{per}$), which is proportional to the total (polarization independent) fluorescence intensity (Lakowicz 1999; Valeur 2002).

Time-resolved fluorescence anisotropy measurements supply information about molecular dynamics and energy transfer between chromophores. The rotational diffusion motion of a molecule, which takes place during the time that a molecule resides in the excited state, is one source of depolarization. The rate of depolarization that can be detected in time-resolved anisotropy measurements, depends on the size and shape of the molecule as well as on the viscosity of the environment. Energy transfer between molecules or internal molecular reorientation are other sources of depolarization that can be detected.

1.2 GFP technology

To monitor cellular processes with the use of FRET, one often uses various kinds of fluorescent proteins. An important example is the green fluorescent protein (GFP) from the jellyfish *Aequorea victoria*. The application of GFP technology has become very important for the imaging of intracellular proteins (Tsien 1998) and for their crucial contributions to this technology, Osamu Shimomura, Martin Chalfie and Roger Y. Tsien were awarded the Nobel Prize in chemistry in 2008. Several differently colored GFP mutants have now been developed and have found widespread application as natural, brightly fluorescent markers in cell biology. Currently, fluorescent proteins emitting from violet to red are available (Shaner et al. 2004;2005; Verkhusha and Lukyanov 2004; Tomosugi et al. 2009; Merzlyak et al. 2007; Subach et al. 2009). This allows for instance the tracking of differently labeled proteins simultaneously in the cell but different pairs of fluorescent proteins are also widely used as donor-acceptor pairs in FRET applications. So far, the enhanced forms of cyan fluorescent protein (ECFP) and yellow fluorescent protein (EYFP) are the most commonly used FRET pairs in cell biology and they also receive considerable attention in this thesis. Different biosensors based on GFP technology have been developed, like the 'cameleons' for in vivo measurements of concentrations of calcium, which is a very important ion in cellular signaling, since it acts as an essential second messenger. These genetically encoded fluorescent calcium indicators do not require any cofactors and are targetable to specific intracellular locations (Miyawaki et al. 1997; Miyawaki et al. 1999). An important Ca-biosensor is the so-called yellow cameleon (YCam) which consists of a tandem fusion of ECFP, a calmodulin domain having four calcium binding sites, a calmodulin binding peptide M13 and EYFP (Váradi and Rutter 2002) (figure 3). Binding of calcium ions makes calmodulin wrap around the M13 domain resulting in an increase of the FRET efficiency. Several variants of the cameleon sensors are currently available and are continuously being improved. The latest versions are pH independent and consist of the brighter EYFP variant Venus (Evanko and Haydon 2005; Nagai et al. 2004). The important benefit of YCams is that EYFP and ECFP fluorescence intensities can be measured simultaneously in two different detection channels of a fluorescence microscope. This enables ratio imaging so that relative calcium concentration changes can be measured in real time.

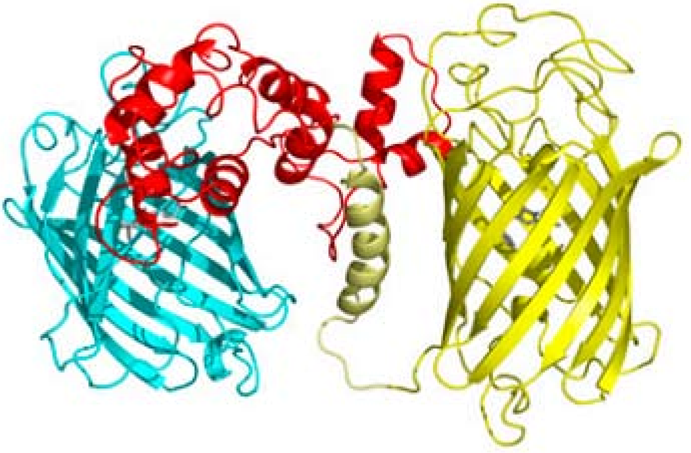

Figure 3. *Cartoon representation of YC3.60 in the calcium-free conformation. The left, cyan barrel (ECFP) is connected at the N-terminus of the red calmodulin part. The C terminus of the M13 peptide (gold) finally connects to the right, yellow barrel (Venus).*

1.3 Instruments and methods

Time-resolved fluorescence microscopy and spectroscopy techniques are widely used and form powerful experimental tools at the interface of biology, biochemistry and biophysics. They allow to obtain information about rate constants of various processes in complex systems (Jameson et al. 2003; Niggli and Egger 2004; Visser et al. 2005; Jares-Erijman and Jovin 2006; Tonaco et al. 2006; van Oort et al. 2009). There are two different techniques for measuring time-resolved fluorescence: time-domain and frequency-domain methods. Using frequency-domain methods, the sample is excited with intensity-modulated (typically sine-wave modulated) light. The emission is measured at the same modulation frequency. As a result of the finite fluorescence lifetime, the emission is delayed in time relative to the excitation light. This delay is measured as a phase shift which can then be used to calculate the excited-state lifetime. In time-domain methods, the sample is excited with a short light pulse. The fluorescence intensity is then measured as a function of time. Both methods have advantages and disadvantages. For principles and details see (Lakowicz 1999; Valeur 2002). Data described in this thesis were obtained using time-correlated single photon counting (TSCPC) and a synchroscan streak-camera system. Both methods are time-domain techniques and require excitation of the sample with a very short light pulse followed by measuring the fluorescence intensity as a function of time.

1.3.1 Time-correlated single photon counting (TCSPC)

Time-correlated single photon counting or single-photon timing (O'Connor and Phillips 1984; Lakowicz 1999; Birch and Imhof 2002; Valeur 2002) is based on the detection of single fluorescence photons after pulsed-light excitation. The time between the excitation pulse and the observed photon is measured and stored in the probability histogram of counts versus time. If the condition for detecting a single photon after excitation pulse is fulfilled, *i.e.* only one fluorescence photon per excitation pulse is detected and there are no photons coming from the sample during the "dead time" of the setup, the probability of detecting a photon in channel *i* is proportional to the fluorescence intensity at delay time *i*, meaning that the histogram of photon arrival times is proportional to the fluorescence intensity decay (figure 4). A filter or monochromator can be placed between sample and detector that allows detecting only fluorescence of a certain frequency (wavelength).

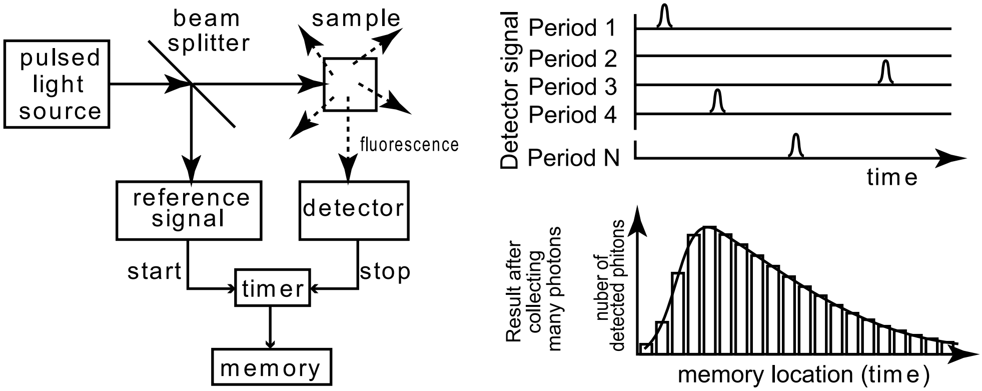

Figure 4. *Time-correlated single photon counting principle. The arrival time of the first photon after the excitation pulse is measured and stored in the memory. The histogram of the arrivals times of photons represents the fluorescence intensity versus time curve.*

In the setup that was used to perform TCSPC experiments described in this thesis the excitation pulses (repetition rate 76 MHz) are generated by a mode-locked Ti:Sapphire laser, pumped by a continuous solid state laser. The repetition rate was then reduced to 3.8 MHz with a pulse-picker, and the pulses were frequency-doubled. The maximum excitation pulse energy was in general below 1 pJ, with a pulse duration of about 300 fs and the light being vertically polarized. The fluorescence was detected at 90^o with respect to the excitation beam via band-pass filters with parallel and perpendicular polarization orientation.

A small part of the excitation pulse energy was directed to a fast photodiode, whose output was fed to one channel of a constant fraction discriminator (CFD) to generate a "stop" signal for the time-to-amplitude converter (TAC). A cooled microchannel plate photomultiplier (MCP) was used for the detection of the fluorescence photons. The amplified output of the MCP was analyzed by another channel of the CFD to generate a "start" signal for the

TAC. The output pulses of the TAC were converted by an analog-to-digital converter (ADC) and analyzed after gathering in the 4096 channels of a multichannel analyzer (MCA). The channel time spacing was either 2 ps or 5 ps. To prevent pile-up distortions, the energy of the excitation pulses was reduced by a neutral density filter to obtain a detection count rate of less than 30000 per second (≈ 1% of 3.8 MHz (Vos et al. 1987)). Also other instrumental sources for data distortion were minimized (van Hoek and Visser 1990). The dynamic instrument response function (IRF) of the setup was obtained from the fast single exponential decay of a reference fluorescence dye. The setup is described in more detail by Borst and coworkers (Borst et al. 2005).

1.3.2 Fluorescence lifetime imaging microscopy (FLIM)

In many cases the samples are spatially inhomogeneous, with differences in fluorescence in the various parts of the sample. In such cases bulk experiments provide only limited information and it is than more advantageous to combine TCSPC with microscopy. This combination leads to a setup called FLIM (Fluorescence Lifetime Imaging Microscopy). The use of genetically encoded visible fluorescent proteins coupled to proteins of interest allows the monitoring of the localization of specific proteins in cellular systems. By combining FRET with FLIM microscopy, methods have been developed in order to use the rate of FRET as a “spectroscopic ruler” to analyze protein interactions in biological systems (Stryer 1978; Jares-Erijman and Jovin 2006). The FLIM setup used in this thesis will be described below using experiments with plant protoplasts transfected with an enhanced variant of cyan fluorescence protein (ECFP). ECFP is widely used as a donor molecule in FRET studies. When FRET occurs, the donor fluorescence lifetime in the presence of an acceptor becomes shorter as compared to the fluorescence lifetime of donor-only case. The shortening of the donor fluorescence lifetime is an indicator of FRET, and the difference between the donor fluorescence lifetime with and without acceptor allows quantification of the FRET efficiency (Stryer 1978; Tramier et al. 2002; Wallrabe and Periasamy 2005). However, an accurate determination of the fluorescence lifetime of donor molecules in the absence of acceptor is still required.

In FLIM measurements, the excitation pulse is focused into a very small volume element of the sample (called voxel in three dimensions and pixel in two dimensions), and the resulting fluorescence is detected by a TCSPC detector. The excitation beam is scanned over the sample in the xy-plane and the fluorescence decay curve is recorded for every individual pixel. The FLIM setup used in this thesis uses two-photon excitation (TPE) to excite the sample. Maria Göppert-Mayer in 1931 (Göppert-Mayer 1931) has shown theoretically that energy of two quasi-simultaneous photons can bring a molecule to an excited state. To induce the TPE process, two photons have to interact with a pigment within approximately one femtosecond (10^{-15} s). The probability of TPE to occur is very small under most light conditions and requires special precautions, such that the photon density in time and space becomes sufficiently high. This can be achieved by using ultra-short, high-energy light pulses in a sharply focused laser beam. Although TPE requires some effort to achieve, it is worthwhile to pursue because of the following reasons. The penetration of the near-infrared light used in TPE is much deeper than that of visible light used in one-photon excitation microscopy

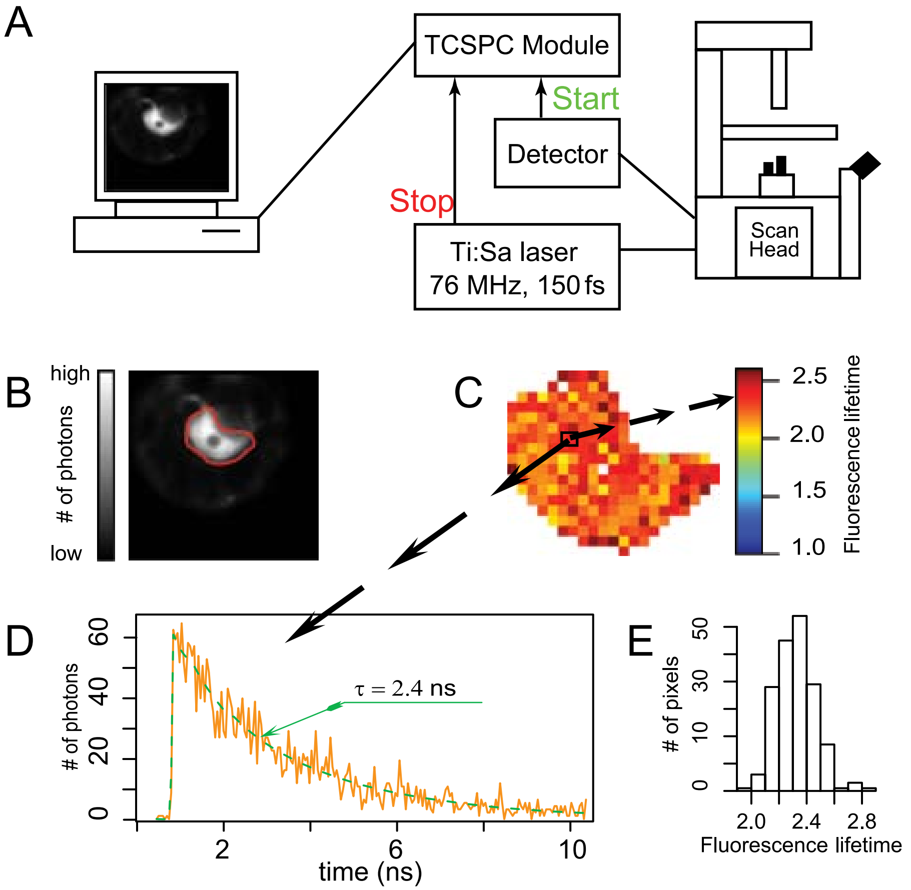
A
TCSPC Module
Start
Detector
Stop
Ti:Sa laser
76 MHz, 150 fs
Scan
Head
B
high
# of photons
low
C
2.5
2.0
1.5
1.0
Fluorescence lifetime
D
# of photons
0
20
40
60
τ = 2.4 ns
2
6
10
time (ns)
E
# of pixels
0
10
30
50
2.0
2.4
2.8
Fluorescence lifetime

Figure 5. *Schematic overview of the FLIM experiment (A) and analysis. A steady state fluorescence intensity image (B), results of analysis of the FLIM image color codes for the average fluorescence lifetime obtained from multi-exponential fit of traces from individual pixels (C), representative trace and fit result (E), frequency histogram of the average fluorescence lifetimes in C (D).*

(Piston 1999). The excitation occurs only in a small spot with the highest photon density and therefore no confocal pinhole is required. To obtain two-photon excitation a Ti:Sapphire laser pumped by a solid state laser is used to generate 150-femtosecond pulses with center wavelength 860 nm and repetition rate 76 MHz. The output of the laser is coupled into the microscope after the laser beam has been shaped and its power has been modulated by a beam conditioning unit. Excitation light is focused into the sample using a 60x objective lens. Fluorescence is detected by the same objective and separated from the excitation light by a dichroic mirror. Single photons are then detected via a non-descanned detector similar to the one used in the TCSPC experiments. In most cases, the images were recorded with a frame size of 64x64 pixels and 256 time channels resulting in a 48-ps/channel time interval. The total time-window was always 12.5 ns. The setup is described in more detail in chapter 5 and by Borst and co-workers (Borst et al. 2003).

Figure 5 shows a scheme of the FLIM experiment. The fluorescence intensity image of a plant protoplast transfected with ECFP after excitation with 860 nm light is depicted in figure 5B. The brightness of the pixel codes for the number of detected photons. In most cases it is wise to select a region for the analysis and this region is depicted by a contour in figure 5B. Figure 5D shows a representative trace from one of the pixels in the region of interest and results of fitting of this trace using a multi-exponential model. The results of fitting all traces from the region of interest is presented in figure 5C. The color reflects the average fluorescence lifetime for each pixel in the region of interest and the frequency of the average lifetimes is shown in the histogram. From this figure it is clear that the average fluorescence lifetimes are almost the same for all pixels within the selected region.

1.3.3 Streak-camera system

Another method to measure time-resolved fluorescence following pulsed excitation is via detection with a synchroscan streak camera. The advantage of this method is the simultaneous detection of the photon's wavelength and arrival time, allowing to monitor the evolution of whole spectra in time instead of measuring fluorescence decay at a single wavelength. Moreover, a streak camera has a better time resolution. The full-width-at-half-maximum (FWHM) of the IRF of the streak camera is 5-20 ps instead of 30-40 ps of the TCSPC setup. The main disadvantage of the streak camera is its relatively low sensitivity.

The principle of streak-camera detection is the following. Fluorescence photons induced by the excitation laser pulse are focused by an objective into a spectrograph, where they are deflected in a horizontal way by a grating. Separated in wavelength, the photons then hit a horizontal photocathode which produces photo-electrons. The photo-electrons are then accelerated by an electro-static field and deflected in the vertical direction by a periodical electric field (deflection field or sweep field). These accelerated and deflected photoelectrons are imaged by a 2D detector consisting of an microchannel plate (MCP) electron multiplier, a phosphor screen and a cooled CCD camera. The photoelectrons generated at different times experience different deflection fields and therefore hit the MCP at different vertical position (figure 6).

The excitation is performed by a set of lasers and optical amplifiers. In the setup used in this thesis a mode-locked Ti:Sapphire laser is used to generate short light pulses of 800 nm with duration of about 200 fs and repetition rate of 79.5 MHz. A small fraction of the output of this laser is used for synchronization with a sweep field, while the major part is fed into a regenerative amplifier (RegA), where the energy of the pulses is increased while the repetition rate is decreased to 250 kHz. The output of the RegA is directed to an optical parameter amplifier (OPA) which is used to produce excitation pulses of all wavelengths longer than 235 nm. The polarization of the excitation light is corrected by a polarizer and focused into the sample by a lens.

As an example of a streak image, figure 7A shows time-resolved spectra of ECFP. The image represents the fluorescence intensity as a function of time and wavelength. Light pulses of 400 nm were used for excitation of the sample. Every vertical column contains a

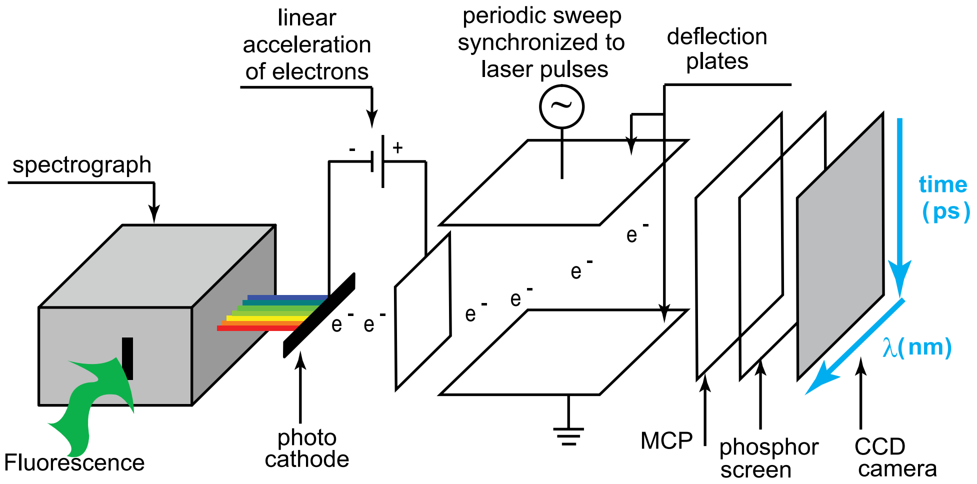
linear
acceleration
of electrons
periodic sweep
synchronized to
laser pulses
deflection
plates
spectrograph
- +
e -
e -
e - e -
e - e -
time
(ps)
λ(nm)
Fluorescence
photo
cathode
MCP
phosphor
screen
CCD
camera

***Figure 6**. Schematic representation of a streak camera.*

time trace of the fluorescence at the corresponding wavelength, whereas every horizontal line reflects a fluorescence emission spectrum after a certain delay time. A small part of the scattered excitation pulse is visible on the left part of the image as well as a Raman scatter peak around 460 nm. After several necessary steps of pre-processing, the image can be analyzed using various types of models; for more details see (van Stokkum et al. 2008). Figure 7B shows decay-associated spectra (DAS) and normalized DAS as the result of an analysis using a parallel decay scheme with 2 mono-exponentially decaying compartments. The DAS represent spectra of two conformations of the CFP chromophore which has lifetimes of 3.1 ns (major population) and 0.5 ns (minor population) (Hyun Bae et al. 2003; Borst et al. 2005). For more details about the analysis of time-resolved spectra using compartmental models see (van Stokkum et al. 2004).

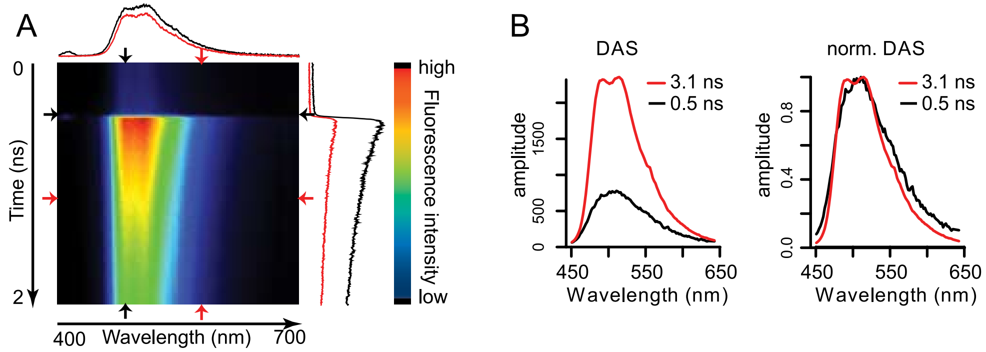

***Figure 7.** Time-resolved spectra of ECFP (A), DAS and normalized to maximum DAS resulting from global analysis of streak image from A (B).*

1.4 Data analysis

In the previous sections various experimental techniques of data collection were described. However, data analysis can be as important as data acquisition. The goal of the analysis is to obtain a description of the full dataset in terms of a small number of precisely estimated parameters. Mathematically, the core of the analysis is finding a global minimum of a function γ with the corresponding set of parameters $\mathbf{b} = (b_1 \ldots b_n)$:

$$\gamma(\mathbf{b}) = L(\psi, F(\mathbf{b})) \qquad (1)$$

with L – a mathematical operator for a function, which is sometimes called target criterion, ψ - the experimental data and $F(\mathbf{b})$- the simulated data obtained from an analytical function or simulation. In general, the time-resolved fluorescence can be fitted with a multi-exponential function convolved with an instrumental response function:

$$F(b) = \sum_i a_i \exp\left(-\frac{t}{\tau_i}\right) \otimes g(t) \qquad (2)$$

where the summation is over the number of components n_{comp} of the decay, $g(t)$ – the instrumental response function, and parameter vector **b** consists of n_{comp} pre-exponential factors a_i and n_{comp} fluorescence lifetimes τ_i.

There are several numerical optimization methods, which allow the minimization of function γ from eq. 1. They might be divided into two large groups: non-derivative methods, which do not require derivatives of the target fit criterion, and gradient methods, requiring derivatives of the target fit criterion. Among the non-derivative methods several classes are widely cited in the literature: Search methods perform a one-dimensional search with respect to each fit parameter (grid method, Hooke-Jeeves method, Powell method, Rosenbrock method) (Himmelblau 1970; Schwefel 1993). Simplex methods construct a polygon (simplex) in the space of fit parameters and move the center of this polygon to the parameter point where the target fit criterion value is the best (Nelder and Mead 1965). Stochastic methods use a search procedure based on a random determination of the search direction (random walk, Monte Carlo methods, method of simulated annealing etc.). Application of the gradient optimization methods in comparison with non-derivative methods ensures faster convergence to the optimum value but requires calculation of first or second derivative of the target fit criterion. The most frequently referenced gradient methods are steepest descent method, Gauss-Newton method, and Levenberg-Marquardt method (Johnson et al. 1985; Fletcher 1987; Bates and Watts 1988).

It has been found that for accurate separation of closely spaced parameters, the analysis of individual fluorescence curves is usually insufficient (Beechem et al. 1991). For the accurate analysis of complex phenomena it is advantageous to combine data from more than one measurement in one analysis. This simultaneous analysis of several related experimental datasets is commonly called global analysis. When some unknown parameters of interest are linked (assumed to be the same) between two or more datasets, the global analysis procedure has a significant advantage, since it increases the precision of the small number of estimated parameters that are estimated from all data (Beechem 1992). For global analysis, the fluorescence decay traces from n separate experiments can be stored as a matrix in which each column represents the fluorescence decay associated with a single experiment x_i, such that

$$\Psi = \left[\begin{array}{c|cccc} & x_1 & x_2 & \cdots & x_n \\ \hline t_1 & \psi(t_1,x_1) & \psi(t_1,x_2) & \cdots & \psi(t_1,x_n) \\ t_2 & \psi(t_2,x_1) & \psi(t_2,x_2) & \cdots & \psi(t_2,x_n) \\ \vdots & \vdots & \vdots & \ddots & \vdots \\ t_m & \psi(t_m,x_1) & \psi(t_m,x_2) & \cdots & \psi(t_m,x_n) \end{array}\right] \tag{3}$$

where $\Psi(t_i, x_j)$ is the fluorescence intensity at time t_i for experiment x_j.

Using a multi-exponential model for each decay trace, and using the assumption that the lifetimes are invariant between datasets associated with the different experiments, matrix $\mathbf{\Psi}$ can be modelled as

$$\mathbf{\Psi} = \mathbf{CE}^T = \sum_{i=1}^{n_{comp}} c_i a_i^T = \sum_{l=1}^{n_{comp}} (\exp(-t/\tau_i) \otimes g(t)) a_i^T \tag{4}$$

where column i of matrix $\mathbf{C}$ represents the time profile of component i of the fluorescence decay, and column i of matrix $\mathbf{A}$ represents the amplitude of component i in all experiments. The free parameters of the model are the n_{comp} lifetimes τ_i and for each experiment the n_{comp} amplitude parameters describing the fluorescence decay, composed in n_{comp} vectors a_i, each of length n. The parameter estimation problem associated with fitting the model for $\mathbf{\Psi}$ is an example of a separable nonlinear least squares optimization problem(Golub and Pereyra 2003). Under least square criteria the fitting problem can be written as

$$\min_{z \in R_q} \left\| \mathbf{\Psi} - \mathbf{C}(\theta)\mathbf{A}^T \right\|^2 \tag{5}$$

Matrix $\mathbf{A}$ contains parameters called conditionally linear parameters and they can be found by means of linear regression for known set of the parameters θ (Bates and Watts 1988). The variable projection algorithm developed by Golub and Pereyra (Golub and Pereyra 1973; Kaufman 1975) has many advantages over other techniques for separable nonlinear least squares problems and relies on analytically eliminating the conditionally linear amplitude parameters a_i from the residual function, meaning smaller number of parameters for standard nonlinear least square algorithms like Gauss-Newton or Levenberg-Marquardt methods. For more details see (van Stokkum et al. 2004; Mullen and van Stokkum 2007; Mullen et al. 2007). An application of the global analysis and variable projection algorithm for analysis of FLIM images will be discussed in more detail in chapters 4 and 5.

In spite of the fact that it is possible to fit time-resolved fluorescence data with a sufficient number of exponentials and corresponding amplitudes, the interpretation of the observed parameters is often difficult, implying that the mathematical parameters represent the data well but that they don't have a physical meaning. When *a priori* knowledge about a physical model is available, it is possible to analyze the data in terms of discrete physical models rather than relying on the empirical nature of the pre-exponential factors and decay rates derived from conventional deconvolution methods and this approach has been named target analysis by (Arcioni and Zannoni 1984). The combination of global and target analysis is a very powerful method for the analysis of complex problems (see chapter 3 and (Beechem et al. 1985; van Stokkum et al. 2004)).

The goal of the analysis of complicated photophysical phenomena is to obtain statistical models which can describe experimentally observed data to a satisfactory degree of accuracy; moreover the models should be well interpretable according to physico-chemical theory. This often requires an iterative process of model specification, parameter estimation, validation and adjustment of model.

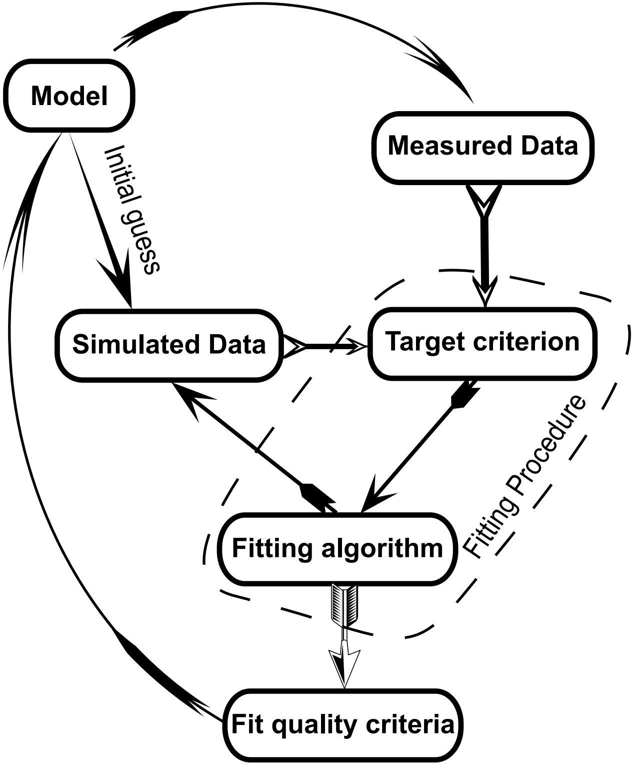

Figure 8. Scheme of iterative analysis

Figure 8 shows a possible scheme of data analysis. A candidate model for data analysis is selected based on *a priori* information about the dataset. The model fitting (insight loop) then provides a set of parameters, that is statistically most probable. In this thesis least squares criteria are used as target criteria and variable projection and Levenberg-Marquardt methods are used for the fitting algorithm. Validation of the model usually consists of the following steps: Examination whether the parameter estimates are precise enough based on the χ^2 criterion (Bevington and Robinson 2002) and analysis of the graphical statistical tests, *e.g.* plots of the weighted residuals, autocorrelation of weighted residuals, and singular vectors of the residual matrix (Hoff et al. 1994; van Stokkum et al. 2004). The next step then is the validation whether the estimated parameters are likely to be correct according to physico-chemical theories and, if necessary, adjustment of the candidate model, which brings one back to the fitting model stage or even to new measurements.

1.4 Outline of this thesis

The work in this thesis is concerned with the development, testing and application of new multidimensional fluorescence analysis protocols using global and target analysis of complex spectral, spatial and time-resolved data sets. Chapter 2 describes the usage of the rise time of the acceptor fluorescence upon donor excitation together with the analysis of the time-resolved fluorescence anisotropy for studying the FRET process and for obtaining structural information about the orientation of donor and acceptor molecules with respect to each other in the calcium sensor yellow cameleon. In chapter 3 the same experimental system is used to demonstrate the possibility of applying target analysis with both spectral and time-resolved measurements.

Chapters 4 and 5 demonstrate the possibilities of global and target analysis for analyzing FLIM images. The possibilities of global analysis and the variable projection algorithm for quantitative analysis of FLIM images with a typical low SNR were first tested on simulated datasets (chapter 4). The application of the global analysis for studying FRET processes *in vivo* based on the global analysis of images detected at two detection wavelengths is described in chapter 5.

The data analysis procedures described in this thesis have been implemented in the package **TIMP** for the “**R** project for Statistical Computing”. **TIMP** and **R** are freely available under the terms of the GNU General Public License (http://timp.r-forge.r-project.org). A Java-based graphical user interface (GUI) for the TIMP package is currently under development (http://timpgui.org). The GUI is meant for 1) simplifying the model specification for global and target analysis of time-resolved microspectroscopy data, 2) improving the interactivity of the analysis, using the scheme described in figure 8, and 3) visualization of the analysis results.

A summarizing discussion is presented in Chapter 6.

References

Arcioni, A. and C. Zannoni (1984). Intensity deconvolution in fluorescence depolarization studies of liquids, liquid crystals and membranes. *Chemical Physics* **88**(1): 113-128.

Bates, D. M. and D. G. Watts (1988). Nonlinear regression analysis and its applications. New York, John Wiley & Sons Inc.

Beechem, J., E. Gratton, M. Ameloot, J. Knutson and L. Brand (1991). The global analysis of fluorescence intensity and anisotropy decay data: second-generation theory and programs. In: Lakowicz, J. R. editor. Topics in Fluorescence Spectroscopy vol. 1: 241-305.

Beechem, J. M. (1992). Global analysis of biochemical and biophysical data. *Methods Enzymol* **210**:37-54.

Beechem, J. M., M. Ameloot and L. Brand (1985). Global and target analysis of complex decay phenomena. *Instrumentation Science & Technology* **14**(3): 379 - 402.

Bevington, P. R. and D. Keith Robinson (2002). Data reduction and error analysis for the physical sciences, McGraw-Hill Inc.,US.

Birch, D. J. S. and R. E. Imhof (2002). Time-domain fluorescence spectroscopy using time-correlated single-photon counting. In: Lakowicz, J. R. editor. Topics in Fluorescence Spectroscopy. vol. 1:1-88.

Borst, J. W., M. A. Hink, A. van Hoek and A. J. W. G. Visser (2003). Multiphoton microspectroscopy in living plant cells. *Proc. SPIE* **4963**:231-238.

Borst, J. W., M. A. Hink, A. van Hoek and A. J. Visser (2005). Effects of refractive index and viscosity on fluorescence and anisotropy decays of enhanced cyan and yellow fluorescent proteins. *J Fluoresc* **15**(2): 153-160.

Evanko, D. S. and P. G. Haydon (2005). Elimination of environmental sensitivity in a cameleon FRET-based calcium sensor via replacement of the acceptor with Venus. *Cell Calcium* **37**(4): 341-348.

Fletcher, R. (1987). Practical methods of optimization. New York, John Wiley & Sons Inc.

Förster, T. (1948). Zwischenmolekulare Energiewanderung und Fluoreszenz. *Ann. Phys.* **2**: 55-75.

Golub, G. and V. Pereyra (2003). Separable nonlinear least squares: the variable projection method and its applications. *Inverse Problems* **19**(2): R1-R26.

Golub, G. H. and V. Pereyra (1973). Differentiation of pseudo-inverses and nonlinear least-squares problems whose variables separate. *Siam Journal on Numerical Analysis* **10**(2): 413-432.

Göppert-Mayer, M. (1931). Über Elementarakte mit zwei Quantensprüngen. *Annalen der Physik* **401**(3): 273-294.

Himmelblau, D. M. (1970). Process analysis by statistical methods. New York, John Wiley & Sons, Inc.

Hoff, W. D., I. H. van Stokkum, H. J. van Ramesdonk, M. E. van Brederode, A. M. Brouwer, J. C. Fitch, T. E. Meyer, R. van Grondelle and K. J. Hellingwerf (1994). Measurement and global analysis of the absorbance changes in the photocycle of the photoactive yellow protein from Ectothiorhodospira halophila. *Biophys. J.* **67**(4): 1691-1705.

Hyun Bae, J., M. Rubini, G. Jung, G. Wiegand, M. H. J. Seifert, M. K. Azim, J.-S. Kim, A.

Zumbusch, T. A. Holak, L. Moroder, R. Huber and N. Budisa (2003). Expansion of the genetic code enables design of a novel “Gold” class of green fluorescent proteins. *J. Mol. Biol.* **328**(5): 1071-1081.

Jabłoński, A. (1935). Über den Mechanismus der Photolumineszenz von Farbstoffphosphoren. *Zeitschrift für Physik* **94**(1): 38-46.

Jameson, D. M., J. C. Croney and P. D. J. Moens (2003). Fluorescence: basic concepts, practical aspects, and some anecdotes. *Biophotonics*, Pt A **360**:1-43.

Jares-Erijman, E. A. and T. M. Jovin (2006). Imaging molecular interactions in living cells by FRET microscopy. *Cur. Opin. Chem. Biol.* **10**(5): 409-416.

Johnson, M. L. and S. G. Frasier (1985). Nonlinear least-squares analysis. *Methods Enzymol* **117**: 301-342.

Kaufman, L. (1975). A variable projection method for solving separable nonlinear least squares problems. *BIT Numerical Mathematics* **15**(1): 49-57.

Lakowicz, J. R. (2006). Principles of fluorescence spectroscopy 3rd edition, New York, Springer.

Merzlyak, E. M., J. Goedhart, D. Shcherbo, M. E. Bulina, A. S. Shcheglov, A. F. Fradkov, A. Gaintzeva, K. A. Lukyanov, S. Lukyanov, T. W. J. Gadella and D. M. Chudakov (2007). Bright monomeric red fluorescent protein with an extended fluorescence lifetime. *Nat Meth* **4**(7): 555-557.

Miyawaki, A., O. Griesbeck, R. Heim and R. Y. Tsien (1999). Dynamic and quantitative Ca^{2+} measurements using improved cameleons. *Proc. Natl. Acad. Sci. USA* **96**(5): 2135-2140.

Miyawaki, A., J. Llopis, R. Heim, J. M. McCaffery, J. A. Adams, M. Ikura and R. Y. Tsien (1997). Fluorescent indicators for Ca^{2+} based on green fluorescent proteins and calmodulin. *Nature* **388**(6645): 882-887.

Mullen, K. M. and I. H. M. van Stokkum (2007). TIMP: An R package for modeling multiway spectroscopic measurements. Journal of Statistical Software **18**(3).

Mullen, K. M., M. Vengris and I. H. Stokkum (2007). Algorithms for separable nonlinear least squares with application to modelling time-resolved spectra. *J. Global Optimization* **38**(2): 201-213.

Nelder, J. A. and R. Mead (1965). A simplex method for function minimization. *Comput. J.* **7**(4): 308-313.

Niggli, E. and M. Egger (2004). Applications of multi-photon microscopy in cell physiology. *Front Biosci* **9**:1598-610.

O’Connor, D. V. and D. Phillips (1984). Time-correlated single-photon counting. , London, Academic Press.

Piston, D. W. (1999). Imaging living cells and tissues by two-photon excitation microscopy. *Trends Cell Biol.* **9**(2): 66-69.

Rizzo, M. A., G. H. Springer, B. Granada and D. W. Piston (2004). An improved cyan fluorescent protein variant useful for FRET. *Nat Biotech* **22**(4): 445-449.

Schwefel, H.-P. P. (1993). Evolution and optimum seeking. New York, John Wiley & Sons.

Shaner, N. C., R. E. Campbell, P. A. Steinbach, B. N. G. Giepmans, A. E. Palmer and R. Y. Tsien (2004). Improved monomeric red, orange and yellow fluorescent proteins derived from Discosoma sp. red fluorescent protein. *Nat Biotech* **22**(12): 1567-1572.

Shaner, N. C., P. A. Steinbach and R. Y. Tsien (2005). A guide to choosing fluorescent proteins. *Nat Meth* **2**(12): 905-909.

Stryer, L. (1978). Fluorescence energy transfer as a spectroscopic Ruler. *An. Rev. Biochem.* **47**(1): 819-846.

Subach, F. V., G. H. Patterson, S. Manley, J. M. Gillette, J. Lippincott-Schwartz and V. V. Verkhusha (2009). Photoactivatable mCherry for high-resolution two-color fluorescence microscopy. *Nat Meth* **6**(2): 153-159.

Tonaco, I. A. N., J. W. Borst, S. C. de Vries, G. C. Angenent and R. G. H. Immink (2006). *In vivo* imaging of MADS-box transcription factor interactions. *J. Exp. Bot.* **57**: 33-42.

Tomosugi, W., T. Matsuda, T. Tani, T. Nemoto, I. Kotera, K. Saito, K. Horikawa and T. Nagai (2009). An ultramarine fluorescent protein with increased photostability and pH insensitivity. *Nat Meth* **6**(5): 351-353.

Tramier, M., I. Gautier, T. Piolot, S. Ravalet, K. Kemnitz, J. Coppey, C. Durieux, V. Mignotte and M. Coppey-Moisan (2002). Picosecond-hetero-FRET microscopy to probe protein-protein interactions in live cells. *Biophys. J.* **83**(6): 3570-3577.

Tsien, R. Y. (1998). The green fluorescent protein. *Annu. Rev. Biochem.* **67**(1): 509-544.

Valeur, B. (2002). Molecular fluorescence: principles and applications, Weinheim, Wiley-VCH Verlag GmbH.

van Hoek, A. and A. J. W. G. Visser (1990). Efficient method for the extraction of second harmonic light after extracavity frequency doubling. *Appl. Opt.* **29**(18): 2661-2663.

van Oort, B., S. Murali, E. Wientjes, R. B. M. Koehorst, R. B. Spruijt, A. van Hoek, R. Croce and H. van Amerongen (2009). Ultrafast resonance energy transfer from a site-specifically attached fluorescent chromophore reveals the folding of the N-terminal domain of CP29. *Chem. Phys*, **357**:113-119

van Stokkum, I. H. M., D. S. Larsen and R. van Grondelle (2004). Global and target analysis of time-resolved spectra. *Biochim. Biophys. Acta.* **1657**(2-3): 82-104.

van Stokkum, I. H. M., B. F. van Oort, F. van Mourik, B. Gobets and H. van Amerongen (2008). (Sub)-picosecond spectral evolution of fluorescence studied with a synchroscan streak-camera system and target analysis. Biophysical Techniques in Photosynthesis, . Dordrecht Springer Volume II.: 223 - 240.

Váradi, A. and G. A. Rutter (2002). Green fluorescent protein calcium biosensors. Calcium imaging with GFP cameleons. *Methods Mol. Biol.* **183**:255-264.

Verkhusha, V. V. and K. A. Lukyanov (2004). The molecular properties and applications of Anthozoa fluorescent proteins and chromoproteins. *Nat Biotech* **22**(3): 289-296.

Visser, N. V., J. W. Borst, M. A. Hink, A. van Hoek and A. J. W. G. Visser (2005). Direct observation of resonance tryptophan-to-chromophore energy transfer in visible fluorescent proteins. *Biophys. Chem.* **116**(3): 207-212.

Vos, K., A. van Hoek and A. J. W. G. Visser (1987). Application of a reference convolution method to tryptophan fluorescence in proteins - a refined description of rotational-dynamics. *Eur. J. Biochem.* **165**(1): 55-63.

Wallrabe, H. and A. Periasamy (2005). Imaging protein molecules using FRET and FLIM microscopy. *Cur. Opin. Biotech.* **16**(1): 19-27.

Chapter 2

Structural changes of yellow cameleon domains observed by quantitative FRET analysis and polarized fluorescence correlation spectroscopy

based on:
Borst, J. W., S. P. Laptenok, A. H. Westphal, R. Kühnemuth, H. Hornen, N. V. Visser, S. Kalinin, J. Aker, A. van Hoek, C. A. M. Seidel and A. J. W. G. Visser, 2008. "Structural Changes of Yellow Cameleon Domains Observed by Quantitative FRET Analysis and Polarized Fluorescence Correlation Spectroscopy." Biophys. J. 95(11): 5399-5411.

Abstract

Förster Resonance Energy Transfer (FRET) is a widely used method for monitoring interactions between or within biological macromolecules conjugated with suitable donor-acceptor pairs. Donor fluorescence lifetimes in absence and presence of acceptor molecules are often measured for the observation of FRET. However, these lifetimes may originate from interacting and non-interacting molecules, which hampers quantitative interpretation of FRET data. Here we describe a methodology for the detection of FRET that monitors the rise time of acceptor fluorescence upon donor excitation thereby detecting only those molecules undergoing FRET. The large advantage of this method, as compared to more commonly used donor fluorescence quenching method, is that the transfer rate of FRET can be accurately determined even in cases where the FRET efficiencies approach 100% yielding highly quenched donor fluorescence. Subsequently, the relative orientation between donor and acceptor chromophores is obtained from time-dependent fluorescence anisotropy measurements performed under identical conditions of donor excitation and acceptor detection. The FRET based calcium sensor Yellow Cameleon 3.60 (YC3.60) was used because it changes its conformation upon calcium binding, thereby increasing the FRET efficiency. After mapping distances and orientation angles between the FRET moieties in YC3.60, cartoon models of this FRET sensor with and without calcium could be created. Independent support for these representations came from experiments where the hydrodynamic properties of YC3.60 under ensemble and single-molecule conditions upon selective excitation of the acceptor were determined. From rotational diffusion times as found by fluorescence correlation spectroscopy (FCS) and consistently by fluorescence anisotropy decay analysis it could be concluded that the open structure (without calcium) is flexible as opposed to the rather rigid closed conformation. The combination of two independent methods gives consistent results and presents a rapid and specific methodology to analyze structural and dynamical changes in a protein upon ligand binding.

2.1 Introduction

Förster resonance energy transfer (FRET) in aqueous solution is a photophysical process where the excited-state energy from a donor molecule is transferred non-radiatively to an acceptor molecule at close distance (< 10 nm) via weak dipole-dipole coupling (Förster 1948). Since FRET occurs between molecules in close proximity, it is used as a spectroscopic ruler to investigate interactions and conformational changes in biological macromolecules (Stryer 1978). A requirement for the occurrence of FRET is spectral overlap between the fluorescence emission spectrum of a donor molecule with the absorption spectrum of an acceptor molecule. The energy transfer efficiency is inversely proportional to the sixth power of the intermolecular distance (R). The critical or Förster radius (R_0) is the distance between donor and acceptor, at which the energy transfer efficiency is 50%. Because FRET is based upon dipolar interactions, both distance and orientation between donor and acceptor transition dipoles are determining factors.

The development of biosensors based on FRET technology has provided information about a large variety of biochemical processes (Miyawaki et al. 1997; Harpur et al. 2001; Jares-Erijman and Jovin 2003; Jares-Erijman and Jovin 2006; van Dongen et al. 2006; Vinkenborg et al. 2007). For quantification of FRET, several methods are available, of which the one based on fluorescence lifetime measurements is the most straightforward method. The time that a molecule remains in the excited state, i.e. the fluorescence lifetime, gives information about the local environment of the chromophore and, in particular, the occurrence of FRET (Suhling et al. 2005). Usually the fluorescence lifetime of the donor molecule is measured and reduction of this lifetime is an indicator for FRET. Donor fluorescence lifetime values often originate from two populations, namely interacting and non-interacting molecules. Therefore, the determined average lifetime does not reflect the real distance between the interacting molecules, because the lifetime (and thus distance) is too long.

Here we describe a methodology where the rise time of the acceptor fluorescence is followed upon donor excitation for the observation of FRET. An advantage using this approach is that only those molecules that are involved in energy transfer are monitored. Furthermore, time-dependent acceptor fluorescence anisotropy measurements upon donor excitation provide information on the mutual dipolar orientation between FRET pairs. A Cameleon calcium sensor protein (YC3.60) was chosen as a model system to test this methodology. Cameleon sensors are fluorescent calcium indicators composed of genetically encoded protein constructs without any cofactors (Miyawaki et al. 1997; Miyawaki et al. 1999). The YC3.60 consists of a fusion of an ECFP (donor) and an EYFP derivative (Venus) moiety (acceptor) linked by calmodulin and a calmodulin binding peptide of myosin light chain kinase (M13). The binding of calcium ions to calmodulin makes calmodulin wrap around the M13 domain enhancing the FRET efficiency from ECFP to Venus, as the calmodulin changes its conformation from an extended calcium-free conformation to a more compact calcium-bound conformation. The dynamic range of the YC3.60 has been optimized by changing the position of the N-terminus via circular permutation of the Venus molecule (Nagai et al. 2004). In this way, the relative orientation, position and distance between ECFP and Venus were modified resulting in the most sensitive Ca^{2+} sensor, YC3.60.

Support for these experiments came from polarized fluorescence correlation experiments when the Venus moiety of YC3.60 is excited and detected. The hydrodynamic parameters of YC3.60 in the presence and absence of calcium are clearly different, which must be ascribed to structural variations.

2.2 Materials and methods

2.2.1 Protein material and sample preparation

cDNA of YC3.60 was kindly provided by Dr. Atsitsu Miyawaki (RIKEN Brain Science Institute, Saitama, Japan). The full length sensor was cloned into the GST fusion vector (pGEX5x2 vector). The YC3.60 was isolated and purified as previously described (Smith and Johnson 1988). The purity of the YC3.60 protein was analyzed on SDS-PAGE and a single band of approximately 75 kDa without degradation products was observed. A stoichiometry of 1:1 between ECFP and the Venus moiety was determined by size exclusion chromatography and absorption spectroscopy. The concentration of YC3.60 was determined with light absorption measurements at 514 nm using the Venus extinction coefficient ε = 92200 $M^{-1}cm^{-1}$. YC3.60 was diluted in 100 mM Hepes buffer at pH 7.9 containing either 50 µM EGTA alone or 50 µM EGTA and 100 µM Ca^{2+} to a final concentration of 100 nM (unless otherwise indicated) for time-resolved fluorescence experiments. The experiments were performed in Hepes buffer pH 7.9. Ensemble fluorescence experiments were performed in quartz cuvettes of 1.0×0.4 cm and at room temperature (22 °C). The fluorescence intensity ratio between Venus (measured at 527 nm) and ECFP (measured at 475 nm) changes from 1.6 in the absence of Ca^{2+} to 8.3 in the presence of 100 µM Ca2+ similarly as reported previously (Nagai et al. 2004)

2.2.2 Time-resolved polarized fluorescence experiments and data analysis

Time-resolved fluorescence measurements were carried out using a mode-locked continuous wave laser for excitation and time-correlated single photon counting as detection technique as previously described (Borst et al. 2005). The samples were excited with plane polarized light pulses (0.2 ps FWHM) at an excitation frequency of 3.8 MHz and both parallel- and perpendicular-polarized fluorescence intensities were detected. At 400-nm excitation ECFP fluorescence was detected with a 480.5-nm interference filter (Schott, Mainz, Germany, half-bandwidth of 5.4 nm). The sensitized emission of Venus fluorescence was detected with an OG 530 cut-off filter (Schott) and 557.6-nm interference filter (Schott, half-bandwidth 5.9 nm). Some experiments were conducted at 420-nm excitation, but then Raman scattering turned out to be an interfering factor at 480.5-nm detection of the donor fluorescence. Another experiment was conducted using a much higher concentration of YC3.60 (500 nM as compared to the usual 100-nM YC3.60 concentration) to reduce the interference of Raman scatterering and background fluorescence on the quenched donor fluorescence decay. The dynamic instrumental response function of the setup (approximately 40 ps FWHM) was obtained at the ECFP or Venus emission wavelengths by using a solution of xanthione in ethanol as reference compound having an ultrashort fluorescence lifetime of 14 ps (Ho et al. 1989; Boens et al. 1990; Karolczak et al. 2001). The use of the reference convolution method (Vos et al. 1987; Boens et al. 1990) together with the current instrumentation enables determining fluorescence lifetimes with high accuracy and picosecond precision. A systematic study involving both simulations and experiments have shown that the standard error in determination of lifetimes can be in the order of one tenth of the FWHM (Karolczak et al. 2001). With the setup used it was possible to accurately determine 7-ps fluorescence lifetimes and >10-ps correlation times (Digris et al. 1999; van den Berg et al. 2002; van den Berg et al. 2004). In this work two time scales were used: 1 ps/channel and 5 ps/channel giving a time range of 4 ns and 20 ns for 4096 data points. Global analysis of the experimental data taken at short and long timescales using multi-exponential model functions was performed as described previously (Borst et al. 2005; Visser et al. 2005) To obtain an optimal fit of the time-resolved fluorescence anisotropy data of YC3.60 an associative fitting protocol was used, in which short fluorescence lifetimes are grouped with short correlation times and longer fluorescence lifetimes with longer correlation times. Another experiment was conducted to observe the fluorescence anisotropy decay of YC3.60 when the Venus part is excited (492 nm) and monitored (557 nm).

2.2.3 Acceptor photobleaching experiments

The acceptor photobleaching (APB) experiments were performed on microdroplets composed of YC3.60 -/+Ca^{2+}. Microdroplets of YC3.60 were prepared by mixing the protein solution with 1-octanol at a ratio of 1:9 v/v as described by Patterson et al. (1997). Droplets of 50 µm in diameter were imaged using a confocal laser scanning microscope (LSM510, Carl Zeiss, Jena, Germany). The CFP moiety within YC3.60 was excited with the 458 nm argon laser line and the Venus with the 514-nm argon laser line, respectively. The fluorescence of CFP was detected using a bandpass filter of 470-500 nm and Venus fluorescence by a bandpass filter of 535-595 nm. FRET efficiencies were determined as described in Bastiaens et al. (1996).

2.2.4 Polarized fluorescence correlation experiments and data analysis

Fluorescence correlation spectroscopy (FCS) was carried out with a home-built multiparameter fluorescence detection (MFD) setup based on an inverted confocal microscope (IX70, Olympus, Hamburg, Germany) using epi-illumination, as described earlier and summarized in the following references. (Kühnemuth and Seidel 2001; Felekyan et al. 2005; Widengren et al. 2006) The fluorescent molecules were excited by a linearly polarized argon-ion-laser (Innova Sabre, Coherent) at 496 nm in cw mode. The laser was focused into the sample by a NA = 1.2 water-immersion objective lens (UPLAPO 60x, Olympus). The fluorescence was collected by the same lens and separated from the excitation by a polychroic beamsplitter (488/636 PC, AHF, Tübingen, Germany). A confocal pinhole of 100 µm diameter and the slightly underfilled objective yielded a detection volume element of approximately 1 µm diameter and 1.6 fl size, as determined by fluorescence correlation spectroscopy. The characteristic diffusion time of rhodamine 110 was 0.22 ms.

The applied mean irradiance in the focus was I0/2 = 150 kW/cm^2 (Schaffer et al. 1999). The collected fluorescence light was separated first into its parallel and perpendicular components by a polarizing beamsplitter cube (VISHT11, Gsänger, Planegg, Germany), then again divided into two parts by 50% beamsplitters. Fluorescence bandpass filters (HQ533/46, AHF) blocked residual laser light and reduced Raman scattering from the solvent. The detectors used were single photon avalanche diodes (SPCM AQR 14, Perkin Elmer, Germany). The single photon signal traces were recorded by two synchronized but otherwise independent TCSPC boards (SPC132, Becker&Hickl, Berlin, Germany). Each board monitored, via a router, one parallel and one perpendicularly polarized fluorescence channel. This way by correlating traces from different boards FCS curves down to picoseconds could be generated, not affected by the deadtime of detectors and electronics. Software-correlation was usually performed in both directions (channel A → channel B, channel B → channel A). Both correlation curves were then averaged to reduce noise. In each presented experiment $7x10^8$ photons were recorded. Three different combinations of polarizations were computed: autocorrelation of the fluorescence polarized parallel to the excitation polarization (pp), perpendicular to the excitation (ss), and cross-correlation of both polarizations (ps and sp).

The data was approximated by a multi-exponential model function in a global analysis (OriginPro 7.5, OriginLab Corporation, Northampton, MA). The range of data for the fit was limited to correlation times between tc = 10^{-6} and $5x10^{-3}$ ms. At shorter times increased noise prohibits meaningful analysis. At longer times diffusion in and out of the focus becomes the dominating effect in the FCS. This term is distorted at high irradiances due to saturation and photobleaching, is prone to artifacts and requires sophisticated fitting models, which are beyond the scope of this paper (Enderlein et al. 2005)

2.2.5 Modeling

Three-dimensional models of the open (-Ca^{2+}) and closed (+Ca^{2+}) conformation of YC3.60 were constructed. For the closed conformation the crystal structure files 2BBM.pdb (calmodulin wrapped around the light chain myosin kinase helix (M13)) and 1C4F.pdb (GFP) were used. For the open conformation the calmodulin part of 1XFU.pdb with M13 and 1C4F.pdb (GFP) were used. The different domains of the YC3.60 (CFP,CaM/M13, Venus) are connected by flexible linkers. These linkers provided flexibility to adapt the orientation within the YC3.60 for the open and closed conformations, which are based on the two different PDB-structures of the CaM/M13 unit. The lengths of the linkers were restricted to a maximal distance between the fluorescent moieties. The transition dipole moments in the molecular frame of the chromophore in GFP (Rosell and Boxer 2003) and the relative angle between these vectors of the two chromophores within both fluorescent protein units were used to orient the individual parts of the YC3.60 molecule using the program PyMOL (http://www.pymol.org) (DeLano 2002). It is assumed that the absorption and emission dipole moments coincide in the molecular frame of the chromophore and that the transition dipoles have the same direction in the CFP and YFP chromophores as in the GFP chromophore. This assumption is more rigorous for the CFP chromophore than for the one of YFP, which is except for the π-stacking interaction with the phenolic group of Tyr^{203} identical to the GFP chromophore.

2.3 Results

2.3.1 Time-resolved FRET spectroscopy

Time-resolved fluorescence experiments were conducted by monitoring donor fluorescence lifetime in which YC3.60 was excited at 400 nm (ECFP moiety) and the fluorescence of ECFP was detected at 480 nm. The fluorescence decay in the ECFP channel requires a three-component exponential model to obtain a satisfactory fit (figure 1). Analysis of the fluorescence decays resulted in fluorescence lifetimes of 0.67 ns (α_1=45%), 2.20 ns (α_2=36%) and 3.57 ns (α_3=19%) (table 1) yielding an (amplitude-weighted) average fluorescence lifetime $<\tau>$ = 1.77 ns for the calcium free YC3.60. In the presence of Ca^{2+} the fluorescence lifetimes were 0.28 ns (α_1=46%), 1.39 ns (α_2=34%) and 3.57 ns (α_3=20%) resulting in reduction of the average lifetime to $<\tau>$ = 1.31 ns (table 1). The quenching of the ECFP fluorescence within the calcium sensor results in significantly shorter average lifetimes as compared to the unquenched average fluorescence lifetime of purified ECFP alone (figure 1 curve 1; $<\tau>$ = 2.71 ns).

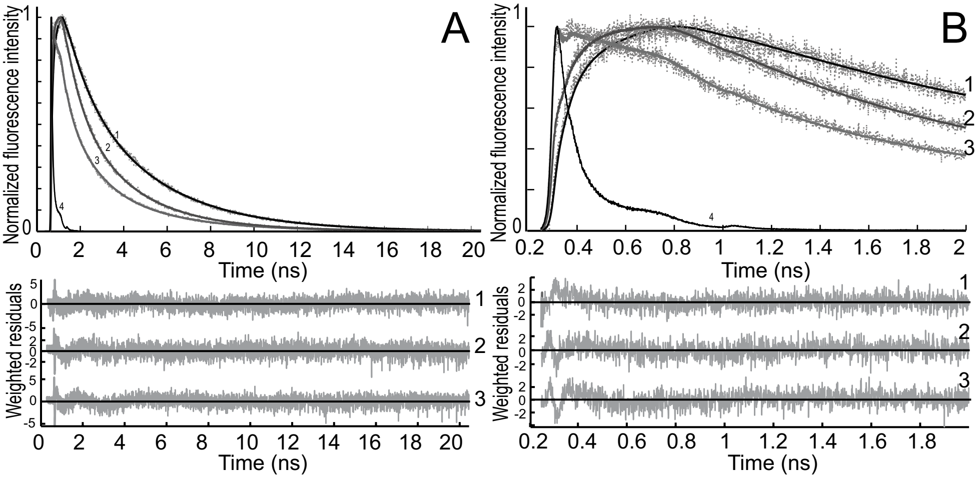

Figure 1. *Normalized experimental (dotted line) and fitted (solid line) fluorescence decay curves of ECFP (curve 1), YC3.60 in absence of* Ca^{2+} *(curve 2), YC3.60 in presence of* Ca^{2+} *(curve 3) and the reference compound xanthione in ethanol (curve 4). The excitation wavelength was 400 nm and the detection wavelength of ECFP emission was 480 nm. In panel A the data are presented with a time scale of 5 ps/channel, while this is 1 ps/channel in panel B, in which only the first two nanoseconds are shown. The experimental data taken at both time scales are globally analyzed using a multiexponential model with amplitudes* α_i *and lifetimes* τ_i *as adjustable parameters for obtaining an optimal fit. In case of ECFP a bi-exponential decay model with lifetimes 0.97 ns and 3.57 ns was sufficient. The long 3.57-ns lifetime was fixed in the tri-exponential decay model of YC3.60 All recovered parameters (*α*,* τ*) are collected in table 1 (case 1). Weighted residuals belonging to each fitted curve are presented in the bottom panels. Global* χ^2 *values are, respectively, for ECFP 1.11, for YC3.60 in absence of* Ca^{2+} *1.14 and for YC3.60 in presence of* Ca^{2+} *1.15.*

A correct method for the observation of FRET is to follow the time-dependent increase in fluorescence intensity of the acceptor, which is a direct consequence of energy transfer (Kulinski et al. 1987; Visser et al. 2005). The experiments were performed by exciting the donor at 400 nm and detecting Venus at 557 nm (figure 2). The obtained data were analyzed using a multiple-component model with both positive and negative pre-exponential factors (table 1). The short lifetime with negative amplitude reflects the energy transfer process, and the part of the decay with positive amplitude corresponds to the fluorescence of the acceptor. In the absence of Ca^{2+} an average fluorescence lifetime component (1.4 ns) with negative amplitude was found. Upon addition of Ca^{2+}, a significant decrease of this short component (0.056 ns) was observed. A long fluorescence lifetime component (3.1 ns) of Venus with positive amplitude was found, independent of the presence of calcium.

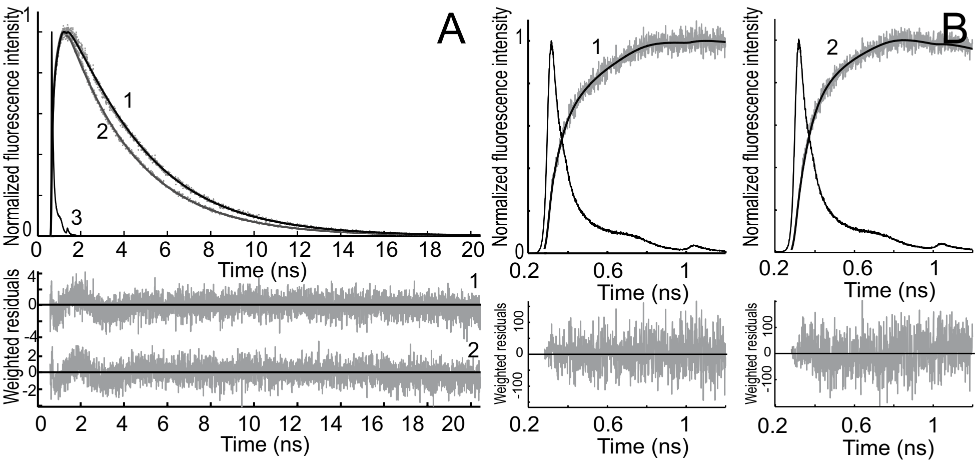

Figure 2. *Normalized experimental (dotted line) and fitted (solid line) fluorescence rise and decay curves of the Venus acceptor, detected at 557 nm, in YC3.60 upon donor excitation at 400 nm. In panel A the data are presented with a time scale of 5 ps/channel, while this is 1 ps/channel in panel B, in which only the first nanosecond is shown. Curve 1 is the fluorescence intensity trace of YC3.60 in the absence of* Ca^{2+}*, while curve 2 is that of YC3.60 in the presence of* Ca^{2+}*. Curve 3 represents the reference compound xanthione in ethanol. In panel B it can be observed that the rise time of curve 2 is shorter than that of curve 1, because curve 2 is already starting to decay. The experimental data taken at both time scales are globally analyzed using a bi-exponential rise (in case of calcium-free YC3.60) and mono-exponential decay model with amplitudes* α_i *and lifetimes* τ_i *as adjustable parameters for obtaining an optimal fit. The recovered parameters* $(\alpha, \tau$ *are collected in table 1 (case 3). Weighted residuals are presented in the bottom panels. Global* χ^2 *values are, respectively, for YC3.60 in absence of* Ca^{2+} *1.05 and for YC3.60 in presence of* Ca^{2+} *1.05.*

2.3.2 Time-resolved fluorescence anisotropy

The time-dependent fluorescence anisotropy of the acceptor exhibits a peculiar pattern after donor excitation (figure 3). The fluorescence anisotropy shows an initial decay with a correlation time that is compatible to the rise time of the acceptor fluorescence. This correlation time becomes much shorter when calcium is present. In the latter case the anisotropy even becomes negative, followed by a slow increase to zero. The time-resolved fluorescence anisotropy curves were globally analyzed using an associative, two-component model yielding two correlation times (ϕ_1 and ϕ_2) and corresponding amplitudes (β_1 and β_2) (table 2) (Borst et al. 2005; Visser et al. 2005). The long correlation time (ϕ_2) can be attributed to overall protein rotation (ϕ_{prot}). Its value was obtained after fitting the fluorescence anisotropy decay of YC3.60 upon excitation and fluorescence detection of the Venus moiety (see below). The long correlation times were fixed during analysis. The short correlation time (ϕ_1), due to energy transfer, decreases from 1.29 ns (- Ca^{2+}) to 0.056 ns (+ Ca^{2+}).

Table 1. *Fluorescence decay and rise parameters of YC3.60 (-/+Ca2+) upon excitation at 400 nm and detection at either donor (480 nm) or acceptor (557 nm) emission.*

Sample	Detection (nm)		α_1 (%)	τ_1 (ns)	α_2 (%)	τ_2 (ns)	α_3 (%)	τ_3 (ns)	α_4 (%)	τ_4 (ns)	$<\tau>$ (ns)
ECFP	480		33	0.97±0.06	67	3.57±0.05					2.71
Case 1: all lifetimes and relative amplitudes are included in calculation of $<\tau>$											
YC3.60- Ca^{2+}	480		45	0.67±0.008	36	2.20±0.05	19	3.57(fixed)			1.77
YC3.60+ Ca^{2+}	480		46	0.280±0.003	34	1.39±0.01	20	3.57(fixed)			1.31
Case 2: only FRET-active donor molecules contribute to $<\tau>$											
			Non-interacting CFP (20%)				Interacting CFP (80%)				
YC3.60- Ca^{2+}	480	A	33	0.98±0.02	67	3.59±0.01	50	0.60±0.01	50	2.2±0.1	1.40
	480	B	36	1.04±0.01	64	3.62±0.01	48	0.500±0.004	52	2.10±0.01	1.33
	480	C	37	1.08±0.01	63	3.65±0.01	49	0.51±0.01	51	2.25±0.02	1.40
YC3.60+ Ca^{2+}	480	A	33	0.98±0.02	67	3.59±0.01	60	0.269±0.004	40	1.46±0.01	0.69
	480	B	36	1.10±0.02	64	3.40±0.08	72	0.024±0.007	28	0.28±0.01	0.095
	480	C	36	1.04±0.02	64	3.50±0.01	67	0.024±0.007	33	0.14±0.02	0.063
Case 3: $<\tau>$ is calculated from average rise time of acceptor intensity											
YC3.60- Ca^{2+}	557		-6	0.38±0.06	-24	1.70±0.3	70	3.10(fixed)			1.40
YC3.60+ Ca^{2+}	557		-26	0.056±0.012	74	3.10(fixed)					0.056

Standard errors of the fluorescence lifetimes are obtained from the fit.

Case 1. The sum of amplitudes has been normalized to 100%. The average fluorescence lifetime $<\tau>$ is the amplitude-weighted average lifetime.

Case 2. The parameters of interacting and non-interacting donor molecules were derived from the following 4-exponential model:

$$I = N_1(\alpha_1 e^{-\frac{t}{\tau_1}} + \alpha_2 e^{-\frac{t}{\tau_2}}) + N_2(\alpha_3 e^{-\frac{t}{\tau_3}} + a_4 e^{-\frac{t}{\tau_4}})$$

in which $N_1 = 20\%$ and $N_2 = 80\%$ and $\alpha_1+\alpha_2 = 1$ (100%); $\alpha_3+\alpha_4 = 1$ (100%).

$<\tau>$ is obtained from the values of FRET-active ECFP.

A: analysis of one experiment with 100 nM YC3.60; B: global analysis of 6 different experiments (100 nM YC3.60) linking common parameters; C: analysis of one experiment with 500 nM YC3.60.

Case 3. A negative value of the amplitude α_1 indicates a rise of fluorescence intensity. The sum of the absolute values of the amplitudes has been normalized to 100%.

YC3.60 – Ca^{2+}: Rise time obtained from global analysis of 3 independent experiments using a 2-component fit model and presented as amplitude-weighted average rise time.

YC3.60 + Ca^{2+}: Rise time values obtained using a 1-component fit model at one time scale (1 ps/channel).

From the time-resolved fluorescence and fluorescence anisotropy results one can calculate the steady-state anisotropy <*r*>. The calculated values are <*r*> = 0.121 (-Ca^{2+}) and <*r*> = -0.047 (+Ca^{2+}) (shown as dashed lines in figure 3A). These values are in excellent agreement with experimental values reported previously (Nagai et al. 2004).

In figure 4 the experimental and fitted fluorescence anisotropies are presented for YC3.60 in the absence and presence of calcium. In these experiments the Venus moiety is selectively excited at 492 nm and its fluorescence detected at 557 nm. The fluorescence anisotropy decay is a single exponential in both cases. However, when calcium is absent the decay becomes significantly faster. The overall rotational correlation time changed upon binding of calcium to calmodulin from 31 ns (-Ca^{2+}) to 50 ns (+Ca^{2+}).

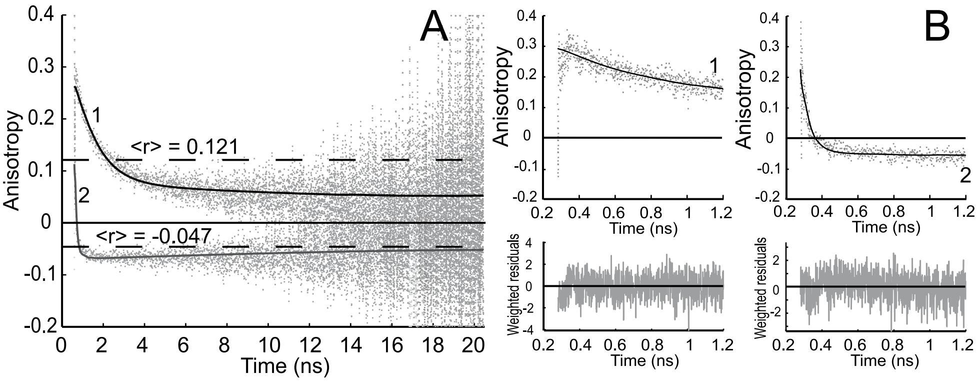

Figure 3. Experimental (dotted line) and fitted (solid line) fluorescence anisotropy decays of the Venus acceptor, detected at 557 nm, in YC3.60 upon donor excitation at 400 nm. Curve 1 is the time-dependent fluorescence anisotropy of YC3.60 in absence of Ca^{2+}, while curve 2 is that of YC3.60 in presence of Ca^{2+}. In panel A the data are presented with time scale of 5 ps/channel, while this is 1 ps/channel in panel B, in which only the first nanosecond is shown. The dashed horizontal lines in panel A represent steady-state anisotropy values be longing to curves 1 and 2. The steady-state anisotropy is obtained from:

$$<r>= \int_0^\infty r(t).I(t)dt \Big/ \int_0^\infty I(t)dt$$

I(t) is the total fluorescence decay ($I(t)=I_{||}(t)+2I_{\perp}(t)$) and r(t) is the time-dependent fluorescence anisotropy ($r(t)=(I_{||}(t) - I_{\perp}(t))/ I(t)$). An associative global analysis to a bi-exponential model was performed to the polarized intensity components, in which the short correlation time is grouped with the short fluorescence lifetime and the long correlation time with the long fluorescence lifetime. The long correlation time was separately determined and fixed in the analysis (see legend to figure. 4). The analyzed data yielded correlation times (ϕ_i) and amplitudes (β_i) that are collected in table 2. Weighted residuals are presented at the bottom of panel B. Global χ^2 values are, respectively, for YC3.60 in absence of Ca^{2+} 1.11 and for YC3.60 in presence of Ca^{2+} 1.07.

***Table 2**. Fluorescence anisotropy decay parameters of YC3.60 (-/+Ca^{2+}) upon excitation at 400 nm or 492 nm and emission detection at 557 nm.*

Sample	β_1	ϕ_1 (ns)	β_2	ϕ_2 (ns)
YC3.60 - Ca^{2+} (λ^{ex} 400 nm)	0.19 (0.17 - 0.22)	1.29 (1.10 - 1.41)	0.08 (0.06 - 0.10)	31 (fixed)
YC3.60 + Ca^{2+} (λ_{ex} 400 nm)	0.13 (0.12 - 0.23)	0.056 0.047 - 0.069)	-0.060 (-0.063 - 0.057)	50 (fixed)
YC3.60 - Ca^{2+} (λ_{ex} 492 nm)			0.368 (0.366 - 0.371)	31.2 (29.8 - 32.7)
YC3.60 - Ca^{2+} (λ_{ex} 492 nm)	0.052 (0.043 - 0.063)	5.1 (3.4-6.8)	0.322 (0.310-0.332)	50 (fixed)
YC3.60 + Ca^{2+} (λ_{ex} 492 nm)				50.4 (47.8 - 53.3)

Values in parentheses are the 67% confidence limits obtained from a rigorous error analysis. The recovered parameters in the first two entries (λ_{ex} 400 nm) were obtained by associative analysis of fluorescence anisotropy decays (taken at two time ranges), in which the short fluorescence lifetimes (table 1, case 3) were grouped with the short correlation times (ϕ_1) and the long (fixed) fluorescence lifetimes with the long (fixed) correlation times (ϕ_2). The recovered parameters in the fourth entry (λ_{ex} 492 nm) were obtained after a bi-exponential decay analysis with the long correlation time (ϕ_2) fixed to 50 ns. In this case the fitted curve had the same quality criteria as for the mono-exponential model (see figure. 4).

2.3.3 Acceptor photobleaching

It is desirable to obtain estimates of the FRET efficiency using another, independent method. Several APB experiments on droplets of YC3.60 were performed using a confocal microscope. From results of APB analysis FRET efficiencies of 39±4 % in YC3.60 (- Ca^{2+}) and 59±14 % in YC3.60 (+ Ca^{2+}) were obtained.

2.3.4 Fluorescence correlation spectroscopy

The FCS curves of YC3.60 upon direct acceptor excitation showed a distinct polarization dependence in the range from $t_c = 10^{-6}$ to10^{-3} ms, as it is characteristic for rotational diffusion of (nearly) spherical molecules with transition dipole moments of absorption and emission oriented parallel to each other (figure 5A). The observed relative amplitudes of the rotational terms $(G_{max}-G_{iso}-1)/(G_{iso}-1)$ of 1.2, 0.4 and 0.1 for pp, ss and ps/sp crossed polarizations are consistent with the numbers predicted for spherical rotators of 1.78, 1.14 and 0.2, taking into account that the experimental values as directly read from the curves are strongly reduced by the overlap with the antibunching term. (Ehrenberg and Rigler 1974; Aragón and Pecora 1975; Kask et al. 1989). Theory predicts that correlation curves of even ideal spheres should exhibit two bunching terms for the rotational regime (t_{rot} and 0.3 t_{rot}). For autocor-

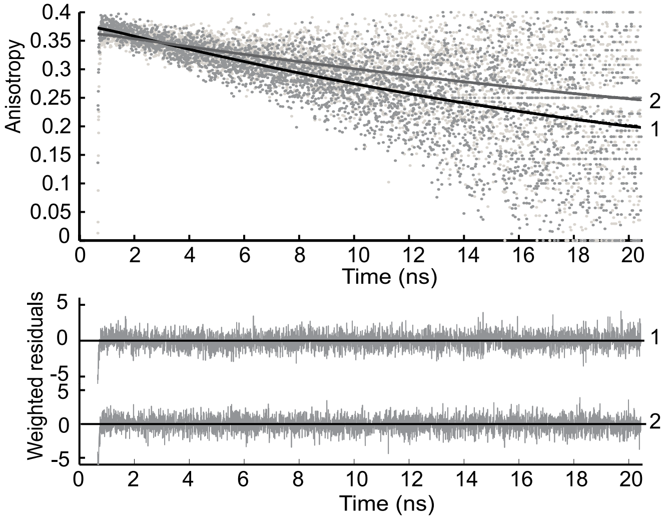

Figure 4. Experimental (dots) and fitted (solid line) fluorescence anisotropy decays of YC3.60 upon excitation (492 nm) and detection (557 nm) of the Venus moiety in absence of Ca^{2+} (curve 1) and in presence of Ca^{2+} (curve 2). The decay model is a mono-exponential function yielding the anisotropy at time zero, r(0) = r_0, and rotational correlation time that are presented in Table 2. Weighted residuals are presented in the bottom panel. Global χ^2 values are, respectively, for YC3.60 in absence of Ca^{2+} 1.06 and for YC3.60 in presence of Ca^{2+} 1.09.

relation of the fluorescence polarized parallel to the exciting laser light (pp, curve 1 in figure 5A) the contribution of the second (shorter) time should be only 8% and is neglected in the following analysis.

The parameters of the fluorescence correlation curve G(tc) were derived from the following 4-exponential model, where t_c is the correlation time and t_i is the characteristic antibunching or bunching time.

$$G(t_c) = 1 - \sum_{i=1}^{4} A_i + \sum_{i=1}^{4} A_i e^{-t_c/t_i} \qquad (1)$$

A sum of 3-4 exponentials representing photon antibunching (t_1, mainly below 10^{-5} ms), rotational diffusion (t_2 and t_3, mainly between 10^{-5} and 10^{-4} ms) and photophysical triplet and/or protonation kinetics (t_4, mainly above 10^{-4} ms) was globally fitted to the pp-polarized correlation data obtained from YC3.60 in absence and in presence of Ca^{2+} (Mets 2001). The only non-global parameters used corresponded to the rotational diffusion: one independent decay time for each curve and, in case of a biexponential decay, the relative amplitudes. Three fits have been performed differing only in the modeling of the rotational diffusion: (1) one decay time for each curve, (2) two times for YC3.60 in absence, one time for YC3.60 in presence of Ca2+, and (3) two decay times for each curve. The results are summarized in table 3.

The rise time at short times, t_1, is in all fits around 2.6 ns. This is consistent with the measured fluorescence lifetime for the Venus moiety of τ_2 = 3.2 ns and a high excitation rate

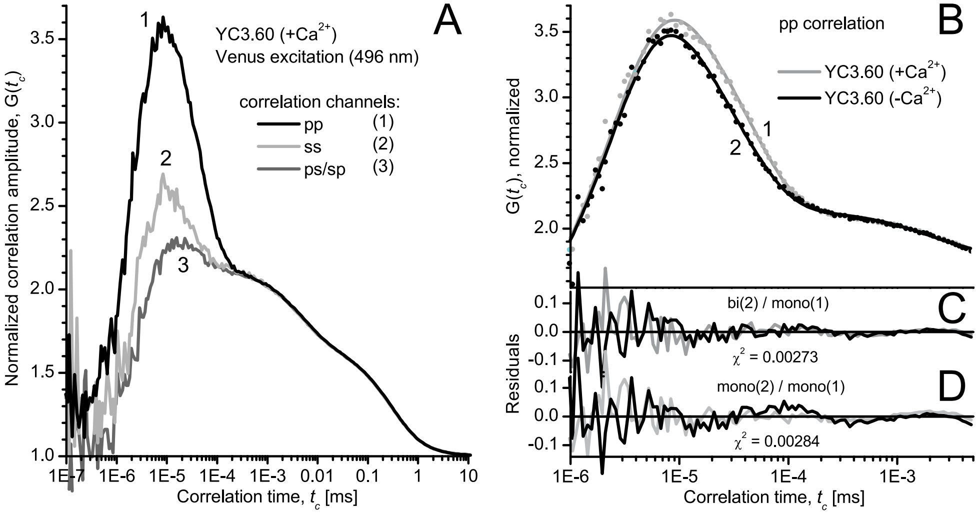

***Figure 5**. Experimental and fitted fluorescence correlation curves of YC3.60 after excitation and detection of the acceptor (λ_{ex} 496 nm, λ_{det} 510-556 nm). The curves are normalized at tc = 1.2 µs. A: Correlation curves for YC3.60 in presence of Ca^{2+}. Three different combinations of polarizations are presented: autocorrelation of the fluorescence polarized parallel to the excitation polarization (pp, curve 1), perpendicular to the excitation (ss, curve 2), and cross-correlation of both polarizations (ps and sp, curve 3). Only the polarization dependent part of the correlation curves can be assigned to rotational diffusion. The measurement time was 14 min. B: pp-correlation curves of YC3.60 in presence of Ca^{2+} (curve 1) are compared to YC3.60 in absence of Ca^{2+} (curve 2). The rotational part of curve 1 (+Ca^{2+}) can be reproduced well by a single exponential, while curve 2 (-Ca^{2+}) shows significant deviations and exhibits a second decay time. Fit parameters are presented in Table 3. C: Residuals for the global fit with: (YC(+Ca^{2+}): 3 exponentials, YC(-Ca^{2+}): 4 exp.). D: For comparison residuals for the global fit with: YC(-/+Ca^{2+}): 3 exp ; i.e. a single independent rotational correlation time for each of the two curves.(fit not shown).*

k_{01} ($1/t_1 = 1/\tau_2 + k_{01}$) (Felekyan et al. 2005). The photophysics term (t_4 = 2-3 µs) was only taken into account in the fits because of a slight overlap with the tail of the rotational term and has otherwise no relevance for the topic of this paper.

Fitting a single decay time to each of the correlation curves (fit 1) does not give a satisfactory result for YC3.60 in absence of Ca^{2+}, as indicated by the residuals (Figure 5D) and by χ^2. The residuals indicate (figure 5D) the necessity of a second bunching time in the regime of the rotational correlation especially for YC3.60 (-Ca^{2+}). Adding this time improves the fit significantly (fit 2, figure 5C). If there is also a second time allowed for YC3.60 in presence of Ca^{2+}, only a small improvement of the fit is achieved (fit 3). The amplitude of the additional bunching term is relatively small and has a large statistical error. According to this analysis the rotational correlation of YC3.60 in absence of Ca^{2+} exhibits a biexponential decay with characteristic times of t_2 = 17.5±4.3 ns and t_3 = 42.9±1.6 ns. However, in presence of Ca^{2+} the contribution of this short rotation time vanishes or is at least strongly reduced.

Table 3. *Fluorescence correlation parameters of YC3.60 (-/+Ca2+) upon excitation at 496 nm and emission detection at 510-556 nm.*

Sample	t_1 (ns)	A_2(rel.)	t_2 (ns)	A_3(rel.)	t_3 (ns)	Fit #
YC3.60-Ca^{2+}	2.56±0.04	0 (fixed)		1 (fixed)	33.2±1.1	1
YC3.60+Ca^{2+}	(global)				43.7±1.5	
YC3.60-Ca^{2+}	2.58±0.04	0.30±0.08	17.5±4.3	0.70±0.09	42.9±1.6	2
YC3.60+Ca^{2+}	(global)	0 (fixed)		1 (fixed)	(global)	
YC3.60-Ca^{2+}	2.68±0.07	0.42±0.08	15.0±3.2	0.58±0.08	50.4±4.4	3
YC3.60+Ca^{2+}	(global)	0.22±0.08	(global)	0.78±0.07	(global)	

Standard errors are obtained from the fit. A global fit was performed in the data range from $t_c = 10^{-6}$ *to* $5\text{x}10^{-3}$ *ms. The relative amplitudes* A_i*(rel) were determined from* $A_i(rel) = A_i / (A_2 + A_3)$*. Values for* t_4 *for fit 1, 2 and 3 are 1.8±0.5 µs, 2.2±0.6 µs and 2.9±1.2 µs.* χ^2 *for fit 1, 2 and 3 is 0.00284, 0.00273 and 0.00267, respectively. Fit 2 is shown in figure 5B, residuals in figure 5C. Residuals of fit 1 are presented in figure 5D.*

2.4 Discussion

2.4.1 Donor fluorescence decay in case of FRET

In time-resolved FRET studies, usually the fluorescence lifetime of the donor molecule is measured. Quenching of the donor fluorescence by an acceptor molecule leads to a shorter fluorescence lifetime of the donor. The experimental data of the donor fluorescence decay in YC3.60 was analysed with three fluorescence lifetime components for an optimal fit. A complicating factor in the analysis is the already heterogeneous fluorescence decay of single ECFP molecules which needs to be analyzed with at least two components to obtain a satisfying fit (table 1) (Borst et al. 2005; Habuchi et al. 2002; Tramier et al. 2002; Camuzeaux et al. 2005; Grailhe et al. 2006; Jose et al. 2007; Millington et al. 2007). The origin of the two fluorescence lifetimes in ECFP has been attributed to the presence of two distinct chromophore conformations in the protein (Hyun Bae et al. 2003), which are in slow equilibrium (Seifert et al. 2002) and exhibit similar spectra (Demachy et al. 2005). The average donor lifetime of the YC3.60 decreased from 1.77 ns (-Ca^{2+}) to 1.31 ns (+Ca^{2+}) and the average donor fluorescence lifetime without acceptor was 2.71 ns (case 1: average donor fluorescence lifetime including all lifetime components). Close examination of table 1, however, learns that there are still, independent on calcium, long lifetime components > 3 ns present in the donor fluorescence decay. These long lifetime components may originate from a population of YC3.60 molecules, in which no FRET occurs. For instance, when a certain population of the protonated form of the Venus is present, FRET is not observed because the overlap between absorption spectrum of the protonated acceptor and the donor fluorescence spectrum is strongly reduced.

The pK_a of the Venus chromophore has been reported to be equal to 6.0 (Nagai et al. 2002). This pK_a value may be different in the circular permutated variant of the Venus chromophore. The same observation has been made and discussed recently for CFP-YFP constructs in mammalian and fungal cells (Millington et al. 2007). Millington and coworkers (Millington et al. 2007) have proposed two models to explain the results. They have labelled their models 3tau and 4tau. The 3tau model comprises the simplest case: only one of the two ECFP conformations participates in FRET. The more complex (and more realistic) 4tau model assumes that both conformations participate in FRET. There are two complicating factors in the latter approach. One complication in the 4tau model is that there are two different critical transfer distances (R_0), because the fluorescence quantum yields of the two donors differ by a factor given by the ratio of the respective lifetimes (τ_{D1}/τ_{D2}). The other complication arises from the observation that the shorter, unquenched donor lifetime (τ_{D1}) becomes similar to the quenched donor lifetime τ_{DA2} and cannot be distinguished any more. Although there are four lifetimes present, only three of them can be actually resolved in the decay analysis. We have analyzed the fluorescence decays of YC3.60 using the 4tau model with the following modifications. A global analysis was performed on the fluorescence decay data of YC3.60 under high and low calcium conditions and of those of unquenched ECFP, in which a fixed amplitude ratio for the unquenched lifetimes was preserved. The other lifetime components then should represent the true donor lifetime values in case of FRET. These average lifetimes become shorter (1.4 ns, $-Ca^{2+}$ to 0.69 ns, $+Ca^{2+}$) when the long lifetime components are excluded in the average lifetimes (case 2A: average donor fluorescence lifetime from a FRET-active selection) (table 1). Since the average donor fluorescence lifetime is still a factor of 10 longer than obtained from the acceptor rise time (see next paragraph), we decided to globally analyse all available experimental data taken at different days, from different YC3.60 preparations of the same concentration (100 nM) and with different excitation wavelengths (400, 420 and 440 nm). All common parameters were linked and potential contributions from Raman scattering and impurities from the background (taken from samples without protein and measured under identical conditions) were taken into account. The results of this extensive global analysis yielded parameters that are also collected in table 1 (case 2B). The average fluorescence lifetime of the donor in the calcium-free form of YC3.60 remained unaltered. On the other hand, the average fluorescence lifetime of the donor in calcium-bound YC3.60 becomes distinctly shorter (0.095 ns). Therefore, we have to conclude that in cases of very large transfer efficiencies the donor fluorescence lifetime becomes so short, comparable to a very small intensity contribution, that its lifetime can be barely recovered in the presence of a dominant background fluorescence consisting of a non-quenched donor population and of Raman scattering and impurity fluorescence. In addition, the intrinsic heterogeneity of the ECFP fluorescence kinetics is a complicating factor in the decay analysis. To further support this conclusion we have analyzed experimental data of YC3.60 at relatively high protein concentration (500 nM) at which background contributions to the decay are expected to be minimal. Indeed, very good agreement between donor fluorescence lifetimes and rise times is obtained both in the absence and presence of calcium (case 2C).

2.4.2 Rise of acceptor fluorescence intensity in case of FRET

To recover a correct FRET efficiency a method is applied, in which the rise time of the acceptor fluorescence is detected upon donor excitation (Figure 2; parameters collected in table 1). In this way one selectively observes the pure FRET process between donor and acceptor molecules, since the transfer rate constant (k_T) can be directly determined from the rise time of the acceptor fluorescence intensity, which is equivalent to the donor fluorescence lifetime in the presence of acceptor (τ_{DA}). The method of analysis of acceptor rise time has been described for single-tryptophan containing proteins transferring energy from tryptophan to a fluorescent acceptor (Kulinski et al. 1987; Visser et al. 2005). It was pointed out that this might be a useful approach in cases where the donor exhibits fluorescence lifetime heterogeneity as observed in the YC3.60. Although other research groups have made the same observations in case of energy transfer between two fluorescent proteins (Harpur et al. 2001; Camuzeaux et al. 2005; Millington et al. 2007), this approach has not yet been assessed quantitatively. We will discuss the method in more detail in the next paragraph (case 3: average donor fluorescence lifetime from acceptor rise time). In supplementary material (S1) simulations are presented to investigate the resolvability of different rise times under certain conditions. The simulations were set up to mimick the experiment as closely as possible, for example by using convolution with an experimental impulse reponse function and two rise times corresponding to a biexponential donor fluorescence decay in the presence of acceptor. The main outcome of the simulations is that analysis of longer rise times (0.5-2 ns) with a two-component model yields a better fit quality than with a single-component model. In case of short rise times (50-200 ps) a model using two components has similar fit quality as that of a single-rise time model. Following the results of the simulations a global analysis was performed on experimental fluorescence rise and decay traces of YC3.60 measured at both time resolutions (1 and 5 ps/channel) thereby linking common rise and decay parameters. For YC3.60 in the presence of calcium the data can be sufficiently analyzed using a monoexponential model with one rise time of 0.056 ns and one decay time of 3.1 ns. In case of calcium-free YC3.60 a model with two rise times and one decay time yielded a much better fit than a one-component rise model. Since the longer rise time and the decay time exhibited a strong correlation, the decay time had to be fixed in the analysis to recover a reliable value of the longer rise time. All recovered parameters are collected in table 1 (case 3).

2.4.3 Comparison of both methods: donor fluorescence decay and acceptor fluorescence rise

FRET efficiencies can be determined from $E = 1 - \tau_{DA} / \tau_D$, where τ_{DA} is the donor fluorescence lifetime in the presence of acceptor and τ_D that in the absence of acceptor. The rate constant of energy transfer (k_T) can be determined from $k_T = 1/\tau_{DA} - 1/\tau_D$. The transfer rate constant can be directly related to the distance through $k_T = \tau_D\text{-}1(R_0/R)^6$. From the overlap integral between ECFP emission and EYFP absorption spectra, donor fluorescence quantum yield and, initially assuming an orientation factor $\kappa^2 = 1$, a critical distance $R_0 = 4.90$ nm was determined (Hink et al. 2003). Using the average lifetime values and $\tau_D = 2.71$ ns, the FRET

Table 4. *FRET parameters of YC3.60 (-/+Ca^{2+}) upon excitation at 400 nm and detection at donor (480 nm) or acceptor (557 nm) emissions.*

	τ_{DA} (ns)		Transfer efficiency (%)		k_T (ns^{-1})		R (Å)	
Analysis	-Ca^{2+}	+Ca^{2+}	-Ca^{2+}	+Ca^{2+}	-Ca^{2+}	+Ca^{2+}	-Ca^{2+}	+Ca^{2+}
Case 1	1.77	1.31	35	52	0.19	0.39	55	48
Case 2A	1.40	0.69	48	75	0.35	1.08	49	40
Case 2B	1.33	0.095	51	96	0.38	10.1	49	28
Case 2C	1.40	0.063	48	98	0.35	15.5	49	26
Case 3	1.35	0.056	49	98	0.37	17.5	49	26

τ_{DA} is the donor fluorescence lifetime in the presence of acceptor. The (FRET) transfer efficiency is determined from $E=1-\tau_{DA}/\tau_D$; τ_D is the fluorescence lifetime in the absence of acceptor and taken as 2.71 ns (see Table 1). The rate constant of energy transfer (k_T) is determined from $k_T=1/\tau_{DA}-1/\tau_D$. The distance R is obtained from $k_T= \tau_D$-$1(R_0/R)^6$, in which the critical transfer distance R_0 = 49 Å. The three different cases are referred to in Table 1. Case 1 refers to inclusion of all fluorescence lifetimes in calculation of the average fluorescence lifetime τ_{DA}. Case 2 refers to inclusion of only fluorescence lifetimes involved in FRET in calculation of τ_{DA}. A: analysis of one experiment with 100 nM YC3.60; B: global analysis of 6 different experiments (100 nM YC3.60) linking common parameters; C: analysis of one experiment with 500 nM YC3.60. Case 3 is restricted to FRET parameters obtained from acceptor fluorescence rise times.

efficiency of YC3.60 changed upon Ca^{2+} addition from 35 % to 52 % (case 1: all lifetime components and relative amplitudes are included in calculation of the average donor fluorescence lifetime). The FRET efficiencies become larger for case 2A (unquenched donor fluorescence lifetimes are excluded in the calculation of the average donor fluorescence lifetime), 48% (-Ca^{2+}) and 75% (+Ca^{2+}), respectively. The average rise times of case 3 (directly yielding the average donor fluorescence lifetime) show a transfer efficiency increase from 49% (-Ca^{2+}) to 98% (+Ca^{2+}). The slow average rise time in YC3.60 (- Ca^{2+}) is in good agreement with the corresponding average donor fluorescence lifetime (cases 2A-C). The results of these experiments are therefore internally consistent. The fast rise time 0.056 ns for YC3.60 (+ Ca^{2+}) is much faster than the corresponding donor fluorescence lifetime (0.69 ns) obtained from analysis of a single experiment (case 2A), but in good agreement with the value of 0.095 ns obtained from global analysis of multiple experiments (case 2B) and in even better agreement with the 63-ps lifetime of the single experiment at relatively high YC3.60 concentration (case 2C). It should be noted that a single rise time is more straightforward to obtain than the average decay time of the donor fluorescence obtained after 4-exponential decay analysis with constrained conditions such as the presence of a certain percentage of non-quenched donor molecules and of impurity fluorescence. All these data are collected in Table 4. Transfer rate constants and distances between the ECFP and Venus moieties within YC3.60 are collected in Table 4 as well for all cases. A distance of 4.9 nm is the same as the critical transfer distance R_0 and can therefore accurately be determined, whereas a distance of 2.6 nm is so short that it corresponds to an energy transfer efficiency approaching 100%, making this distance less determined. The "corrected" FRET efficiencies are more realistic than the 'raw' FRET efficiencies. FRET efficiencies and transfer rate constants determined from acceptor fluorescence rise times have the particular advantage that only the partners contributing to FRET are selected.

2.4.4 Acceptor photobleaching

APB experiments emphasize the emission properties of the donor before and after bleaching of the acceptor. It is therefore relevant to compare FRET efficiencies obtained from donor fluorescence lifetimes (table 4: cases 1 and 2) and from APB. FRET efficiencies of 39% (- Ca^{2+}) and 59% (+ Ca^{2+}) were found from APB experiments. These values are in good agreement with FRET efficiencies determined from lifetime data of case 1 (table 4: 35% (- Ca^{2+}) and 52% (+ Ca^{2+})). The calculated donor lifetimes composed of 20% non-interacting CFP and 80% interacting CFP molecules (table 4: case 2A) resulted in average fluorescence lifetimes of 1.67 ns (- Ca^{2+}) and 1.10 ns (+ Ca^{2+}) yielding FRET efficiencies of 39% and 60%, respectively, which is in excellent agreement with those found by the APB method. An important conclusion is that the APB method is not able to resolve heterogeneity in the donor population. This conclusion is in sharp contrast with the method of determination of donor fluorescence lifetimes, in which two distinct populations of donor molecules can be distinguished: one fraction is involved in the FRET process while the other fraction is not.

2.4.5 Fluorescence anisotropy decay

With fluorescence anisotropy one measures the change in orientation of transition dipole moments. The time-resolved fluorescence anisotropy of YC3.60 in the absence of calcium shows an initial rapid decay followed by a much slower decay (figure 3, curve 1). In the case of the Ca^{2+}-bound form of YC3.60 the first part of the decay is even more rapid and reaches a negative anisotropy value before it slowly rises to zero (figure 3, curve 2). The rapid decay is the characteristic time needed to change the transition dipole orientation of the initially photo-selected donor molecules to the transition dipole orientation of the acceptor molecules. However, one should realize that this energy transfer process occurs without radiation impeding to monitor the time-dependent initial depolarization of the acceptor. The early fluorescence signal in the acceptor channel is composed of two other sources, namely some remainder of ECFP emission (crosstalk) and emission from Venus arising from direct excitation. The fluorescence carrier signal for observing the anisotropy change is therefore provided by fluorescence photons from ECFP and/or Venus that are not participating in the energy transfer process. A two-component analysis was used to fit the experimental time-resolved anisotropy data. The short correlation time arising from energy transfer changed from 1.29 ns (-Ca^{2+}) to 0.056 ns (+Ca^{2+}) (table 2). These correlation times are in excellent agreement with the 'transfer' times obtained from the rise of acceptor fluorescence leading essentially to the same rates and efficiencies of energy transfer. The long correlation time of YC3.60 was obtained by direct excitation and emission detection of the Venus part and fixed in the analysis (see figure 4). The pre-exponential factors (*β*) of the fluorescence anisotropy decay (table 2) can be related to geometrical parameters describing the relative change in transition dipole moment orientations of ECFP and Venus in the YC3.60 complex. Because of experimental limitations the initial anisotropy is clearly smaller than the expected one $r_0 \approx 0.37$ (Borst et al. 2005). One can then estimate the angle between the transition dipole moments of the chromophores in ECFP and Venus (θ_T) of YC3.60 from the amplitude β_2 connected to the rotation part of the anisotropy, as this amplitude can be more reliably estimated (see confidence limits of β_2 in table 2) (Tanaka and Mataga 1979):

$$\beta_2 = \frac{2}{5}\frac{3\left\langle \cos^2\theta_{Donor\ excitation \rightarrow Acceptor\ emission}\right\rangle - 1}{2} \cong r_0 \frac{3\left\langle \cos^2\theta_T \right\rangle - 1}{2} \qquad (2)$$

No crosstalk is assumed in eq. 2. Taking $r_0 \approx 0.37$ we determined an angle $\theta_T = 46°$ between the chromophores in YC3.60 in the absence of Ca^{2+}. Binding of Ca^{2+} changed the angle to $\theta_T = 62°$.

It is striking that the long rotational correlation times obtained from Venus excitation and detection are different for the two conformations of YC3.60: 50 ns for the calcium-bound and 31 ns for the calcium-free conformation. Since the rotational correlation time is for a given shape proportional to molecular mass and there is no mass change and only a small change in shape involved, this large change must have another origin. The reason for the much shorter correlation time must be sought in local flexibility of the Venus part in the calcium-free conformation, which can be considered as a more flexible structure (see also discussion of FCS measurements below). This type of flexibility measured by fluorescence anisotropy decay has been observed previously for GFP linked to a single-chain antibody (Hink et al. 2000). Hink and coworkers (Hink et al. 2000) have discussed this observation by referring to simulations of the fluorescence anisotropy decay of two rigid proteins connected by a flexible hinge (Harvey 1979; Harvey and Cheung 1980). An important outcome of these simulations is that the emission transition dipole of the Venus part can sample the flexibility of the hinge between two relatively rigid proteins, while the fluorescence anisotropy decay remains single exponential with a shorter correlation time. This is apparently the case for the calcium-free form of YC3.60. In contrast, the calcium-bound YC3.60 rotates as a rigid body with a 50-ns correlation time, which is in agreement with a protein complex of this size. To obtain an estimate of the correlation time characteristic for this flexibility we have reanalyzed the fluorescence anisotropy decay of calcium-free YC3.60 with a biexponential decay model in which the long correlation time was fixed to 50 ns and the shorter correlation time treated as a free adjustable parameter. The results of this analysis have been incorporated in Table 2. The fit quality was the same as for a single-component analysis, but a short correlation time of 5 ns shows up in agreement with the FCS rotational diffusion experiments described in the next section.

2.4.6 FCS experiments

The results from the FCS experiments are consistent with the anisotropy measurements by single-photon timing and support the idea of a flexible structure for YC3.60 in absence of Ca^{2+}. Similar to the anisotropy decay data FCS also shows a significantly smaller mean rotational correlation time for this sample (t_3 = 33.2±1.1 ns in fit 1) as compared to the calcium bound species (t_3 = 43.7±1.5 ns in fit 1). This difference is much bigger than one would expect for rigid structures: A simulation of the rotational diffusion using HYDROPRO software (Garcia de la Torre et al. 2000) with PDB-data derived from the proposed structures (figure 6, next section) and assuming the recommended bead radius of 3.1 Å, which is a measure for solvation, yields mean correlation times of 50.7 ns ($-Ca^{2+}$) and 46.4 ns ($+Ca^{2+}$). If the bead radius is reduced to 2 Å, correlation times of 46.6 ns ($-Ca^{2+}$) and 43.0 ns ($+Ca^{2+}$) are obtained, which is very close to the experimentally observed values and supports the structural model in figure 6. Another outcome of the simulation is the small deviation of the five characteristic relaxation times from the mean for both structures of less than 9%. This justifies the assumption of a spherical shape and the treatment of the correlation data with an approximated model for spherical particles. The simulation predicts a slightly higher rotational correlation time for the open structure. The experimentally observed difference in the mean rotational correlation times with the closed structure exhibiting a longer time by 10 to 20 ns therefore cannot be attributed to a change in shape but rather to a conformational flexibility of protein structure in absence of calcium. Both TCSPC and FCS consistently found a characteristic relaxation time due to this conformational motion in the range of 5 to 15 ns.

2.4.7 Cartoon representation of YC3.60 structures

To translate FRET-efficiency and hydrodynamic changes into structural changes it is highly desirable to build a molecular model of YC3.60 in both conformations for visualization purposes. Based on X-ray crystallography and fluorescence data we were able to design a realistic structural model of the two fluorescent protein moieties and the calmodulin-M13 complex of YC3.60 ($-/+ Ca^{2+}$) using the obtained distances and orientational angles (case 3). In the closed calcium-bound conformation a distance of 2.6 nm between the chromophores and a relative angle of 62° between the transition dipole moments were used for construction. For the structural model of the open conformation ($-Ca^{2+}$), values of 4.9 nm and 46° were used. The short distance of 2.6 nm originates from the fact that the FRET efficiency approaches 95% resulting in the shortest possible distance. In the closed conformation (figure 6A) the two fluorescent proteins are positioned adjacent to each other and the calmodulin is wrapped around the M13 peptide. In the open conformation the fluorescent proteins remain close to the calmodulin, but the M13 peptide is released from the calmodulin domain (figure 6B).

The anisotropy experiments only yield the angle between the transition dipole moments of ECFP and Venus (θ_T), but not the angles θ_D and θ_A that the donor and acceptor transition moment make with the separation vector and that are also determining the orientation factor κ^2 (Dale et al. 1979). For that reason, the exact value of κ^2 cannot be evaluated. The exact spatial coordinates of the chromophores are necessary to determine the influence of κ^2 on this system. In supplemental data (S2) the dependence of κ^2 on the angles θ_D and θ_A (at fixed θ_T) is graphically presented. κ^2 can adopt any value up to a maximal value for $\kappa^2 = 3$. When the structural models were built, it could be noticed that slight structural changes induced by slightly rotating the fluorescent protein around a flexible linker while keeping the same average distance between ECFP and Venus, indeed gave rise to any value of the orientation factor. In S2 it is also shown that a 5-fold change in orientation factor (from 0.5 to 2.5) only brings about a 1.3-fold increase in critical distance and thus actual distance indicating that the FRET process in YC3.60 is mainly distance dependent.

Finally, the correlation times recovered from anisotropy and FCS analysis are much slower than the characteristic times of the FRET process. Therefore the structural cartoons depicted in figure 6 must be considered as static models.

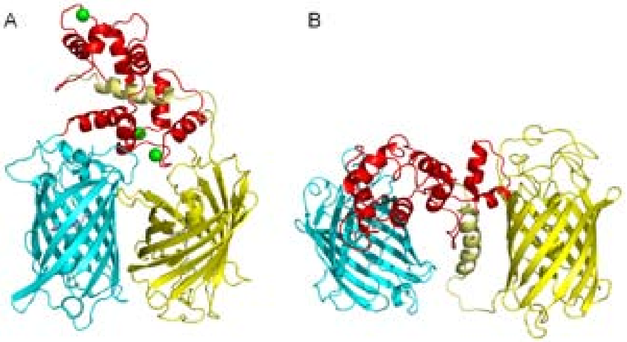

Figure 6. *Cartoon representation of YC3.60 in the closed (A) and open (B) conformation. Calcium ions are shown as green balls in the closed conformation. The left, cyan barrel (ECFP) is connected at the N-terminus of the red calmodulin part (A, top; B, middle). The C-terminus of the M13 peptide (gold) finally connects to the right, yellow barrel (Venus).*

2.5 Conclusions

In this work we used the rise time of acceptor fluorescence upon donor excitation to determine the rate of transfer from ECFP to Venus in the calcium sensor YC3.60. There are two advantages of this method as compared to measurements of the more conventional donor fluorescence lifetimes. The first advantage is that only FRET-active pairs are selected. The second advantage is that transfer rates can be accurately determined even in cases where FRET efficiencies are approaching 100% characterized by strongly quenched donor fluorescence intensities and ultrashort donor fluorescence lifetimes. From the transfer rate, the efficiency of transfer and the distance between both chromophores in YC3.60 can be determined. Since the transfer efficiency in the calcium-bound form of YC3.60 is approaching 100%, the distance between both fluorescent proteins must be so short that they must be nearly adjacent to each other. From the FRET parameters (distance, orientation) cartoon representations for calcium-free and calcium-bound conformations have been generated. The different structures have been compared with rotational diffusion properties of YC3.60 obtained with ensemble and single-molecule polarized fluorescence. There is excellent agreement between the hydrodynamic results of both methods. An important conclusion is that the rates of conformational fluctuations are smaller than the FRET rates implying a static regime of the FRET process. Summarizing, the here described time-resolved polarized fluorescence methodology can be used as a rapid method for the observation of ligand-dependent changes in structure and dynamics of biological macromolecules.

Supplementary material

S1. Analysis of the rise time in YC3.60 time-resolved fluorescence data.

To check whether it is possible to resolve two components in the time-dependent rise of acceptor fluorescence intensity, several simulations were performed, namely for YC3.60 in the presence of Ca^{2+} where the FRET efficiency is about 95% and for YC3.60 in the absence of Ca^{2+} where the FRET efficiency is about 50%. The rise times for the simulations were calculated from the lifetimes of CFP in case of 95% FRET efficiency ($\alpha_1 = 0.3$, $\tau_1 = 50$ ps, $\alpha_2 = 0.7$, $\tau_2 = 180$ ps) and of 50 % FRET efficiency ($\alpha_1 = 0.3$, $\tau_1 = 500$ ps, $\alpha_2 = 0.7$, $\tau_2 = 1800$ ps). In another simulation 3% of donor crosstalk (2.7 ns) in the acceptor detection window was allowed. The model used for the simulations was:

$$I = [A\{N_{pos} e^{-\frac{t}{\tau_A}} - N_{neg}(\sum_i \alpha_i e^{-\frac{t}{\tau_{ni}}})\} + Be^{-\frac{t}{\tau_D}}] \otimes Irf$$

where τ_A is the fluorescence lifetime of the acceptor, τ_D is the fluorescence lifetime of the unquenched donor, τ_{ni} are fluorescence rise times and α_i their relative amplitudes ($\sum_i \alpha_i = 1$), N_{pos} and N_{neg} are scaling factors, *B* is the amplitude that accounts for crosstalk of unquenched donor fluorescence, such that *A+B=1*, *Irf* is the instrumental response function and   is the convolution operator. The measured fluorescence decay of xanthione in ethanol with a fluorescence lifetime of 14 ps was used in the reference convolution method. A time scale of 1 ps/ch and 4000 data channels were used and Poissonian noise was added to the theoretical decay equivalent to a signal to noise ratio of experimentally observed fluorescence decay with approximately 2000 photons in the maximum of the curve.

Theoretical fluorescence traces of donor-excited YC3.60 in the acceptor detection window are presented in figure S1-1. It is immediately clear that the effect of spectral crosstalk (*B = 0.03 or B = 0.20*) is larger in case of slower rise times, since both curves are clearly separated. The results of the analysis of simulated data without crosstalk are presented in table S1-1 and in figure S1-2.

Table S1-1. *Parameters used during simulation and parameter estimates after single and double component analysis without crosstalk*

Input parameters for simulation					Single rise-time analysis			Double rise-time analysis					
α_1 (%)	τ_{n1} (ps)	τ_{n2} (ps)	$<\tau_n>$ (ps)	τ (ps)	τ_{n1} (ps)	τ (ps)	χ^2	α_1 (%)	τ_{n1} (ps)	τ_{n2} (ps)	$<\tau_n>$ (ps)	τ (ps)	χ^2
30	50	180	141	3100	145	3100	1.09	30	62	181	145	3100	1.03
30	500	1800	1410	3100	897	3100	1.82	28	470	1600	1283	3100	1.01

The first entry corresponds to parameters for YC3.60 in the absence of calcium. The second entry corresponds to those for YC3.60 in the presence of calcium.

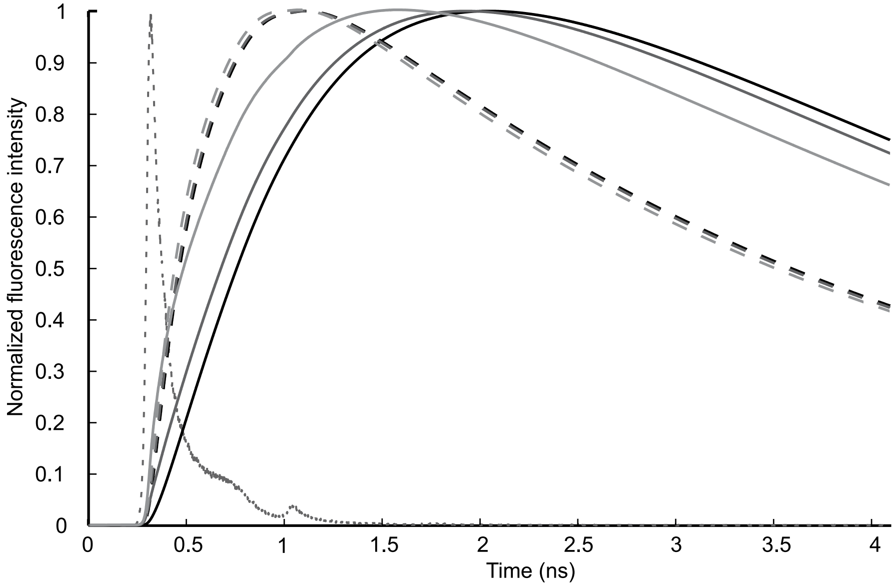

Figure S1-1*. Theoretical fluorescence traces of donor-excited YC3.60 in the acceptor detection window. Dashed lines represent data with a FRET efficiency of 95%, while solid lines represent data with a FRET efficiency of 50%. Black lines represent data without spectral crosstalk and grey lines (from dark grey to light grey) are data with respectively 3% and 20% of crosstalk. The IRF (dotted line) is also presented*

In case of 50% FRET efficiency (Fig. S1-2A) the recovered rise times (470 ps and 1600 ps) are close to the values used for the simulation (500 ps and 1800 ps) leading to an average lifetime of 1283 ps close to the expected one of 1410 ps (see table S1-1). The recovered values strongly depend on the estimated decay time of the acceptor. Analysis in this case should be done with a fixed fluorescence lifetime of the acceptor. In case of single-component rise time analysis it is observed that the average lifetime is even shorter (897 ps) (see table S1-1). In addition, the fit quality is worse than for a fit with two rise times (see χ^2 value in table S1-1 and residuals in figure S1-2A).

In case of 95% FRET efficiency (figure S1-2B) the two fast components (50 ps and 180 ps) are not completely recovered from the rising part of the acceptor fluorescence decay curve (62 ps and 181 ps, see table S1-1). The reason might be due to the finite width of the instrumental response function (~30 ps) and distortions induced by convolution. Analysis using the single-component model yields a rise time of 145 ps, which is very close to the average rise time of 141 ps (see table S1-1). The quality of the fit is similar for both single- and double-component analysis.

The effect of crosstalk in the analysis of simulated data has been presented in trable S1-2. By comparing the recovered time constants with those in the absence crosstalk (table S1-1) it can be concluded that the optimized rise times remain similar with a slight tendency for the longer average rise time to slightly increase with increasing percentage of crosstalk (from 1283 ps (0%), 1330 ps (3%) to 1670 ps (20%)).

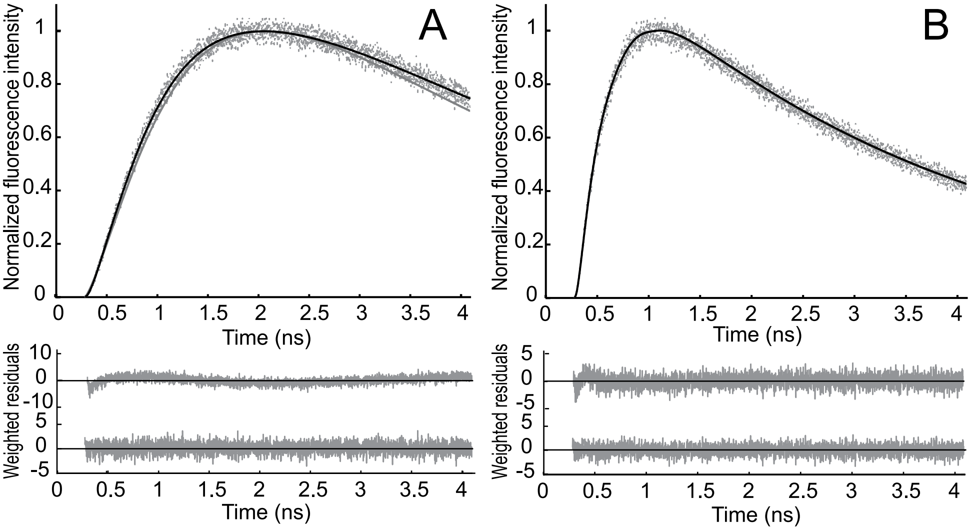

***Figure S1-2**. The results of the analysis of simulated data with donor excitation and acceptor detection without crosstalk. A: Simulated and fitted fluorescence decay of YC3.60 in the absence of Ca^{2+}; B: Simulated and fitted fluorescence decay of YC3.60 in the presence of Ca^{2+}, weighted residuals from a single-component analysis are shown in the upper panel and weighted residuals from a double-component analysis are shown in the lower panel.*

***Table S1-2.** Parameters used during simulation and parameter estimates after single and double component analysis with 3% and 20% of crosstalk.*

Input parameters for simulation					Single rise-time analysis			Double rise-time analysis					
α_1 (%)	τ_{n1} (ps)	τ_{n2} (ps)	$<\tau_n>$ (ps)	τ (ps)	τ_{n1} (ps)	τ (ps)	χ^2	α_1 (%)	τ_{n1} (ps)	τ_{n2} (ps)	$<\tau_n>$ (ps)	τ (ps)	$\chi 2$
3% of crosstalk													
30	50	180	141	3100	144	3100	1.05	29	53	176	140	3100	0.99
30	500	1800	1410	3100	912	3100	1.54	29	486	1675	1330	3100	0.99
20% of crosstalk													
30	50	180	141	3100	133	3100	1.03	18	43	147	128	3100	1.03
30	50	180	141	3100	969	3100	1.31	26	500	2082	1670	3100	1.03

An important conclusion is that a double-component intensity rise analysis clearly recovers the average donor fluorescence lifetime in the presence of acceptor $<\tau_{DA}>$, which can then be used for calculation of the FRET efficiency from $E = 1 - <\tau_{DA}>/<\tau_D>$. Short, average rise times are already recovered after a single-component analysis. The simulations showed that it is better to fix the long decay time in the analysis.

A considerable simplification is introduced, when there is only one donor fluorescence lifetime present.

S2. The orientation factor κ^2 in FRET

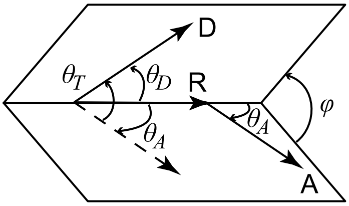

Figure S2-1. *Dependence of the orientation factor κ2 on the direction of transition dipole moments of donor and acceptor.*

The orientation factor κ^2 for a donor-acceptor pair depends on three orientation angles: the angle (θ_D) between the emission transition dipole moment of the donor ($\boldsymbol{\mu}_D$) and the line connecting the centres of the donor and acceptor chromophores, the separation vector **R**, the angle (θ_A) between the absorption transition dipole moment of the acceptor ($\boldsymbol{\mu}_A$) and the separation vector and the angle (θ_T) between transition dipole moments $\boldsymbol{\mu}_D$ and $\boldsymbol{\mu}_A$ (figure S2-1). Two planes are formed by $\boldsymbol{\mu}_D$ and R and by $\boldsymbol{\mu}_A$ and **R**, intersecting at **R** and under an angle φ. The "experimental" angle θ is equivalent to θ_T. The orientation factor can be expressed in two ways in terms of the various angles:

$$\kappa^2 = (\cos\theta_T - 3\cos\theta_D \cos\theta_A)^2$$
$$\kappa^2 = (\sin\theta_D \sin\theta_A \cos\varphi - 2\cos\theta_D \cos\theta_A)^2$$

One can make 3D plots of κ^2 (z-axis) versus θ_D (y-axis) and versus θ_A (x-axis) for certain values of θ_T and estimate lower and upper values of possible κ^2 values. These graphs are presented in Fig. S3 for both $\theta_T = 46°$ and $\theta_T = 62°$.

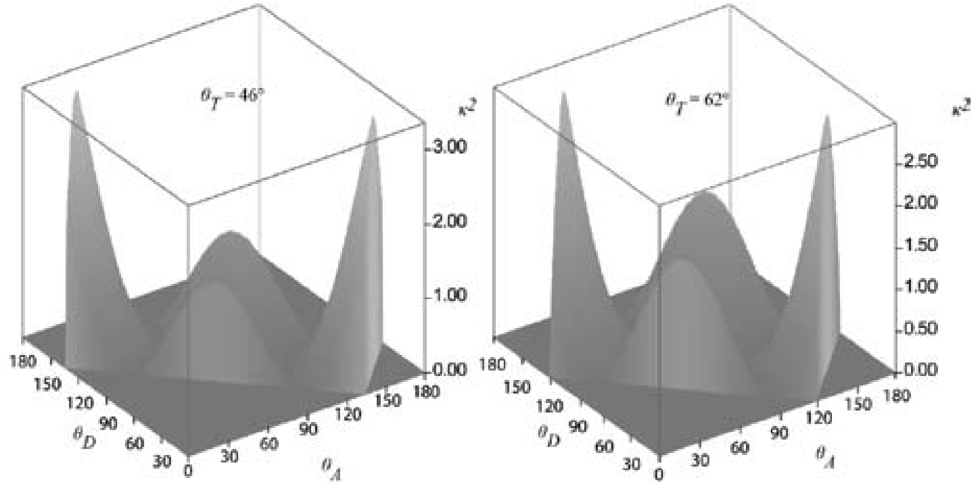

Figure S2-2. *Graphical presentations of κ^2 versus θ_D and θ_A for $\theta_T = 46°$ and $\theta_T = 62°$.*

From both graphs it can be noticed that the maximum value of κ^2 is between 2.5 ($\theta_T = 62°$) and 3 ($\theta_T = 46°$).

The critical transfer distance R_0 is plotted against κ^2 for the ECFP-Venus couple in Figure S2-3. When κ^2 changes from 0.5 to 2.5 the change in R_0 is from 4.5 nm to 5.9 nm, illustrating that a 5-fold increase of orientation factor brings about a 1.3-fold increase of critical distance. A very low value of $\kappa^2 = 0.1$ already yields a $R_0 = 3.2$ nm.

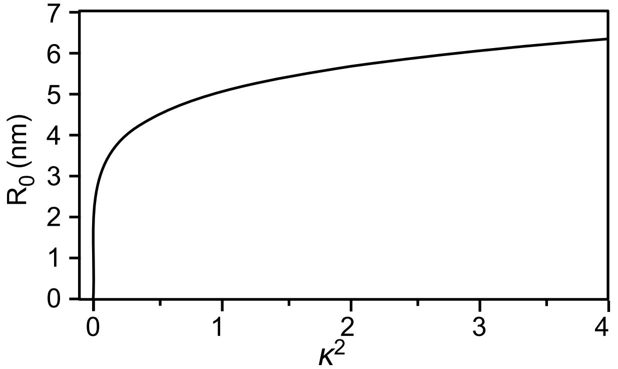

Figure S2-3. *The dependence of the critical distance R_0 on the orientation factor κ^2 in case of FRET between ECFP and Venus. The quantum yield of the donor is 0.39, the refractive index of the medium is assumed to be 1.33 and the spectral overlap integral is $1.55x10^{15}$ $nm^4M^{-1}cm^{-1}$.*

Acknowledgment

We thank Dr. A. Miyawaki (RIKEN Brain Science Institute, Saitama, Japan) for the YC3.60 plasmid. This research was funded by the Netherlands Organization for Scientific Research (ALW812.06.004 to JA), by the Sandwich Programme of Wageningen University (SL) and by the European Community (Marie Curie Research Training Network MRTN-CT-2005-019481 “From FLIM to FLIN”) (SL). CS thanks for the support of this work by the Deutsche Forschungsgemeinschaft (DFG) via the SFB 590 “Inherent and adaptive differentiation processes”.

References

Aragón, S. R. and R. Pecora (1975). Fluorescence correlation spectroscopy and brownian rotational diffusion. *Biopolymers* **14**: 119-138.

Bastiaens, P. I., I. V. Majoul, P. J. Verveer, H. D. Soling and T. M. Jovin (1996). Imaging the intracellular trafficking and state of the AB5 quaternary structure of cholera toxin. *EMBO J* **15**(16): 4246-53.

Boens, N., N. Tamai, I. Yamazaki and T. Yamazaki (1990). Picosecond single photon timing measurements with a proximity type microchannel plate photomultiplier and global analysis with reference convolution. *Photochem. Photobiol. Sci.* **52**: 911-917.

Borst, J. W., M. A. Hink, A. van Hoek and A. J. Visser (2005). Effects of refractive index and viscosity on fluorescence and anisotropy decays of enhanced cyan and yellow fluorescent proteins. *J Fluoresc* **15**(2): 153-160.

Camuzeaux, B., C. Spriet, L. Heliot, J. Coll and M. Duterque-Coquillaud (2005). Imaging Erg and Jun transcription factor interaction in living cells using fluorescence resonance energy transfer analyses." *Biochem. Biophys. Res. Commun.* **332**(4): 1107-1114.

Dale, R. E., J. Eisinger and W. E. Blumberg (1979). The orientational freedom of molecular probes. The orientation factor in intramolecular energy transfer. *Biophys. J.* **26**(2): 161-193.

DeLano, W. L. (2002). The PyMOL Molecular Graphics System. DeLano Scientific San Carlos CA, USA.

Demachy, I., J. Ridard, H. Laguitton-Pasquier, E. Durnerin, G. Vallverdu, P. Archirel and B. Levy (2005). Cyan fluorescent protein: Molecular dynamics, simulations, and electronic absorption spectrum. *J. Phys. Chem. B* **109**(50): 24121-24133.

Digris, A. V., V. V. Skakoun, E. G. Novikov, A. van Hoek, A. Claiborne and A. J. W. G. Visser (1999). Thermal stability of a flavoprotein assessed from associative analysis of polarized time-resolved fluorescence spectroscopy. *Eur. Biophys. J.* **28**: 526-531.

Ehrenberg, M. and R. Rigler (1974). Rotational brownian motion and fluorescence intensity fluctuations. *Chemical Physics* **4**: 390-401.

Enderlein, J., I. Gregor, D. Patra, T. Dertinger and U. B. Kaupp (2005). Performance of fluorescence correlation spectroscopy for measuring diffusion and concentration. *Chemphyschem* **6**(11): 2324-36.

Felekyan, S., R. Kühnemuth, V. Kudryavtsev, C. Sandhagen, W. Becker and C. A. M. Seidel (2005). Full correlation from picoseconds to seconds by time-resolved and time-correlated single photon detection. *Rev. Sci. Instr.* **76**(8): 83104-83118.

Förster, T. (1948). Zwischenmolekulare Energiewanderung und Fluoreszenz. *Ann. Phys.* **2**: 55-75.

Garcia de la Torre, J., M. L. Huertas and B. Carrasco (2000). Calculation of hydrodynamic properties of globular proteins from their atomic-level structure. *Biophys. J.* **78**:719-730.

Grailhe, R., F. Merola, J. Ridard, S. Couvignou, C. Le Poupon, J. P. Changeux and H. Laguitton-Pasquier (2006). Monitoring protein interactions in the living cell through the fluorescence decays of the cyan fluorescent protein. *ChemPhysChem* **7**(7): 1442-1454.

Habuchi, S., M. Cotlet, J. Hofkens, G. Dirix, J. Michiels, J. Vanderleyden, V. Subramaniam and F. C. De Schryver (2002). Resonance energy transfer in a calcium concentration-dependent cameleon protein. *Biophys. J.* **83**(6): 3499-3506.

Harpur, A. G., F. S. Wouters and P. I. Bastiaens (2001). Imaging FRET between spectrally similar GFP molecules in single cells. *Nat. Biotechnol.* **19**(2): 167-169.

Harvey, S. C. (1979). Transport properties of particles with segmental flexibility. I. Hydrodynamic resistance and diffusion coefficients of a freely hinged particle. *Biopolymers* **18**: 1081-1104.

Harvey, S. C. and H. C. Cheung (1980). Transport properties of particles with segmental flexibility. II. Decay of fluorescence polarization anisotropy from hinged macromolecules. *Biopolymers* **19**: 913-930.

Hink, M. A., R. A. Griep, J. W. Borst, A. van Hoek, M. H. M. Eppink, A. Schots and A. J. W. G. Visser (2000). Structural dynamics of green fluorescent protein alone and fused with a single chain Fv protein. *J. Biol. Chem.* **275**(23): 17556-17560.

Hink, M. A., N. V. Visser, J. W. Borst, A. van Hoek and A. J. W. G. Visser (2003). Practical use of corrected fluorescence excitation and emission spectra of fluorescent proteins in Förster resonance energy transfer (FRET) studies. *J. Fluoresc.* **13**(2): 185-188.

Ho, C. J., A. L. Motyka and M. R. Topp (1989). Picosecond time-resolved S2-S0 fluorescence of xanthione in different fluid solvents. *Chem. Phys. Lett.* **158**: 51-59.

Hyun Bae, J., M. Rubini, G. Jung, G. Wiegand, M. H. J. Seifert, M. K. Azim, J.-S. Kim, A. Zumbusch, T. A. Holak, L. Moroder, R. Huber and N. Budisa (2003). Expansion of the genetic code enables design of a novel "gold" class of green fluorescent proteins. *J. Mol. Biol.* **328**: 1071-1081.

Jares-Erijman, E. A. and T. M. Jovin (2003). FRET imaging. *Nat. Biotechnol.* **21**(11): 1387-95.

Jares-Erijman, E. A. and T. M. Jovin (2006). Imaging molecular interactions in living cells by FRET microscopy. *Curr Opin Chem Biol* **10**(5): 409-16.

Jose, M., D. K. Nair, C. Reissner, R. Hartig and W. Zuschratter (2007). Photophysics of Clomeleon by FLIM: discriminating excited state reactions along neuronal development. *Biophys. J.* **92**(6): 2237-2254.

Karolczak, J., D. Komar, J. Kubicki, T. Wrozowa, K. Dobek, B. Ciesielska and A. Maciejewski (2001). "The measurements of picosecond fluorescence lifetimes with high accuracy and subpicosecond precision." Chem. Phys. Lett. 344: 154-164.

Kask, P., P. Piksarv, M. Pooga, Ü. Mets and E. Lippmaa (1989). Separation of the rotational contribution in fluorescence correlation experiments. *Biophys. J.* **55**: 213-220.

Kühnemuth, R. and C. A. M. Seidel (2001). Principles of Single Molecule Multiparameter Fluorescence Spectroscopy. *Single Molecule* **2**(4): 251-254.

Kulinski, T., A. J. W. G. Visser, D. J. O'Kane and J. Lee (1987). Spectroscopic investigations of the single tryptophan residue and of riboflavin and 7-oxolumazine bound to lumazine apoprotein from *Photobacterium leiognathi. Biochemistry* **26**(2): 540-9.

Mets, Ü. (2001). Antibunching and rotational diffusion in FCS. Berlin Heidelberg New York, Springer-Verlag.

Millington, M., G. J. Grindlay, K. Altenbach, R. K. Neely, W. Kolch, M. Bencina, N. D. Read, A. C. Jones, D. T. Dryden and S. W. Magennis (2007). High-precision FLIM-FRET in fixed and living cells reveals heterogeneity in a simple CFP-YFP fusion protein. *Bio-*

phys. Chem. **127**(3): 155-164.

Miyawaki, A., O. Griesbeck, R. Heim and R. Y. Tsien (1999). Dynamic and quantitative Ca^{2+} measurements using improved cameleons. *Proc. Natl. Acad. Sci. USA* **96**(5): 2135-2140.

Miyawaki, A., J. Llopis, R. Heim, J. M. McCaffery, J. A. Adams, M. Ikura and R. Y. Tsien (1997). Fluorescent indicators for Ca^{2+} based on green fluorescent proteins and calmodulin. *Nature* **388**(6645): 882-887.

Nagai, T., K. Ibata, E. S. Park, M. Kubota, K. Mikoshiba and A. Miyawaki (2002). A variant of yellow fluorescent protein with fast and efficient maturation for cell-biological applications. *Nat. Biotechnol.* **20**(1): 87-90.

Nagai, T., S. Yamada, T. Tominaga, M. Ichikawa and A. Miyawaki (2004). Expanded dynamic range of fluorescent indicators for Ca^{2+} by circularly permuted yellow fluorescent proteins. *Proc. Natl. Acad. Sci. USA* **101**(29): 10554-10559.

Patterson, G. H., S. M. Knobel, W. D. Sharif, S. R. Kain and D. W. Piston (1997). Use of green fluorescent protein and its mutants in quantitative fluorescence microscopy. *Biophys. J.* **73**(November): 2782-2790.

Rosell, F. I. and S. G. Boxer (2003). Polarized absorption spectra of green fluorescent protein single crystals: Transition dipole moment directions. *Biochemistry* **42**(1): 177-183.

Schaffer, J., A. Volkmer, C. Eggeling, V. Subramaniam, G. Striker and C. A. M. Seidel (1999). Identification of single molecules in aqueous solution by time-resolved fluorescence anisotropy. *Journal of Physical Chemistry A* **103**(3): 331-336.

Seifert, M. H., D. Ksiazek, M. K. Azim, P. Smialowski, N. Budisa and T. A. Holak (2002). Slow exchange in the chromophore of a green fluorescent protein variant. *J. Am. Chem. Soc.* **124**(27): 7932-7942.

Smith, D. B. and K. S. Johnson (1988). Single-Step Purification of Polypeptides Expressed in Escherichia coli as Fusions with Glutathione S-Transferase. *Gene* **67**(1): 31-40.

Stryer, L. (1978). Fluorescence energy transfer as a spectroscopic ruler. *Annu. Rev. Biochem.* **47**: 819-846.

Suhling, K., P. M. W. French and D. Phillips (2005). Time-resolved fluorescence microscopy. *Photochem. Photobiol. Sci.* **4**(1): 13-22.

Tanaka, F. and N. Mataga (1979). Theory of time-dependent photo-selection in interacting fixed systems. *Photochem. Photobiol.* **29**: 1091-1097.

Tramier, M., I. Gautier, T. Piolot, S. Ravalet, K. Kemnitz, J. Coppey, C. Durieux, V. Mignotte and M. Coppey-Moisan (2002). Picosecond-hetero-FRET microscopy to probe protein-protein interactions in live cells. *Biophys. J.* **83**(6): 3570-3577.

van den Berg, P. A. W., K. A. Feenstra, A. E. Mark, H. J. C. Berendsen and A. J. W. G. Visser (2002). Dynamic conformations of flavin adenine dinucleotide:simulated molecular dynamics of the flavin cofactor related to time-resolved fluorescence characteristics. *J. Phys. Chem. B* **106**: 8858-8869.

van den Berg, P. A. W., A. van Hoek and A. J. W. G. Visser (2004). Evidence for a novel mechanism of time-resolved flavin fluorescence depolarization in glutathione reductase. *Biophys. J.* **87**(4): 2577-2586.

van Dongen, E. M., L. M. Dekkers, K. Spijker, E. W. Meijer, L. W. Klomp and M. Merkx (2006). Ratiometric fluorescent sensor proteins with subnanomolar affinity for Zn(II) based on copper chaperone domains. *J. Am. Chem. Soc.* **128**(33): 10754-10762.

Vinkenborg, J. L., T. H. Evers, S. W. Reulen, E. W. Meijer and M. Merkx (2007). Enhanced sensitivity of FRET-based protease sensors by redesign of the GFP dimerization interface. *Chembiochem* **8**(10): 1119-1121.

Visser, N. V., J. W. Borst, M. A. Hink, A. van Hoek and A. J. W. G. Visser (2005). Direct observation of resonance tryptophan-to-chromophore energy transfer in visible fluorescent proteins. *Biophys. Chem.* **116**: 207-212.

Vos, K., A. van Hoek and A. J. W. G. Visser (1987). Application of a reference deconvolution method to tryptophan fluorescence in proteins. A refined description of rotational dynamics. *Eur. J. Biochem.* **165**: 55-63.

Widengren, J., V. Kudryavtsev, M. Antonik, S. Berger, M. Gerken and C. A. Seidel (2006). Single-molecule detection and identification of multiple species by multiparameter fluorescence detection. *Anal Chem* **78**(6): 2039-50.

Chapter 3

Picosecond fluorescence spectroscopy of the calcium sensor YC3.60.

based on:
S. P. Laptenok, I. H. M. van Stokkum, J. W. Borst, A. J. W. G. Visser, H van Amerongen,
Picosecond fluorescence spectroscopy of the calcium sensor YC3.60.
in preparation

Abstract

A significant number of fluorescent dyes has been developed that are used as indicators for cell viability, nuclear staining, determining calcium concentrations and many other cellular parameters. In this study time-resolved fluorescence spectra with picosecond time resolution of the calcium sensor yellow cameleon 3.60 (YC3.60) in aqueous solution have been measured and globally analyzed. YC3.60 is composed of a calmodulin domain and a M13 peptide, which are located in between the fluorescent proteins ECFP and the Venus variant of EYFP. Their action is based on radiation-less excitation energy transfer from ECFP to Venus, the efficiency of which becomes larger when calcium is bound. Global target analysis of streak images of purified YC3.60 in calcium-free and calcium-bound conformations yield detailed insight in the FRET kinetics, and demonstrate the complications that can be expected when applying ratio imaging.

3.1 Introduction

Genetically encoded sensors have become a powerful tool for investigating cellular signaling pathways. Cellular processes can even be visualized in real time through the use of sensors that are based on the green fluorescent protein (GFP) (Tsien 1998) for specific intracellular constituents (Guerrero and Isacoff 2001; Zhang, Campbell et al. 2002). Many of these sensors use changes in Förster resonance energy transfer (FRET) efficiency between donor and acceptor variants of GFP separated by a ligand binding domain that is sensitive to a particular signaling pathway.

FRET in aqueous solution is a photophysical process where the excited-state energy from a donor molecule is transferred non-radiatively to an acceptor molecule at close distance (< 10 nm) via weak dipole-dipole coupling (Förster 1949). Since FRET only occurs between molecules in close proximity, it can be used as a spectroscopic ruler to investigate interactions and conformational changes in biological macromolecules (Stryer 1978; Jares-Erijman and Jovin 2006). The occurrence of FRET requires spectral overlap between donor emission and acceptor absorption spectra. The energy transfer efficiency is inversely proportional to the sixth power of the distance (R) between donor and absorption.

Changes in free calcium concentration play an important role in many biological processes. Therefore, much effort has been spent on the development of systems for imaging calcium fluxes. The creation of genetically encoded fluorescent protein sensors for intracellular Ca^{2+} has the potential to enable studies of calcium signaling *in vivo*, which are difficult or impossible with the widely used chemically synthesized fluorescent indicators (Miyawaki et al. 1997; Baird et al. 1999). Cameleon sensors are fluorescent calcium indicators composed of genetically encoded protein constructs without any cofactors (Miyawaki et al. 1997; Miyawaki et al. 1999; Nagai et al. 2004). The cameleon variant YC3.60 is a fusion of an ECFP (donor) and an EYFP derivative (Venus) moiety (acceptor) linked by calmodulin and a calmodulin binding peptide of myosin light chain kinase (M13). The binding of calcium ions to calmodulin makes calmodulin wrap around the M13 domain increasing the FRET efficiency from ECFP to Venus.

Recently improved imaging technology in cell biology (Gabriel and Teissié 1998;

Agronskaia et al. 2004) allows imaging of biophysical processes in living cells with high speed and accuracy using genetically encoded fluorescence sensors. However for quantitative analysis of the data observed for live cells, an accurate study of the fluorescence dynamics of sensors *in vitro* is mandatory. Therefore, we measured the time-resolved spectra of YC3.60 with and without calcium with a picoseconds synchroscan system and performed detailed data analysis. The present investigation is an extension of the previously reported single-photon timing study of YC3.60, which has been obtained at less time resolution and at only two detection wavelengths of the fluorescence. (Borst et al. 2008)

3.2 Materials and methods

3.2.1 Time-resolved fluorescence using the streak-camera setup

Picosecond fluorescence spectra measurements were performed using a synchroscan streak camera system. Excitation light pulses were obtained with a set of lasers and optical amplifiers from Coherent Inc., Santa Clara, CA, USA. A mode-locked Ti:Sapphire laser model Mira 900 was used to generate short light pulses of 800 nm with an average power of 0.5 W, duration of about 200 fs and repetition rate of 79.5 MHz. A small fraction of the output of this laser is used for synchronization with a sweep field in the streak camera, while the major part was fed into a regenerative amplifier model RegA 9000, where the energy of the pulses is increased while the repetition rate is decreased to 250 kHz. Continuous wave solid state lasers (Coherent Verdi V5 and Coherent Verdi V10) were used to pump a Mira and RegA, respectively. The output of the RegA is directed to an optical parameter amplifier (OPA 9400) which is used to produce excitation pulses of all wavelengths longer than 235 nm. The average output of the OPA was 300 mW. The light intensity was modulated with neutral density filters and residual white light of the OPA was removed with an interference filter. Vertical polarization of the excitation light was set with a Berek polarizer model 5540 (New Focus, San Jose, CA, USA). A lens with a focal length of 15 cm focused the light into the sample in a static quartz cuvette of 1.0 x 0.4 cm at room temperature. In front of the streak camera an imaging spectrograph was mounted (model 250is, Chromex, Albuquerque, NM, USA). Fluorescence emission was focused into the input slit of the spectrograph, using two identical achromatic lens assemblies (model UV APO special, f = 70 mm, d = 22 mm, Sill Optics, Wendelstein, Germany) placed in a complementary manner with a Glan Taylor polarizer (model GT20, Leysop Ltd., Essex, England) and an optical cut-off filter 408 nm in between to suppress scatter. The detection polarizer was set at magic angle orientation. The output of the spectrograph was coupled directly onto the stripe-shaped (height 70 μm) cathode of the streak-camera (model C5680 with model M5675 Synchroscan unit, Hamamatsu Photonics K.K., Hamamatsu City, Japan). The wavelength dispersion of the spectrograph was in the horizontal direction, the time dispersion of the streak tube was in the vertical direction.

The instrument response function (IRF) $i(t)$ can be satisfactory modeled with a Gaussian with parameters μ and Δ for location and full width at half maximum (FWHM), respectively:

$$i(t) = \frac{1}{\tilde{\Delta}\sqrt{2\pi}} \exp(-\log(2)(2(t-\mu)/\Delta)^2)$$

where $\tilde{\Delta} = \Delta/(2\sqrt{2\log(2)})$. Location (μ) and FWHM (Δ) of the IRF were free fit parameters. The wavelength dependence of the location of the IRF was described by a parabola (wavelength vs. time) resulting in two extra free parameters. For more technical details about streak camera experiments see (van Stokkum et al. 2008; van Oort et al. 2009)

3.2.2 Streak camera data-analysis

The aim of the analysis is to obtain a model-based description of the data in terms of a small number of precisely estimated parameters. The rate constants and spectra are usually the most relevant parameters for describing time-resolved spectroscopy data.

Time-resolved spectroscopy data can be stored as a matrix $\mathbf{\Psi}$, where each column represents a fluorescence decay at certain wavelength and each row represents a fluorescence spectrum at a given time. The basis for global analysis is the superposition principle, which is the assumption that measured data result from a linear combination of n_{comp} components, each with a distinct time profile **C**[,*j*] and spectrum **E**[,*j*], giving rise to the equation where $\mathbf{\Psi}$ is the $m \times n$ matrix representing measured data, the $m \times n_{comp}$ matrix **C** and the $n \times n_{comp}$ matrix **E** represent the components in the time and wavelength domain, respectively. Using least square criteria, the fitting problem can be written as $\min \left\| \mathbf{\Psi} - \mathbf{C}\mathbf{E}^T \right\|^2$. It is also often the case that a parametric description of either **C** or **E**, but not both matrices, is available. In most cases matrix **C** can be described with a compartmental model, which describes a set of first-order differential equations, with a sum of exponential decays as a solution. In this case the parameter estimation problem associated with fitting the model for $\mathbf{\Psi}$ can be formulated as:

$$\min_{k \in R_q} \left\| \mathbf{\Psi} - \mathbf{C}(k)\mathbf{E}^T \right\|^2$$

where *k* denotes the set of the kinetic parameters, which describes a compartmental model that was used for the analysis. Depending upon the compartmental model the global analysis yields Decay Associated Spectra (DAS) in case of compartments decaying mono-exponentially in parallel, or Evolution Association Spectra (EAS) when a sequential model with increasing lifetimes is used. The full compartmental scheme, which includes all possible branching or equilibria between compartments, leads to Species Associated Spectra (SAS). For more details about using compartmental models for global and target analysis of time-resolved spectroscopy data see reviews by Holzwarth (Holzwarth 1996) and van Stokkum and co-workers (van Stokkum et al. 2004; van Stokkum et al. 2008). For details on parameters estimation techniques see (van Stokkum and Bal 2006; Mullen et al. 2007).

3.2.3 Protein material, sample preparation and collection of streak images

cDNA of YC3.60 was kindly provided by Dr. Atsitsu Miyawaki (RIKEN Brain Science Institute, Saitama, Japan). The full length sensor was cloned into the GST fusion vector (pGEX5x2 vector). The YC3.60 was isolated and purified as previously described (Smith and Johnson 1988; Borst et al. 2008). The purity of the YC3.60 protein was analyzed on SDS-PAGE and a single band of approximately 75 kDa without degradation products was observed. A stoichiometry of 1:1 between ECFP and the Venus moiety was determined by size exclusion chromatography and absorption spectroscopy. 15 µl of YC3.60 was diluted in 750 µl PBS buffer pH 7.4 containing either 0.5 µl EGTA or 0.1 µl of Ca^{2+}.

Streak-images of YC3.60 in a Ca-free and Ca-bound conformation were measured upon excitation with 400-nm laser light with vertical polarization and 200 µW average power. The fluorescence was detected at magic angle polarization. Images of YC3.60 in the calcium bound conformation were measured at two time ranges (800-ps time window – time range2 (tr2) and 2-ns time window – time range 4 (tr4)). For YC3.60 in the calcium-free conformation images were measured only at tr4. All measurements were performed at room temperature.

The series of 50 images, each taken with 10-sec acquisition time, were corrected for the presence of jitter, background and shading and averaged using the High Performance Digital Temporal Analyzer (HPDTA, Hamamatsu Photonics). Corrected streak images of YC3.60 from all experiments were analyzed globally. Decay rate constants were linked between all datasets while transfer rate constants were linked only between experiments with the same sample (YC3.60 in the presence or absence of calcium).

3.3 Results and discussion

3.3.1 Streak images and global analysis

Figure 1 shows streak images of YC3.60 in calcium-free (A) and calcium-bound (B) conformations measured at tr4.

Due to a difference in time jitter, the FWHM of the IRF for calcium-bound YC3.60 was somewhat larger than for calcium free YC3.60, and the scatter peak at 400 nm in figure 1B is wider in time than that in figure 1A. It is clear from the images that the fluorescence in the blue part of the spectrum is disappearing much faster in calcium-bound YC3.60 as compared to calcium-free YC3.60, which is due to excitation energy transfer (see below). The spectral interval from 440 nm to 640 nm was selected for analysis and sliced into 50 time traces which corresponds to a spectral resolution of 4 nm.

Global analysis of a single data set shows that at least four components and corresponding lifetimes are needed to describe the multi-exponential decay of the emission. Furthermore, a large Raman scatter peak is present near 465 nm, which complicates the analysis.

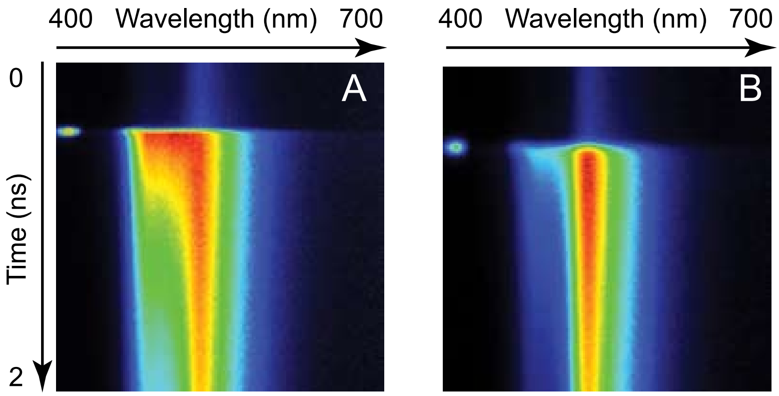

***Figure 1**. Streak images of YC3.60 in the absence of calcium (A) and in the presence of calcium (B) measured at tr4 after averaging, jitter-, background-, and shading correction. Fluorescence intensity is represented by colors from red (high) to black (low).*

Figure 2 represents the estimated decay associated spectra (DAS) for calcium-free (A) and calcium-bound (B) conformations estimated from global analysis, using a parallel decaying model (van Stokkum et al. 2004). In YC3.60 without calcium (figure 2A) the 1.4-ns DAS (blue line) is conservative, *i.e.* has more or less equal positive and negative areas, and it represents decay in the blue part of the spectrum and rise in the red part of the emission, which should be interpreted as energy transfer from ECFP to YFP-Venus chromophores. In contrast, the 329-ps DAS (green line) is not conservative, it shows substantially less rise in the red part of the emission. The positive area of the spectrum is far bigger than the negative one, and apparently a (unknown) decay process is occurring on this time scale, concurrently with energy transfer. Next two DAS (cyan and red) with lifetimes of 2.5 and 2.7 ns, respectively, can be attributed to the fluorescence decay of non-interacting ECFP and YFP-Venus in YC3.60. Based on the steady-state fluorescence spectrum of YFP-Venus the DAS represented by the

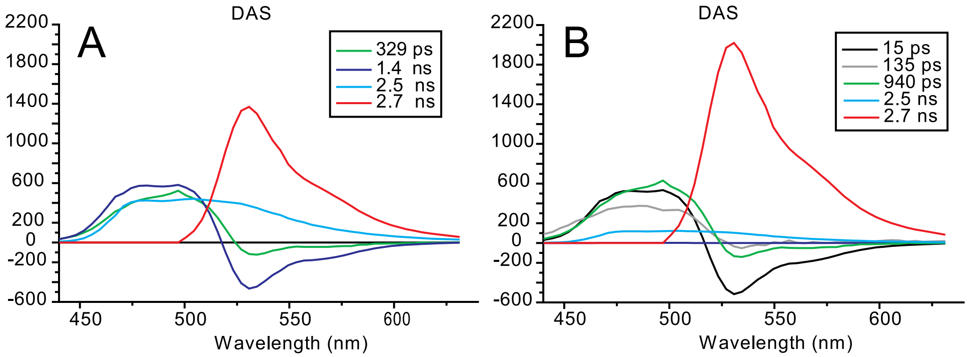

Figure 2. *Decay associated spectra (DAS) for YC3.60 in the absence of calcium (A) and in the presence of calcium (B). Note that the DAS represented by the red lines was set to 0 below 490 nm during analysis.*

red line was set to 0 below 490 nm.

In YC3.60 in the presence of calcium (figure 2B) the first 15-ps DAS (black) is conservative and it represents energy transfer from ECFP to YFP-Venus. The 135-ps and 940-ps DAS are not conservative and show mostly a decay in the blue part of the spectrum, and only a small part of rise component around 530 nm. Similar to the YC3.60 without calcium two long-lived DAS (cyan and red) with lifetimes of 2.5 and 2.7 ns, respectively, are also present and can be attributed to non-interacting ECFP and YFP-Venus chromophores. The green DAS in the YC3.60 without calcium and the green and grey DAS in the YC3.60 with calcium do not represent pure species (*i.e.* the spectra do not correspond to the fluorescence of either ECFP or YFP-Venus only), but should be interpreted as linear combinations of the species spectra. There is a fraction of non-transferring ECFP present in both the presence and absence of Ca^{2+} but the amount is smaller in the Ca^{2+}-bound case. In both conformations there are two major rise components present in the YFP-Venus fluorescence region with different time constants.

3.3.2 Target analysis

For a simultaneous target analysis of all three data sets (YC3.60 in the absence of calcium measured at tr4 and YC3.60 in the presence of calcium measured at tr4 and tr2), it is necessary to use a model with at least six compartments in order to obtain a satisfactory description of the data. Figure 3 shows the kinetic scheme that was used for the global target analysis of the time-resolved spectra of YC3.60. To resolve all kinetic parameters involved in modeling, several spectral constraints had to be applied to the target model.

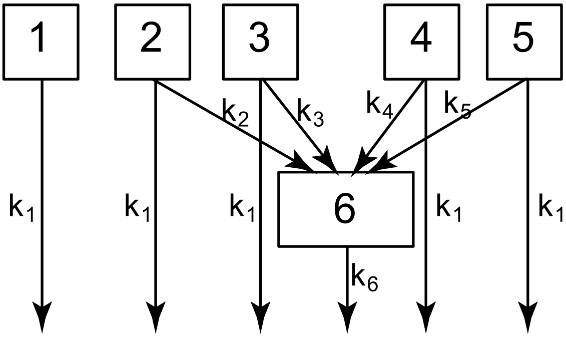

Figure 3. *Kinetic scheme used for global target analysis of YC3.60 data.*

The spectra of compartments 2 and 3 are assumed to be the same, since they are associated with the fluorescence from two different conformations of the ECFP chromophore (Hyun Bae et al. 2003 Demachy et al. 2005), both of which are participating in energy transfer to YFP-Venus. Compartment 1 represents a population of ECFP that does not transfer energy. Although it is known that ECFP normally decays in a bi-exponential fashion, due to two slightly different conformations, here - it is modeled as a mono-exponential decay because of the small amplitude and the spectrum is assumed to be the same as the spectra of compartments 2 and 3. However, for a better description of the data it should be different

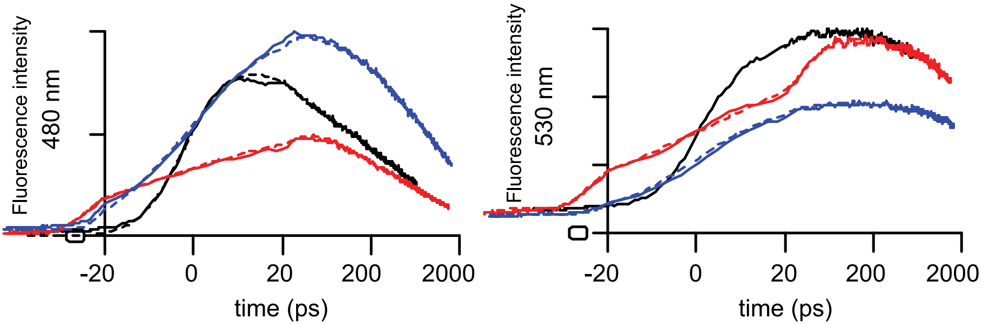

Figure 4. Decay traces and fits at 480 nm and 530 nm of streak data of YC3.60. Dashed lines represent fits of the measured traces (solid lines). Black and red lines represent traces of the Ca^{2+}-bound conformation of YC3.60, using tr2 and tr4, respectively. Blue lines represent the experiment with the Ca^{2+}-free conformation using tr4. Note that the time axis is linear up to 20 ps and logarithmic thereafter.

from the spectra of compartments 2 and 3 below 470 nm. Compartment 6 corresponds to the fluorescence from YFP-Venus. It receives 10% of its excitations via direct excitation at 400 nm, whereas the remaining 90% stems from energy transfer from compartments 2 to 5.

Representative traces and fits are depicted in figure 4. At 480 nm the emission is mostly due to fluorescence from ECFP molecules. It is visible that fluorescence at this wavelength has a smaller amplitude and a faster lifetime in the experiments with the calcium-bound conformation of YC3.60. At 530 nm the fluorescence is detected mainly from YFP-Venus molecules. There is a clear rise of fluorescence in both cases. Moreover, the intensity of the fluorescence at this wavelength is lower in the calcium-free YC3.60.

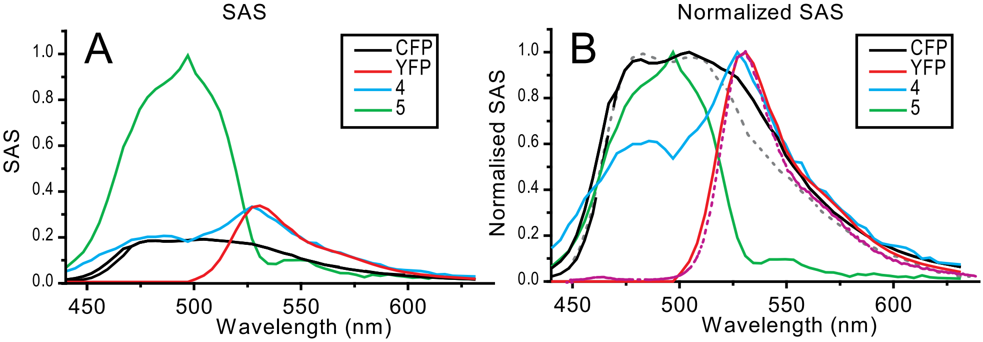

Figure 5. Species associated spectra (SAS) (A) and normalized SAS (B), estimated from the global target analysis of YC3.60 .

Figure 5 depicts the species associated spectra (SAS) estimated from the global target analysis. The black solid line in figure 5 represents the estimated spectra of the two interacting populations of ECFP (compartments 2 and 3 in kinetic scheme of figure 3). The black dashed line represents the estimated spectrum of non-interacting ECFP (compartment 1, figure 3). Note that the spectra of compartments 1, 2, and 3 are the same above 470 nm, therefore dasshed line is only visible before 470 nm. The gray dotted line (only represented in figure 5B) represents a steady-state spectrum of ECFP. The red lines in figure 5 represent the spectrum of YFP-Venus (solid), estimated from the time-resolved data and the steady-state spectrum of EYFP-Venus (magenta dotted line in figure5B). Cyan and green lines represent the estimated spectra of compartments 4 and 5 (figure 3), which are necessary to obtain a satisfactory description of the data. Although there is a bit of misfit of the spectral shape of the ECFP compartments (the steady-state spectrum of ECFP (figure 5B, dotted gray line) has lower amplitude above 520 nm), the estimated shape is considered to be satisfactory. The estimated SAS of YFP-Venus shows good agreement with the measured steady-state spectrum.

The estimated lifetimes of the excited states of the compartments and their starting concentrations, reflecting the amount of direct excitation of the compartment, are summa-

Table 1. *Estimated rate constants, lifetimes and starting concentrations of excited states of the compartments.*

Compartment #	Calcium free YC3.60			Calcium bound YC3.60			
	rate const. (ns^{-1})	life-time (ns)	start. conc.	rate const. (ns^{-1})	life-time (ns)	starting concentration tr2	starting concentration tr4
1 (non-transferring ECFP)	0.4	2.5	0.35	0.4	2.5	0.1	0.17
2 (fast-transferring ECFP)	-	-	-	67	0.015	0.43	0.48
3 (slowly-transferring ECFP)	0.31	1.41	0.47	4.0	0.024	0.0005	0.15
4	-	-	-	7.0	0.137	0.28	0.05
5	2.64	0.33	0.08	0.66	0.94	0.09	0.05
6 (YFP-Venus)	0.37	2.71	0.1	0.37	2.71	0.1	0.1

The observed lifetimes of the excited states in compartments 2-5 are calculated by adding k_i *and the additional slow decay to the ground state (*k_l*). Note that compartments 2 and 4 in calcium free YC3.60 are not present.*

The large differences in kinetics observed previously between Ca^{2+}-free and Ca^{2+}-bound YC3.60 can now be quantified (Borst et al., 2008). First the non-transferring ECFP fraction of excited states decreases from 35% to 10 or 17% for calcium-bound YC3.60. For the calcium-bound conformation of YC3.60 very fast transfer with a transfer rate of about (67 ns^{-1}) is dominating the kinetics (figure 2B and figure 5, black spectra). Starting concentrations of this ultrafast transfer compartment are very similar, 43% and 48% for the tr2 and tr4 experiments. However, the lifetime of this component is comparable to the FWHM of the IRF in the tr2 experiment (19 ps) and much less than the FWHM of the IRF in tr4 (70 ps). Therefore, the precision of estimating this rate constant is about 5 ps^{-1}. A second slower pathway for energy transfer from ECFP to YFP-Venus molecules is also present (compartment 3 or 4) with the transfer rate being 4 or 7 ns^{-1}, but the amplitude of this component is different for the tr2 and tr4 data sets. Finally, compartment 5 decays with a time constatnt of 0.94 ns, indicating very slow energy transfer. It receives less than 10% of the excitations, and it has a large ECFP-like SAS (figure 5, green). The spectral shapes of compartment 4 is not so well resolved, the cyan SAS (figure 5) appears to be a mixture of ECFP and Venus, and is interpreted as a mixture of energy transfer with rate 7 ns^{-1} , as well as some decay of Venus on this time scale. The transfer rate in the Ca^{2+}-bound YC3.60 was also determined before using single-photon timing experiments (Borst et al. 2008) and the obtained value was 18 ns^{-1} (time resolution was limited by the IRF of 40 ps), while in the present study it turned out to be possible to resolve three different transferring components to YFP-Venus with different transfer times of 15 ps 134-234 ps and 940 ps. For the calcium-free YC3.60 the main transferring component has a lifetime of 1.4 ns, which is identical to the average lifetime of transferring ECFP molecules as previously measured (Borst et al. 2008). A second transferring component with a lifetime of 330 ps and a small amplitude (8% of the excitations enter compartment 5) is also found by the target analysis. The amount of non-interacting ECFP was estimated to be about 20% for both Ca^{2+}-free and Ca^{2+}-bound YC3.60 (Borst et al. 2008). However, in the present analysis it is 35% for Ca-free YC3.60, while in the Ca^{2+}-bound conformation it is 10-17%.

It has been reported recently that YFP molecules can be photo-converted into a species, which can be excited with 400-nm light and gives fluorescence in the same region as ECFP (Valentin et al. 2005; Kirber et al. 2007). Trial studies of the fluorescence of EYFP in a buffer solution using 400 nm excitation light, show indeed the presence of fluorescence in the same wavelength region as the fluorescence of ECFP. For more accurate analysis of the YC3.60 dynamics it will be necessary to study time-resolved fluorescence spectra of YFP-Venus alone. This is most important for the analysis of the Ca^{2+}-bound YC3.60 conformation because of the fast and efficient transfer, which leads to a small fluorescence intensity of ECFP molecules. Therefore the kinetic processes that lead to fluorescence of photo-converted YFP molecules in the same wavelength region become relatively more pronounced.

3.4 Conclusions

Target analysis of time-resolved fluorescence spectra of YC3.60 shows the presence of at least two pathways for energy transfer from ECFP to YFP-Venus in both conformations of YC3.60 (in the presence and absence of calcium). In calcium-bound YC3.60 the major transfer component has a lifetime of 15 ps while for calcium-free YC3.60 it is far longer, namely 1.4 ns. The second transfer component of about 170 – 230 ps in the presence of calcium and 330 ps in the absence of calcium should probably be considered to correspond to the kinetics of photo-converted YFP-Venus chromophores. A fraction of non-interacting ECFP molecules is always present and this population is larger in calcium-free YC3.60. It is this mere non-interacting fraction of ECFP molecules that is measured in ratio imaging of YC3.60 in living cellular compartments with relatively high calcium concentration (Nagai et al., 2004).

References

Agronskaia, A. V., L. Tertoolen and H. C. Gerritsen (2004). Fast fluorescence lifetime imaging of calcium in living cells. *J. Biomed. Opt*. **9**(6): 1230-1237.

Baird, G. S., D. A. Zacharias and R. Y. Tsien (1999). Circular permutation and receptor insertion within green fluorescent proteins. *Proc. Natl. Acad. Sci. USA* **96**(20): 11241-11246.

Borst, J. W., S. P. Laptenok, A. H. Westphal, R. Kuhnemuth, H. Hornen, N. V. Visser, S. Kalinin, J. Aker, A. van Hoek, C. A. M. Seidel and A. J. W. G. Visser (2008). Structural changes of yellow cameleon domains observed by quantitative FRET analysis and polarized fluorescence correlation spectroscopy. *Biophys. J.* **95**(11): 5399-5411.

Förster, T. (1949). Experimentelle und theoretische Untersuchung des zwischenmolekularen Ubergangs von Elektronenanregungsenergie. *Zeitschrift für Naturforschung* **4a**(5): 321-327.

Gabriel, B. and J. Teissié (1998). Fluorescence imaging in the millisecond time range of membrane electropermeabilisation of single cells using a rapid ultra-low-light intensifying detection system. *Eur. Biophys J.* **27**(3): 291-298.

Guerrero, G. and E. Y. Isacoff (2001). Genetically encoded optical sensors of neuronal activity and cellular function. *Cur. Opin. Neurobiol.* **11**(5): 601-607.

Holzwarth, A. R. (1996). Data analysis of time-resolved measurements. Biophysical Techniques in Photosynthesis. Springer Netherlands: 75-92.

Hyun Bae, J., M. Rubini, G. Jung, G. Wiegand, M. H. J. Seifert, M. K. Azim, J.-S. Kim, A. Zumbusch, T. A. Holak, L. Moroder, R. Huber and N. Budisa (2003). Expansion of the genetic code enables design of a novel "Gold" class of green fluorescent proteins. *J. Mol. Biol.* **328**(5): 1071-1081.

Jares-Erijman, E. A. and T. M. Jovin (2006). Imaging molecular interactions in living cells by FRET microscopy. *Cur. Opin. Chem. Biol.* **10**(5): 409-416.

Kirber, M. T., K. Chen and J. F. Keaney (2007). YFP photoconversion revisited: confirmation of the CFP-like species. *Nat. Meth.* **4**(10): 767-768.

Miyawaki, A., O. Griesbeck, R. Heim and R. Y. Tsien (1999). Dynamic and quantitative Ca^{2+} measurements using improved cameleons. *Proc. Natl. Acad. Sci. USA* **96**(5): 2135-2140.

Miyawaki, A., J. Llopis, R. Heim, J. M. McCaffery, J. A. Adams, M. Ikura and R. Y. Tsien (1997). Fluorescent indicators for Ca^{2+} based on green fluorescent proteins and calmodulin. *Nature* **388**(6645): 882-887.

Mullen, K. M., M. Vengris and I. H. Stokkum (2007). Algorithms for separable nonlinear least squares with application to modelling time-resolved spectra. *J. Global Optimization* **38**(2): 201-213.

Nagai, T., S. Yamada, T. Tominaga, M. Ichikawa and A. Miyawaki (2004). Expanded dynamic range of fluorescent indicators for Ca^{2+} by circularly permuted yellow fluorescent proteins. *Proc. Natl. Acad. Sci. USA* **101**(29): 10554-10559.

Smith, D. and K. Johnson (1988). Single-step purification of polypeptides expressed in *Escherichia coli* as fusions with glutathione S-transferase. *Gene* **67**(1): 31-40.

Stryer, L. (1978). Fluorescence energy transfer as a spectroscopic ruler. *Annu. Rev. Biochem.*

47(1): 819-846.

Tsien, R. Y. (1998). The green fluorescent protein. *Annu. Rev. Biochem.* **67**(1): 509-544.

Valentin, G., C. Verheggen, T. Piolot, H. Neel, M. Coppey-Moisan and E. Bertrand (2005). Photoconversion of YFP into a CFP-like species during acceptor photobleaching FRET experiments. *Nat. Meth.* **2**(11): 801.

van Oort, B., S. Murali, E. Wientjes, R. B. M. Koehorst, R. B. Spruijt, A. van Hoek, R. Croce and H. van Amerongen (2009). Ultrafast resonance energy transfer from a site-specifically attached fluorescent chromophore reveals the folding of the N-terminal domain of CP29. *Chem Phys*, **357**:113-119

van Stokkum, I. H. M. and H. E. Bal (2006). A Problem Solving Environment for interactive modelling of multiway data. *Concurrency and Computation-Practice & Experience* **18**(2): 263-269.

van Stokkum, I. H. M., D. S. Larsen and R. van Grondelle (2004). “Global and target analysis of time-resolved spectra. *Biochim. Biophys. Acta.* **1657**(2-3): 82-104.

van Stokkum, I. H. M., B. F. van Oort, F. van Mourik, B. Gobets and H. van Amerongen (2008). (Sub)-picosecond spectral evolution of fluorescence studied with a synchroscan streak-camera system and target analysis. Biophysical Techniques in Photosynthesis, . Dordrecht Springer Volume II.: 223 - 240.

Zhang, J., R. E. Campbell, A. Y. Ting and R. Y. Tsien (2002). Creating new fluorescent probes for cell biology. *Nat Rev Mol Cell Biol* **3**(12): 906-918.

Chapter 4

Fluorescence Lifetime Imaging Microscopy (FLIM) data analysis with TIMP

based on:
Laptenok, S.[*], K. M. Mullen[*], J. W. Borst, I.H.M. van Stokkum, V.V. Apanasovich, and A. J. W. G. Visser. 2007. Fluorescence lifetime imaging microscopy (FLIM) data analysis with TIMP. J. Stat. Softw. 18(8)
* contributed equally

Abstract

Fluorescence Lifetime Imaging Microscopy (FLIM) allows fluorescence lifetime images of biological objects to be collected at 250 nm spatial resolution and at (sub-)nanosecond temporal resolution. Often n_{comp} kinetic processes underlie the observed fluorescence at all locations, but the intensity of the fluorescence associated with each process varies per-location, i.e., per-pixel imaged. Then the statistical challenge is *global analysis* of the image: use of the fluorescence decay in time at all locations to estimate the n_{comp} lifetimes associated with the kinetic processes, as well as the amplitude of each kinetic process at each location. Given that typical FLIM images represent on the order of 10^3 timepoints and 10^3 locations, meeting this challenge is computationally intensive. Here the utility of the **TIMP** package for **R** to solve parameter estimation problems arising in FLIM image analysis is demonstrated. Case studies on simulated and real data evidence the applicability of the partitioned variable projection algorithm implemented in **TIMP** to the problem domain, and showcase options included in the package for the visual validation of models for FLIM data.

4.1. Introduction

This chapter describes the utility of the TIMP package for the R language and environment for statistical computing (R Development Core Team 2008) for the analysis of images collected by Fluorescence Lifetime Imaging Microscopy (FLIM) experiments. FLIM experiments allow the collection of fluorescence lifetime images of biological objects at ~250 nm lateral resolution and at (sub-) nanosecond temporal resolution. FLIM has been widely applied in cell biology to detect interactions between fluorescently labeled biological molecules such as proteins, lipids, DNA and RNA. One experimental technique, which is sensitive at these small length scales of 1-10 nm, is the detection of Förster Resonance Energy Transfer (FRET). FRET is a bimolecular process in which the excited-state energy of a donor fluorophore is non-radiatively transferred to a ground-state acceptor molecule by dipole-dipole coupling. The FRET efficiency varies with the inverse 6th power of the distance between donor and acceptor and is usually negligible when the distance is larger than 10~nm. FRET is a fluorescence quenching process and can be identified by a shorter fluorescence lifetime of the donor. Intracellular proteins of interest can be genetically tagged with variants of the green fluorescent protein (GFP) (Tsien 1998). Spectral variants cyan fluorescent protein (CFP, donor) and yellow fluorescent protein (YFP, acceptor) have been proven a valuable FRET-pair. FRET as measured by FLIM can therefore be used as a “spectroscopic ruler” to map protein-protein interactions inside cells (for recent applications see Barber et al. 2005 and Grailhe et al. 2006). Suhling et al. 2005 have comprehensively reviewed different FLIM methods, FLIM and FRET examples and other FLIM applications.

Well-designed data analysis techniques are required to process the measured lifetime images to unravel photophysical phenomena in complex molecular and cellular systems. It is often the case that the dynamics of the system are well-described by a model in which a small number of exponential decays with equal decay rates across all pixels underly the measured fluorescence, with amplitude parameters for the exponentials varying per-pixel. Then estimates for the amplitude parameters are conditionally linear on estimates for the decay rate parameters, allowing application of the variable projection algorithm (Golub and LeVeque 1979), which has been shown to have many desirable properties (Golub and Pereyra 2003, Mullen et al. 2007) for problems of this form. A disadvantage of the variable projection method that has prevented its application in this problem domain (Verveer et al. 2000) is that large memory resources are required. The TIMP package contains an implementation of a partitioned variable projection algorithm that returns the same results as the standard variable projection algorithm but requires much less memory (Mullen and van Stokkum 2007). The ability to apply the variable projection functional to estimation problems in the absence of large memory resources is a primary advantage of the application of TIMP in the FLIM image analysis problem domain. A further primary advantage is the support the package provides for visual interpretation and validation of the results of model fit.

4.2. Statistical model for FLIM data

FLIM images represent the decay of fluorescence in time at many different locations in the underlying system. Each location is represented by a pixel *x*, so that the image may be represented as a matrix

$$\Psi = \left[\begin{array}{c|cccc} & x_1 & x_2 & \cdots & x_n \\ \hline t_1 & \psi(t_1, x_1) & \psi(t_1, x_2) & \cdots & \psi(t_1, x_n) \\ t_2 & \psi(t_2, x_1) & \psi(t_2, x_2) & \cdots & \psi(t_2, x_n) \\ \vdots & \vdots & \vdots & \ddots & \vdots \\ t_m & \psi(t_m, x_1) & \psi(t_m, x_2) & \cdots & \psi(t_m, x_n) \end{array}\right] \qquad (1)$$

Each column of $\mathbf{\Psi}$ represents a fluorescence decay in time at a given pixel x. The decay of fluorescence data in time $\psi(t)$ can often be satisfactorily modeled as a sum of n_{comp} first-order kinetic processes convolved with an instrument response function (IRF) $g(t)$, so that

$$\psi(t) = \sum_{i=1}^{n_{comp}} c_i a_i = \sum_{l=1}^{n_{comp}} \exp(-t / \tau_i) \otimes g(t) a_i \qquad (2)$$

where c_i represents the contribution to the data from process *i* in time *t*, a_i represents the amplitude of decay *i*, and $\otimes$ is the convolution operator. The model parameters to be fit are then the lifetimes τ_i and their associated linear coefficients a_i representative of intensity.

When the same kinetic processes underly the fluorescence at all n locations, Eq. 2 can be applied globally to the image $\mathbf{\Psi}$, so that

$$\mathbf{\Psi} = \mathbf{CE}^T = \sum_{i=1}^{n_{comp}} c_i a_i^T = \sum_{l=1}^{n_{comp}} (\exp(-t / \tau_i) \otimes g(t)) a_i^T \qquad (3)$$

where **C** is a matrix in which column *i* represents the time-profile of the *ith* kinetic process, and **E** is a matrix in which column *i* represents the intensity of kinetic process *i* across pixels. Then the parameter estimation task is *global analysis*: estimation of the n_{comp} lifetimes τ associated with the image as a whole and the n_{comp} amplitude parameters a_i associated with each pixel (so that $n*n_{comp}$ amplitude parameters are estimated in total). Under least-squares criteria this is

$$\min \left\| \mathbf{C}(\tau)\mathbf{E}^T - \mathbf{\Psi} \right\|_{F^2} \tag{4}$$

This is an instance of the multi-exponential analysis problem, which is common in physics applications. Its difficulty is well-known, as Istratov et al. review. (Istratov and Vyvenko 1990)

$\mathbf{\Psi}$ represents the number of photons fluorescing from the location represented by pixel *x* at time *t*, and is therefore count data, the noise associated with which is assumed to be Poisson distributed.

4.3. Methods for FLIM data collection and analysis

FLIM data is collected by exciting a sample (such as a cell) to fluoresce (i.e., emit photons) using a laser pulses. After a laser pulse the time *t* until the first arrived photon is detected at pixel *x* is measured; The process of applying a laser pulse and recording the time of arrival of the first photon is repeated many times. The resulting histograms of arrival times represent fluorescence decays per pixel *x*.

Since samples of interest are *in vivo*, the power of the laser light used must be low if the sample is to remain alive throughout the measurement. The use of laser light of low power results in the arrival of few photons at location *x*. The requirement to keep the sample alive and in the same condition also means that the acquisition time cannot be long, (i.e., the sample cannot be subjected to too many laser pulses).

To improve signal-to-noise ratio (SNR), the time resolution may be decreased, since under a wider histogram channel more photons will be collected. The FLIM experiment is thus always compromising between time resolution and SNR. FLIM experiments that measure process with sub-nanosecond time resolution often have low SNRs (6-15 is typical). Further discussion of the methodology of FLIM experiments may be found in, e.g., Becker and Bergmann (2003)

Methods for the analysis of FLIM data commonly applied (Becker et al. 2001; Becker et al. 2002) fit the model given by eq. 2 independently to each of the *n* pixels in an image. This yields estimates for the decay rates of the n_{comp} kinetic process as well as n_{comp} estimates of the amplitude of each process, *for each pixel in the image*. This is seldom desired, for the assumption that the same n_{comp} kinetic processes underly measurements at all pixels is usually valid.

Data analysis methods that acknowledge the desirability of global analysis, which assumes that the underlying kinetic processes have the same lifetimes but different amplitudes across all pixels measured, as in eq.3 often restrict themselves to the bi-exponential instance of the model (Pelet et al. 2004; Barber et al. 2005). Verveer et al. (2000) acknowledge that the global analysis associated with Problem eq. 4 is a separable nonlinear least-squares problem that may be solved using the variable projection approach, though the authors state that for the large number of variables involved in fitping typical FLIM data, the memory requirements prohibit the approach.

TIMP allows an arbitrary number of exponentials may be fit to the data, though under experimentally realistic SNRs it is most often possible to resolve only one or two components. **TIMP** applies a partitioned variable algorithm to the global analysis problem associated with the analysis of FLIM images. This algorithm forms the residual vector prescribed by the variable projection functional without the need to store and operate on prohibitively large matrices, as is described in detail in (Mullen and van Stokkum 2007).

4.4. Extension of TIMP for FLIM data analysis

Several new capabilities were added to the TIMP package to facilitate the analysis of FLIM data. As described in Section 4.4.1, a file format was defined for the input of FLIM images into TIMP. A method for numerical convolution of an exponential decay with a measured IRF was added to the kinetic model options of the package, as Section 4.4.2 elaborates. New options to visually validate the results of fitting were also added, and are discussed in Section 4.4.3.

4.4.1. Data format

Given a FLIM image, it is often desirable to select those pixels associated with the subject of interest for modeling. For example, given a FLIM image of a cell, only those pixels interior to the cell wall are typically representative of the fluorescence decay of interest, and accordingly only these pixels are usually selected for modeling. Pre-processing dedicated to pixel selection is currently performed outside of TIMP. The indices of selected pixels are then included in the ASCII input file.
The format of the input file is as follows.

line 1:	reserved for comments, not read
line 2:	reserved for comments, not read
line 3:	the character string "FLIM Image"
line 4:	dimension of image as x y (space-delimited)
line 5:	number of timepoints t in image
line 6:	number of pixels x selected for analysis
line 7:	vector of the times at which measurements were made
line 8:	index of selected pixel and decay trace from this pixel $\mathbf{\Psi}$(,p)
...	...
line (8+number of selected pixels):	the character string "Intensity map"
remaining lines:	FLIM intensity image as matrix of dimension x×y

Files in this format may be read into **R** using the **TIMP** function `readData`. Section 4.4.3 defined the meaning of the intensity image; Section 6 contains an example of the use of the `readData` function.

4.4.1. Options for numerical convolution with a measured IRF

The analysis of FLIM data typically employs a measured IRF *g(t)* in fitting the exponential decay model contained in Eq. 3. Evaluation of Eq. 3 requires the numerical convolution of *g(t)* with an exponential decay. Methods to perform this convolution have been addressed in the literature at least since the seminal paper of Grinvald and Steinberg (Grinvald and Steinberg 1974), as Bajzer and co-workers discuss (Bajzer et al. 1995). For FLIM data (in which *g(t)* and the exponential decay are very often represented by 1024 or less time points), we have found that methods based on a Fourier transformation are problematic, and that iterative methods give better results. Since an iterative method for the convolution of a vector and an exponential decay was not found by the authors implemented in **R** or in openly available scientific programming libraries, a method based on an iterative technique suggested in (Grinvald and Steinber.Iz 1974) was implemented in the shared `C` library used by **TIMP**, as the function `Conv1`.

To validate that the implementation of this iterative convolution technique returns an un-biased result, we considered its operation on the convolution of an IRF *g(t)* simulated as a Gaussian with location μ and full width half maximum Δ parameters inspired by values occurring in FLIM experiments. The convolution of a Gaussian with an exponential decay is determined by the analytical expression

$$e^{-tk_j} \otimes \frac{1}{\sigma\sqrt{2\pi}} e^{-\frac{(t-\mu)^2}{\sigma^2}} = \frac{1}{2} e^{\frac{1}{\tau}\left(\mu + \frac{k_j\sigma^2}{2}\right)} e^{-tk_j} \left\{ 1 + erf\left(\frac{t-(\mu + k_j\sigma^2)}{\sqrt{2}\sigma} \right) \right\} \qquad (5)$$

where $\sigma = \Delta/(2\sqrt{2\log(2)})$ and *erf* is the error function. Note that Eq. 5 uses the decay rate k_j (which is also the parameter estimated), whereas its reciprocal $\tau_j = 1/k_j$ is commonly reported. For times and decay rates k_j inspired by values in measured data of interest, the results determined by the implementation of the iterative technique are unbiased as compared to results obtained using the analytical expression.

4.4.3. Model validation

Model validation in the FLIM image analysis application domain is ideally largely visual. The magnitude of residuals and fitted parameter estimated are possible to map per-pixel onto the modeled image as colors, allowing the results of fitting to be quickly evaluated. Several options for this display are implemented in **TIMP**. The analysis of a FLIM image with the **TIMP** function `fitModel` results in a multipanel summary plot as shown in figure 1, whose components will be explained in turn.

First histograms of the estimated amplitudes associated with each component, with the corresponding global lifetime estimate on the bottom are displayed. In figure 1 these are the two plots contained in row 1, columns 1 and 2. These plots allow for an impression of the

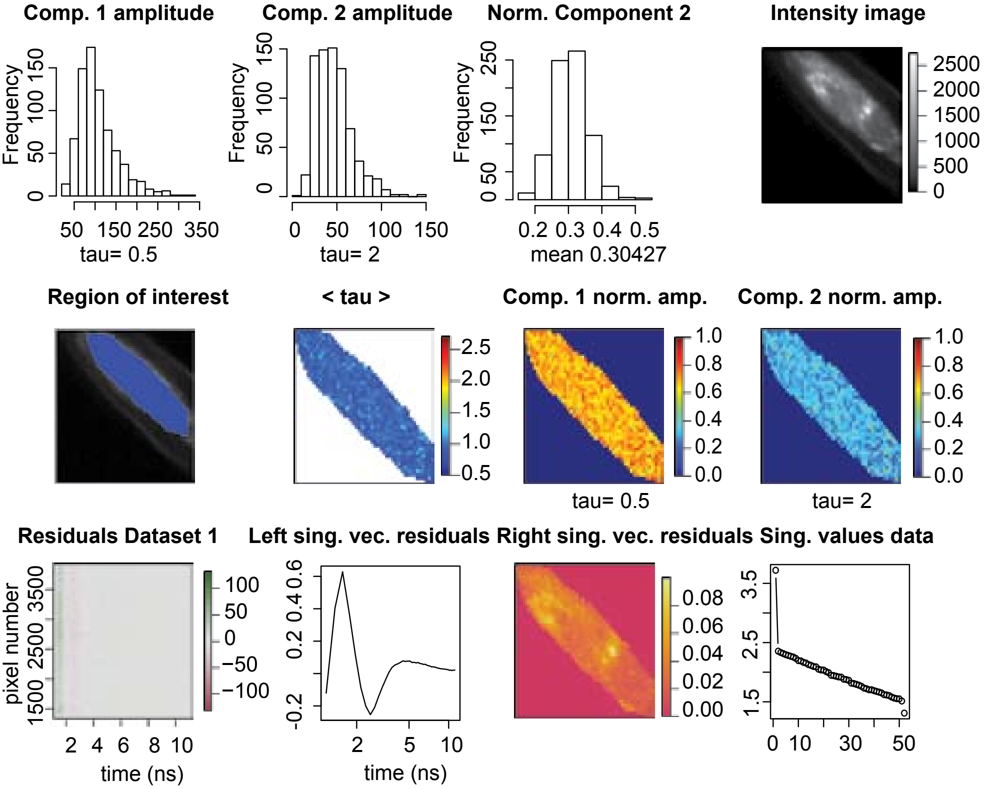

Figure 1. *An example multipanel summary plot of residuals and fit of a bi-exponential model for measured FLIM data. Individual plots are explained in the text of Section 4.3 The image is taken from a fixed BHK (baby hamster kidney) cell with CFP expressed.*

absolute contributions of the components across all pixels of the image. The following plots in the summary figure are $n_{comp}-1$ histograms of the relative contribution p_j of component j, where

$$p_j = \frac{a_j}{\sum_i^{n_{comp}} a_i} \tag{6}$$

In figure 1 this is the plot contained in row 1, column 3. These plots allow for an impression of the relative contribution of the component j across all pixels of the image.

A plot of the intensity image is then given. This intensity image includes those pixels not selected for modeling, and represents the number of photons per pixel measured over the course of all times t represented by the dataset. From this intensity image only some pixels are typically selected for modeling. The selected pixels are shown in the next plot in blue. The intensity image and the intensity image with selected pixels in blue are contained in row 1, column 4 and row 2, column 1, respectively, in figure 1.

The plot titled "<τ>" presents the average lifetime for each pixel from the selected region, where the average lifetime is given as

$$<\tau>=\frac{\sum_{i}^{n_{comp}}\tau_i a_i}{\sum_{i}^{n_{comp}} a_i} \tag{7}$$

(row 2, column 2 of figure 1). The average lifetime may allow insight into the rate of energy transfer in processes on a per-pixel basis. The next n_{comp} plots show normalized amplitudes in a color code mapped to the associated image, for each component j. In figure 1 these are the plots contained in row 2, columns 3 and 4. The normalized amplitude plots allow insight into spatial patterns in the contribution of components. For example, these plots may allow identification of specific structures in a cell where the contribution of a given component is large.

Next the residuals associated with each pixel from the selected region are given as a color image, providing information on the quality of the fit both spatially and temporally, (row 3,column 1 of figure 1). The first left singular vector of the residuals as results from a singular value decomposition (SVD) is plotted next (row 3, column 2 of figure 1). This plot allows insight into structure in the residuals in time. For typical FLIM experiments, this structure is large around time 0, where the exponentially decaying components and the IRF contribute most. Structure in the left singular vectors after time 0 may be indicative of an inadequacy in the applied model.

The next plot shows the first right singular vector associated with the SVD of the residuals mapped to the pixels selected for analysis, which provides information on the quality of the fit per pixel, and allows determination of whether the lack of fit is spatially structured. The last plot shows the singular values associated with the SVD of the data. The number of singular values that stand out in this plot indicate how many spatially and temporally independent components are present in the data. Further discussion of the use of the rank of the data in the estimation of the number of components can be found in e.g., Henry (1997).

4.5. A simulation study

A study of the application of **TIMP** to the analysis of simulated FLIM images was made in order to investigate the capabilities of the package in the problem domain. The study was designed in two parts.

The first part, described in Section 4.5.1, examines the ability of the software to estimate the lifetimes associated with bi-exponential decays in which the decay of fluorescence in time was measured over 64 and 256 timepoints (which we refer to as *channels* throughout). 64 and 256 channel data is commonly collected in FLIM experiments, and thus was of particular interest. Simulation of bi-exponential decays was performed because Gratton et al. (2003) have shown that resolution of more than two components is not possible over this number of channels for experimentally realistic lifetime values and signal-to-noise ratios.

The second part of the simulation study, described in Section 4.5.2, smoothly varies the two amplitude parameters associated with bi-exponential decays across columns of the image for the purpose of examining whether the software is able to accurately estimate the relative contribution of the components.

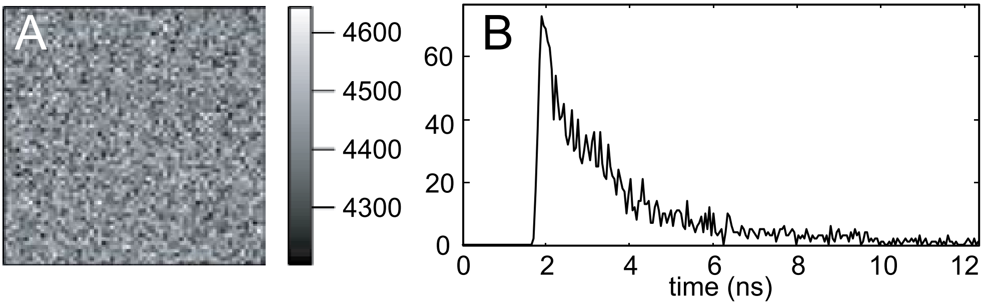

Figure 2. *(A) Intensity image of simulated data comprised of 1600 pixels in a 40×40 pixel arrangement, where intensity means the total photons summed over all channels. (B) A fluorescence decay trace over 256 channels in the interval 0-12.5 ns is ssociated with each of the 1600 pixels comprising an image.*

Images $\psi(t,x)$ were simulated using eq. 2, as shown in figure 2. Each pixel is associated with a decay in the time window 12.5 ns, over either 64 channels or 256 channels (equidistant in the interval 0-12.5 ns). The IRF $g(t)$ was simulated as a Gaussian with mean 9 and 34 and standard deviation 0.4 and 1 for the 64 channel and 256 channel cases, respectively, in units of channels. Note that non-zero contribution of the IRF in both the 64 channel and the 256 channel case is represented by very few channels (3-8), as is commonly the case in FLIM experiments. Poisson noise was added to each decay trace $\psi_x(t)$ to obtain data of the desired signal-to-noise ratio (SNR) (using the **R** function `rpois`).The result may be considered as count data where $\psi(t,x)$ represents the number of photons collected at a given pixel x and time t, as in measured time-correlated single photon counting data (Maus et al. 2001). The SNRs of simulated images were chosen to reflect those commonly obtained in FLIM experiments.

4.5.1 A simulation study in the resolution of bi-exponential decays

This part of the simulation study examines the ability of TIMP to recover satisfactory estimates for the lifetimes underlying simulated images representative of two components. Images simulated with three pairs of lifetimes (in nanoseconds) collated in table 1 were studied. For each pair of lifetimes studied, the relative contribution of the two components was varied between 0.1 and 0.9, so that 9 different images were simulated using each pair of lifetime values. The lifetime values are experimentally motivated (Borst et al. 2005). The images were simulated for both the SNR 8 and the SNR 15 case; the SNR 8 case is average for typical FLIM experiments, while the SNR 15 is higher than average.

A bi-exponential model was fit to the images, with the relative contribution of the two components being estimated as conditionally linear on values for the nonlinear lifetime estimates. The results are shown for images simulated with the pairs of lifetimes on row 1 and 2 of table 1 in figure. 3. Note that each boxplot describes the variance in lifetime estimates as the relative amplitude of the components is varied. Our criteria for a satisfactory lifetime estimate is that the estimate is ±*5%* of the lifetime value used in simulation for data containing

Table 1. *Parameter values in nanoseconds used in simulation of bi-exponential images. Instances of each group were simulated with contributions from the component with the longer lifetime τ_2 as 10%, 20%, 30%, 40%, 50%, 60%, 70%, 80% and 90% of the total intensity.*

Group	τ_1	τ_2
1	1.14	3.72
2	0.6	2.5
3	0.2	0.5

256 channels, and within ±*10%* of the lifetime value used in simulation for data containing 64 channels. Under this criteria, the lifetime estimates obtained and shown graphically in figure 3 are satisfactory. The small bias is attributed to using the number of photons at the leftmost point of each bin of times comprising a time-channel as representative of the average lifetime within the bin; because the data is exponentially decaying, there are always more photons to the left of the bin than to the right, and the average lifetime is thereby underestimated. The bias disappears when the number of channels is increased (for example, for data containing 1024 channels and the same SNR and lifetime values, it is insignificant). For the third pair of lifetimes studied, with $\tau_1=0.2$ *ns* and $\tau_2=0.5$ *ns*, it is impossible to determine satisfactory estimates even for data with SNR 15. The very short lifetimes are represented by only a few channels, so that there is not sufficient information.

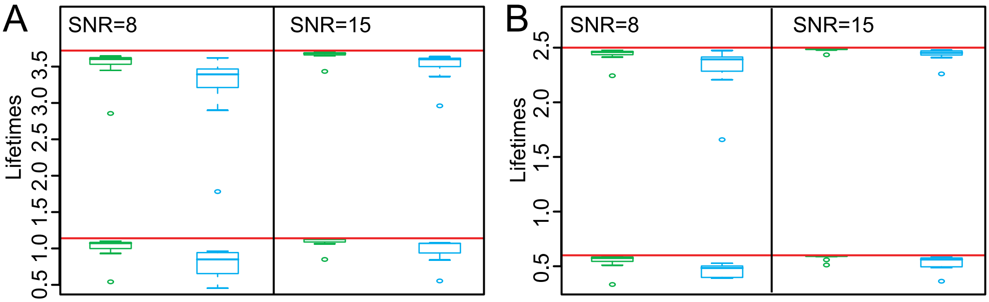

Figure 3*. Boxplots of lifetime estimates for each of two components given datasets simulated with lifetimes described in the first two rows of table 1. Each boxplot is comprised of lifetime estimates determined from fitting 9 different images, simulated with different relative amplitudes between the lifetimes. Lifetimes used in simulation are marked as red lines. Green represents results obtained on images in which the decay was represented by 256 channels, whereas blue represents results obtained on images in which the decay was represented by 64 channels. (A) shows results on images simulated with the lifetimes given in row 1 of Table 2 and (B) shows results on images simulated with the lifetimes given in row 2 of table 1.*

We found that for the lifetime values examined, for cases in which the contribution of one component was lower than 20% and the SNR was 8, lifetime estimates were not satisfactorily estimable. For SNR 15, lifetimes were not satisfactorily estimable for cases in which the contribution of one component was less than 10%.

This part of the simulation study was also repeated using an IRF measured on a FLIM set-up (as opposed to using a simulated IRF with a Gaussian distribution) to check that noise present in the IRF does not significantly decrease the accuracy of lifetime and amplitude estimates. The obtained lifetime and amplitude estimates were very similar to those reported for the Gaussian IRF case, validating that the parameter estimation methodology is robust to an experimentally realistic amount of noise in the IRF.

We consider this part of the simulation study to demonstrate some limits of the resolvability of bi-exponential lifetimes on images inspired by measured data, and that for cases of practical interest **TIMP** lifetime estimates returned by **TIMP** are satisfactory.

4.5.2 A simulation study in the estimation of relative amplitudes of bi-exponential decays

A simulation study was made on instances of the image shown in Figure 4. The decay curve associated with each pixel is bi-exponential, with the two components having lifetimes of 0.6 and 2.5 ns respectively. The amplitude of the contribution a_1 from the first component varies from 0 to 1 across each column of the image, while the contribution a_2 from the second component varies from 1 to 0. Fitting a bi-exponential model to such images allows examination of whether the software is able to accurately estimate the two amplitude parameters a_1 and a_2 associated with each pixel. This part of the simulation study is inspired by a similar study by Pelet et al. (2004). The size of each analyzed image was 64x64 pixels (4096 pixels). The decay of the intensity at each pixel was represented by 256 timepoints equidistant in the interval 0-12.5 ns (this is the 48 ps/channel case described in Section 4.5.1. Images were simulated with both SNR 8 and SNR 25.

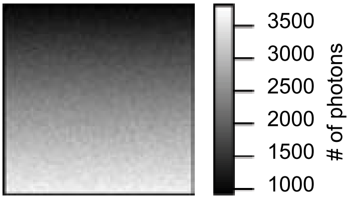

__Figure 4.__ A 64x64 pixel simulated image at one timepoint, in which the relative contribution of the first component increases linearly from 0 to 1 and the contribution of the second component decreases linearly from 1 to 0 along each column of the image. Each simulated dataset is comprised of 256 such images, representing the 256 timepoints (channels) simulated.

Table 2 shows that the lifetime estimates well-approximate the values used in simulation of the images in both the SNR 25 and the SNR 8 case. The deviations from the values of the amplitudes a_i used in simulation are small and unbiased, as shown in Figure 6C

__Table 2.__ Lifetime values in nanoseconds used in simulation and estimated lifetimes for simulated images with smoothly varying contributions from two components.

	Value used in simulation	SNR 25	SNR 8
τ_1	0.6	0.57	0.58
τ_2	2.5	2.49	2.38

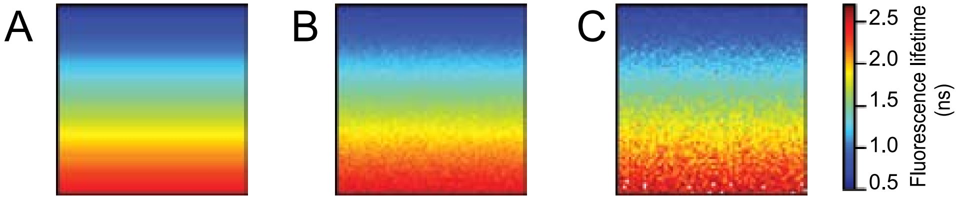

Figure 5. *Colors above represent the average lifetime determined with eq.7 (A) Simulated image with $\tau_1 = 0.6$ ns, $\tau_2 = 2.5$ ns and a linearly varying contribution from two components over time. (B) Estimates of the average lifetime determined with Eq. 7 for an instance of the image in (A) with SNR = 25. Estimated lifetimes are $\tau_1 = 0.57$ ns, $\tau_2 = 2.49$ ns. (C) Estimates of the average lifetime determined with eq. 7 for an instance of the image in (A) with SNR = 8. Estimated lifetimes are $\tau_1 = 0.58$ ns, $\tau_2 = 2.38$ ns.*

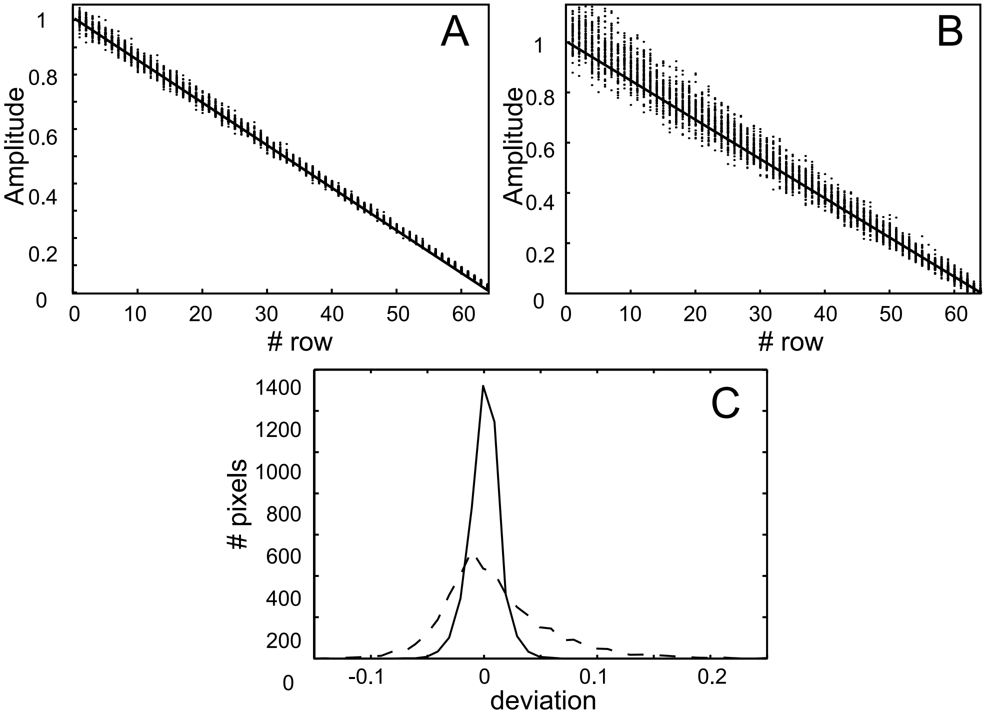

Figure 6. *A 64x64 image was simulated in which the relative contribution of two exponentially decaying components was made to vary linearly along each column as shown in Figure 5 (A).* **TIMP** *was then used to fit a model for the simulated data, resulting in 64 estimated relative amplitudes that correspond to rows of figure 5 (A) for each of the 64 distinct relative amplitude values used in simulation, under data having both SNR 25 and SNR 8. (A) and (B) show the relative amplitude values used in simulating the data as a line; dots represent the distribution over 64 estimates, i.e., rows in the images in figure 5 (B) and (C). In (C) histograms of deviations from the values used in simulation for (solid line) SNR = 25 (dashed line) SNR = 8 estimates are shown. These deviations are unbiased and small.*

graphically. Furthermore the lifetime estimates collated in table 2 are also satisfactory. We conclude that this part of the simulation study demonstrates the ability of **TIMP** to return satisfactory estimates of the amplitude parameters a_i determining the relative contribution of components.

4.6. Case study on measured CFP data

We were interested in investigating the capabilities of **TIMP** for FLIM image analysis of measured data. In cell biology studies FRET-FLIM is often used to demonstrate molecular interactions *in vivo*. For this purpose the fluorescent proteins cyan fluorescent protein (CFP) and yellow fluorescent protein (YFP) are the most widely used as donor-acceptor FRET pairs (Grailhe et al. 2006). However, the fluorescent decay of CFP is bi-exponential, making quantitative analysis of an interacting FRET population challenging (Russinova et al. 2004; Peter et al. 2005).

Time-correlated single photon counting experiments with a very high SNR (unattainable in FLIM experiments) described in (Borst et al. 2005) established the lifetimes of CFP in a solution. We performed an experiment to collect FLIM images of the same sample in a micro-capillary, using the experimental set-up described in (Borst et al. 2003). Note that FLIM images of proteins in solution are not usually measured (the study of protein conformational dynamics *in situ* being the goal of most FLIM experiments), but that this experiment offers an opportunity to validate the ability of the software to estimate the lifetimes associated with the fluorescence decay of this important donor.

The SNR of the FLIM experiment was approximately 9. The time resolution was 48 ps/channel (over 256 channels). The fluorescence intensity image and region selected for analysis are shown in figure 7.

To convey how the package is used to analyze a FLIM image, we describe all commands used to perform this part of the study.

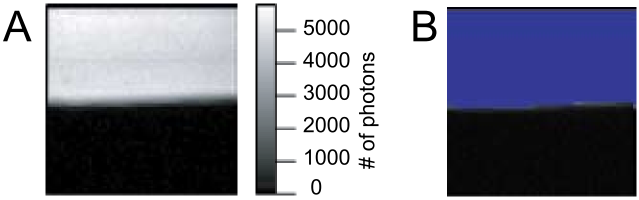

Figure 7. *(A) Intensity image of a measured image of CFP in solution, where color represents the number of photons detected in a given pixel (B) Intensity image with pixels selected for analysis in blue.*

4.6.1 Reading FLIM data into TIMP and preprocessing

The package is loaded.

```
R> library(“TIMP”)
```

Data is read into **R** using the `readData` function of **TIMP**

```
R> cfp_data <- readData(“cfp-13um-256ch-1000s_all.txt”)
```

Preprocessing is then performed to select certain times for analysis using the **TIMP** function `preProcess`.

```
cfp_data_sel <- preProcess(cfp_data, sel_time=c(33,230))
```

A measured IRF is then read in and the same time points as selected in the data are chosen.

```
R> mea_IRF <- scan(“xtetoh_256_060822-bg_int.txt”)[33:230]
```

4.6.2 Initial model for CFP in solution: Mono-exponential decay

The first model applied is based on a mono-exponential decay. The starting value for the decay rate given as 0.3, and is constrained positivity. The model is specified using the **TIMP** function `initModel`.

```
R> mono_cfp_model <- initModel(mod_type = “kin”,
+ kinpar=c(0.3), convalg = 1, parmu = list(0.01),
+ measured_irf = mea_IRF, fixed = list(parmu=c(1)),
+ seqmod=FALSE, positivepar = c(“kinpar”),
+ title=”CFP mono-exponential decay”)
```

4.6.3 Fitting and validation of initial mono-exponential model

The TIMP function fitModel is used to fit the mono-exponential model.

```
R> mono_result <- fitModel(list(cfp_data_sel),
+ mono_cfp_model,
+ opt=list(iter=20, linrange = 20,
+ makeps =”cfp_mono”,
+ notraces = TRUE, xlabel = “time (ns)”,
+ ylabel = “pixel number”, FLIM=list()))
```

The plot of the residuals returned is shown in figure 8. The image plot of the residuals in the upper left hand corner show that there is a pattern of misfit around time 3.5 ns. This pattern of misfit is also indicated in the large upward trend of the left singular vector of the residuals shown in the lower left plot of figure 8, which peaks at 3.5 ns. The root mean square (RMS) error associated with the fit is 5.2. We conclude that a mono-exponential decay model for CFP is not sufficient.

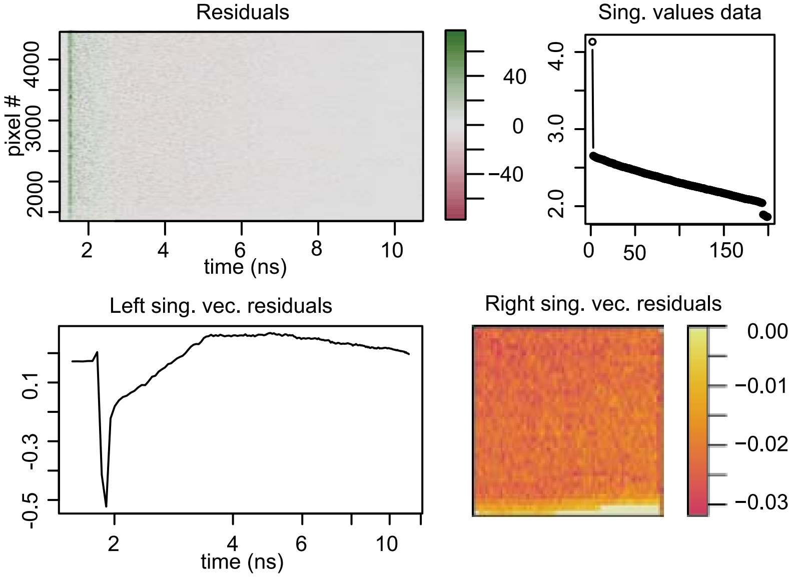

Figure 8. *An image plot of the residuals under the mono-exponential model fit shows structure in time before 3.5 ns.The first left singular vector resulting from an SVD of the residuals also shows this structure. The first right singular vector of an SVD of the residuals mapped to the associated pixels on the intensity image shows the residuals are relatively homogeneous in space. The RMS error associated with this fit is 5.2.*

4.6.4 Refined model for CFP in solution: bi-exponential decay

Based on the inadequacy of the fit of the mono-exponential model as evidenced by analysis of the residuals, the `initModel` function was used to specify a bi-exponential model for the measured CFP image.

```
R> bi_cfp_model <- initModel(mod_type = “kin”,
+ kinpar=c(1, 0.3), convalg = 1, parmu = list(0.01),
+ fixed = list(parmu=c(1)), measured_irf = mea_IRF,
+ seqmod=FALSE, positivepar=c(“kinpar”),
+ title=”CFP bi-exponential decay”)
```

4.6.5 Fitting and validation of initial bi-exponential model

```
R> bi_result <- fitModel(list(cfp_data), bi_cfp_model,
+ opt=list(iter=20, linrange = 20,
+ makeps =”cfp_bi”,
+ notraces = TRUE,
+ xlabel = “time (ns)”,
+ ylabel = “pixel number”, FLIM=list()))
```

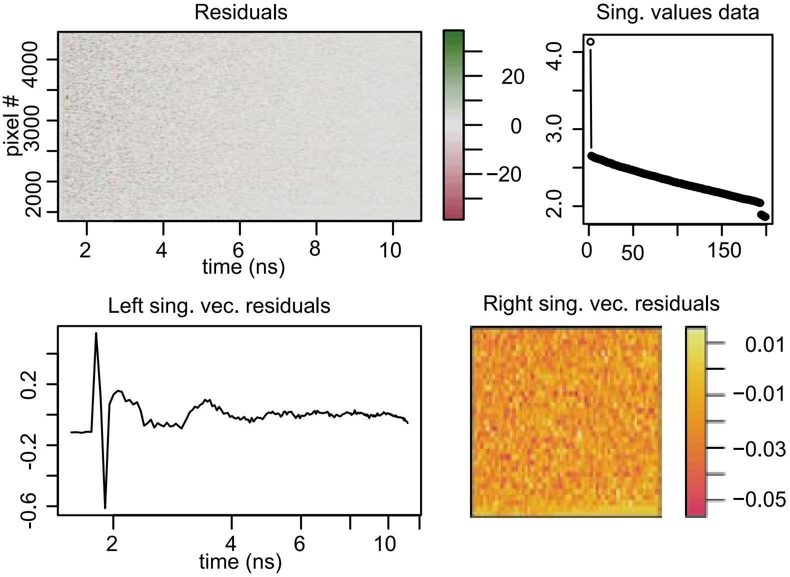

Figure 9. *An image plot of the residuals under the bi-exponential model fit shows less structure in time as compared to the same plot for the mono-exponential fit in figure 8. The first left singular vector resulting from an SVD of the residuals also shows less structure. The first right singular vector of an SVD of the residuals mapped to the associated pixels on the intensity image shows that the residuals remain homogeneous in space. The RMS error associated with this fit is 4.9, less than for the mono-exponential model fit.*

An image plot of the residuals under the bi-exponential model fit shows less structure around time 3.5 ns as compared to the same plot for the mono-exponential fit in figure 8. The first left singular vector resulting from an SVD of the residuals also shows less structure around 3.5 ns. Note that we are not concerned about the structure in the SVD around 0 ns because misfit at this time results from the large contribution of the IRF and the peak in the amplitude of components at the start of their decay at this timepoint. The first right singular vector of an SVD of the residuals mapped to the associated pixels on the intensity image shows that the residuals remain homogeneous in space. Furthermore, the RMS square error has decreased to 4.9 from the RMS error of 5.2 under the fit of the monoexponential model.

Table 3. *Parameter estimates obtained using* **TIMP** *on a measured CFP image*

	a_1	τ_1	a_2	τ_2	$<\tau>$
TIMP estimate	0.373	0.95	0.627	3.48	2.54
established value	0.335	1.14	0.665	3.72	2.86

CFP dataset analyzed with a bi-exponential model, and values in the literature for a dataset collected under similar experimental conditions analyzed using the same bi-exponential model. Note that variability in the experimental set-up, laser power and sample preparation limit the degree to which the results are directly comparable.

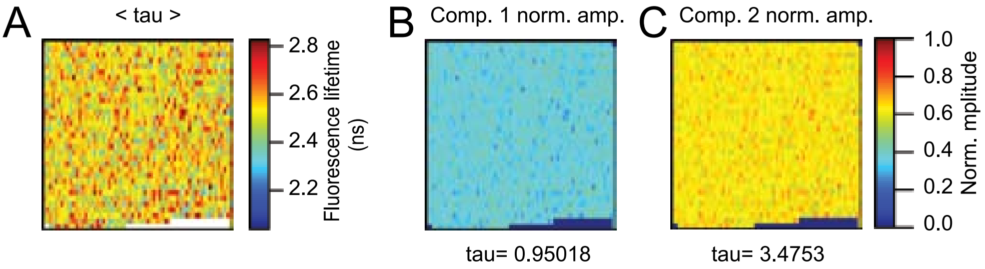

Figure 10. *(A) Distributions of the average lifetimes per location determined with Eq. 7. Normalized amplitudes for component 1 (B) and component 2 (C) as a color on the associated image.*

The lifetime estimates under the bi-exponential model agree well with values published in Borst et al. (2005) for analysis of a dataset collected under similar experimental conditions, as tabulated in table 3. Figure 10A shows that the estimate for the average lifetime per pixel over the course of the decay (as determined with eq. 7) has no spatial structure, as is expected since the measured image represents a homogenous solution. Figure 10 B and C show that the normalized amplitudes of the components are also spatially homogenous, also as expected from the homogeneity of the solution.

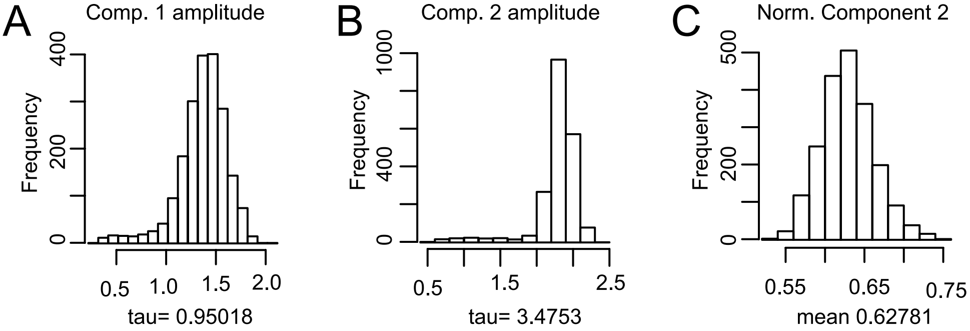

Figure 11. *Histograms of amplitudes of components (A,B) and normalized amplitude of component 2 calculated with Eq. 6 (C)*

4.7. Conclusions

A feasibility study has been made to investigate the use of the **TIMP** package of **R** for the analysis of FLIM data. In the course of the study new options for the fitting and validation of FLIM images with the package were developed. In a simulation study the package was shown to return satisfactory estimates of both lifetime and amplitude parameters, the latter of which are estimated as conditionally linear parameters. On a real dataset it was possible to resolve the contributions of two components known to exist in terms of lifetime and amplitude estimates known from the literature, which further confirms the applicability of the partitioned variable projection fitting algorithm that **TIMP** implements to modeling FLIM images.

Future work will apply **TIMP** to the analysis of further experimentally collected FLIM data. Energy transfer between components will be modeled using the compartmental modeling options for **TIMP** described in (Mullen and van Stokkum 2007). Implementation of a graphical user interface (GUI) to facilitate interactive model validation is also planned, along with a study to benchmark and optimize the package for speed on problems in FLIM analysis.

Acknowledgments

This research was funded by Computational Science grant #635.000.014 from the Netherlands Organization for Scientific Research (NWO) and by the Sandwich Programme of Wageningen University. An anonymous reviewer is thanked for helpful suggestions regarding the presentation of results.

References

Bajzer, Z., A. Zelic and F. G. Prendergast (1995). Analytical approach to the recovery of short fluorescence lifetimes from fluorescence decay curves. *Biophys. J.* **69**(3): 1148-1161.

Barber, P. R., S. M. Ameer-Beg, J. D. Gilbey, R. J. Edens, I. Ezike and B. Vojnovic (2005). Global and pixel kinetic data analysis for FRET detection by multi-photon time-domain FLIM. *Proc. SPIE* **5700**: 171-181.

Becker, W. and A. Bergmann (2003). Lifetime imaging techniques for optical microscopy. Technical report, Becker & Hickl GmbH. *www.becker-hickl.de/pdf/tcvgbh1.pdf.*

Becker, W., A. Bergmann, C. Biskup, T. Zimmer, N. Kloecker and K. Benndorf (2002). “Multiwavelength TCSPC lifetime imaging.” *Proc. SPIE* **4620**: 79-84.

Becker, W., A. Bergmann, H. Wabnitz, D. Grosenick and A. Liebert (2001). “High-count-rate multichannel TCSPC for optical tomography. *Proc. SPIE* **4431**: 249-254.

Borst, J. W., M. A. Hink, A. v. Hoek and A. J. W. G. Visser (2003). Multiphoton microspectroscopy in living plant cells. *Proc. SPIE* **4963**: 231-238.

Borst, J. W., M. A. Hink, A. van Hoek and A. J. Visser (2005). Effects of refractive index and viscosity on fluorescence and anisotropy decays of enhanced cyan and yellow fluorescent proteins. *J Fluoresc* **15**(2): 153-60.

Golub, G. and V. Pereyra (2003). Separable nonlinear least squares: the variable projection method and its applications. *Inverse Problems* **19**(2): R1-R26.

Golub, G. H. and R. J. LeVeque (1979). Extensions and uses of the variable projection algorithm for solving nonlinear least squares problems. *Proceedings of the 1979 Army Numerical Analysis and Computers Conference ARO Report* **79**-3: 1-12.

Grailhe, R., F. Merola, J. Ridard, S. Couvignou, C. Le Poupon, J. P. Changeux and H. Laguitton-Pasquier (2006). Monitoring protein interactions in the living cell through the fluorescence decays of the cyan fluorescent protein. *Chemphyschem* **7**(7): 1442-1454.

Gratton, E., S. Breusegem, J. Sutin and Q. Q. Ruan (2003). Fluorescence lifetime imaging for the two-photon microscope: time-domain and frequency-domain methods. *J. Biomed. Opt.* **8**(3): 381-390.

Grinvald, A. and I. Z. Steinberg (1974). Analysis of fluorescence decay kinetics by method of least-squares. *Anal. Biochem.* **59**(2): 583-598.

Henry, E. R. (1997). The use of matrix methods in the modeling of spectroscopic data sets. *Biophys. J.* **72**(2): 652-673.

Istratov, A. A. and O. F. Vyvenko (1999). Exponential analysis in physical phenomena. *Review Scientific Instruments* **70**(2): 1233-1257.

Maus, M., M. Cotlet, J. Hofkens, T. Gensch, F. C. De Schryver, J. Schaffer and C. A. M. Seidel (2001). An experimental comparison of the maximum likelihood estimation and nonlinear least squares fluorescence lifetime analysis of single molecules. *Anal. Chem.* **73**(9): 2078-2086.

Mullen, K. M. and I. H. M. van Stokkum (2007). TIMP: An R package for modeling multiway spectroscopic measurements. *Journal Statistical Software* **18**(3): -.

Mullen, K. M., M. Vengris and I. H. Stokkum (2007). Algorithms for separable nonlinear least squares with application to modelling time-resolved spectra. *J. Global Optimization* **38**(2): 201-213.

Pelet, S., M. J. R. Previte, L. H. Laiho and P. T. C. So (2004). A fast global fitting algorithm for fluorescence lifetime imaging microscopy based on image segmentation." *Biophys. J.* **87**(4): 2807-2817.

Peter, M., S. M. Ameer-Beg, M. K. Y. Hughes, M. D. Keppler, S. Prag, M. Marsh, B. Vojnovic and T. Ng (2005). Multiphoton-FLIM quantification of the EGFP-mRFP1 FRET pair for localization of membrane receptor-kinase interactions. *Biophys. J.* **88**(2): 1224-1237.

R Development Core Team. (2008). "R: a language and environment for statistical computing." R Foundation for Statistical Computing, Viena. *http://www.R-project.org.*

Russinova, E., J.-W. Borst, M. Kwaaitaal, A. Cano-Delgado, Y. Yin, J. Chory and S. C. de Vries (2004). Heterodimerization and endocytosis of Arabidopsis brassinosteroid receptors BRI1 and AtSERK3 (BAK1). *Plant Cell*: **16**:3216-3229.

Suhling, K., P. M. French and D. Phillips (2005). Time-resolved fluorescence microscopy. *Photochem Photobiol Sci* **4**(1): 13-22.

Tsien, R. Y. (1998). The green fluorescent protein. *Annu. Rev. Biochem.* **67**(1): 509-544.

Verveer, P. J., A. Squire and P. I. H. Bastiaens (2000). Global analysis of fluorescence lifetime imaging microscopy data. *Biophys. J.* **78**(4): 2127-2137.

Chapter 5

Global analysis of Förster resonance energy transfer in live cells measured by fluorescence lifetime imaging microscopy exploiting the rise time of acceptor fluorescence

based on:
S. P. Laptenok, J. W. Borst, K. M. Mullen, I. H. M. van Stokkum, A. J. W. G. Visser, H van Amerongen, Global analysis of Förster resonance energy transfer in live cells measured by fluorescence lifetime imaging microscopy exploiting the rise time of acceptor fluorescence. Submitted

Abstract

A methodology is described for the detection of Förster Resonance Energy Transfer (FRET) in live cells by monitoring the rise time of the acceptor fluorescence using fluorescence lifetime imaging microscopy (FLIM). An advantage of this method is that only those molecules are monitored that are involved in the energy-transfer process. The method relies on global analysis of FLIM images. As a result, a more accurate characterization of the amount of FRET occurring in a given system is obtained as compared to existing methodologies. Previous methods for the estimation of FRET efficiencies from FLIM data rely on estimation of the decay rate of donor fluorescence, which usually is a mixture of the populations of donor molecules that are involved in FRET and those that are fluorescent but not involved in FRET. Alternatively, parameters describing the rise of acceptor fluorescence and the decay of the donor fluorescence can be determined via simultaneous global analysis of multiple FLIM images, thereby increasing the reliability of the analysis. In the present study plant protoplasts transfected with fusions of visible fluorescent proteins are used to illustrate the new data analysis method. It is demonstrated that the distances estimated with the present method are substantially smaller than those estimated from the average donor lifetimes. Software to reproduce the presented results is provided in an open-source and freely available package called "**TIMP**" for "The **R** project for Statistical Computing".

5.1 Introduction

The detection of protein-protein interactions in a biological cell can provide a better understanding of protein function and of mechanisms that regulate intracellular processes (Immink et al. 2002; Vojnovic 2007). In order to monitor these protein interactions in a living cell, Förster Resonance Energy Transfer (FRET) imaging techniques have been developed for the visualization of these processes. FRET is a photophysical process where excitation energy of a donor molecule is transferred non-radiatively to an acceptor molecule if both molecules are in close proximity (within 10 nm) (Yan and Marriott 2003). The use of genetically encoded visible fluorescent proteins coupled to proteins of interest allows the monitoring of the localization of specific proteins in cellular systems. Co-localization studies, however, do not demonstrate physical interactions between proteins and therefore FRET microscopy methods have been developed in order to use the rate of FRET as a "spectroscopic ruler" to analyze protein interactions in biological systems (Stryer 1978; Jares-Erijman and Jovin 2006).

There are several methods for the quantification of FRET using fluorescence intensities, spectra or lifetimes (Pelet et al. 2006). Since FRET is a fluorescence quenching process, it can be measured and characterised based on the fluorescence lifetime of donor molecules (Lakowicz 2006). The fluorescence lifetime can be defined as the average time that a molecule remains in the excited state, and strongly depends on the local environment of the fluorophore and on the fact whether FRET occurs. FLIM is a widely used imaging technique, which allows mapping of fluorescence lifetimes with (sub)nanosecond time resolution and a diffraction-limited, spatial resolution of approximately 250 nm. Therefore, FRET phenomena measured with a FLIM setup can provide temporal and spatial information about protein dynamics and molecular interactions in cells (Bastiaens and Squire 1999).

For accurate and quantitative analysis of FLIM data, well-designed data analysis protocols are required. Significant advantages and improved accuracy in data analysis can be achieved by applying global analysis. When data from different measurements are analyzed simultaneously, the utilization of the assumption that some parameters are invariant during different experiments significantly increases the precision of the analysis (Beechem 1992). The dynamical features of a fluorescence decay are often well described by a small number of kinetic processes, for which the associated fluorescence lifetimes in all pixels have similar values, but the relative intensity values may vary from pixel to pixel (Bednarkiewicz and Whelan 2008).

Global analysis can be used to accurately detect FRET phenomena by estimating the fluorescence lifetimes of donor molecules in the absence and presence of acceptor molecules. When FRET occurs, the donor fluorescence lifetime in the presence of an acceptor becomes shorter as compared to the fluorescence lifetime of the donor-only case. The shortening of the donor fluorescence lifetime is an indicator of FRET, and the difference between the donor fluorescence lifetime with and without acceptor allows quantification of the FRET efficiency. However, a complicating issue is the fact that FRET systems are not always purely homogeneous, since they can contain a population of non-interacting donor molecules (Paul et al. 2005). As a consequence, the average donor lifetime then originates from interacting and non interacting species. Therefore, the donor fluorescence lifetime does not reflect the true FRET efficiency, and distances between molecules calculated based on the efficiency are overestimated (Wlodarczyk et al. 2008). Another method of measuring FRET uses the detection of the rise time of acceptor fluorescence following donor excitation. The main advantage of this approach is that only those molecules are monitored that are involved in energy transfer (Borst et al. 2008). The lifetime of the donor in the presence of the acceptor can be directly determined from the acceptor rise time. This allows calculation of the rate of excitation energy transfer. However, an accurate determination of the fluorescence lifetime of donor molecules in the absence of acceptor is still required.

Here, a global analysis technique is described where the rise time of the acceptor fluorescence is quantitatively monitored after donor excitation in order to quantify FRET in live cells and multiple FLIM images are analyzed simultaneously in order to increase the precision of the transfer rate determination. The global analysis has been performed on plant protoplasts, which were transfected with fusions of visible fluorescent proteins. For detection of the rise time of the acceptor fluorescence two constructs were used. The first one was composed of Enhanced Cyan Fluorescence Protein (ECFP) linked to Enhanced Yellow Fluorescence Protein (EYFP) by thirteen amino acids and the second one of Enhanced Green Fluorescence Protein (EGFP) linked to the red fluorescent protein mCherry by six amino acids. The transfected protoplasts were imaged using FLIM and the characteristic fluorescence rise and decay times were measured with two different detection windows for each pair.

5.2 Materials and methods

5.2.1 FLIM

FLIM images were recorded using the setup previously described in detail by Borst and coworkers (Borst et al. 2003). Briefly, the measurement instrumentation involves a Bio-rad Radiance 2100 MP system coupled to a Nikon TE300 inverted microscope. To obtain two-photon excitation a Ti:Sapphire laser (Coherent Mira D900) (Coherent Inc., Santa Clara, CA) pumped by a 5W solid state laser (Coherent Verdi V5) (Coherent Inc., Santa Clara, CA) is used to generate 150-femtosecond pulses with center wavelength 860 nm and repetition rate 76 MHz. Excitation light is focused using an apochromat 60x water immersion objective lens (CFI Plan Apochromat, numerical aperture 1.2, Nikon, Tokyo, Japan). Fluorescence is detected via different band-pass filters using the time-correlated single photon counting technique (TCSPC) by a Hamamatsu R3809U microchannel-plate photomultiplier operated at 3.1 kV (Hamamatsu Photonics, Hamamatsu, Japan) coupled to a single photon counting module SPC 730 (Becker and Hickl, Berlin, Germany). All images are acquired with a 64x64 pixels frame size and analog-to-digital converter (ADC) set to 256 channels resulting in a 48-ps/channel time interval.

5.2.2 Experimental system

cDNA fusions of EGFP (donor) linked to mCherry (acceptor) by six amino acids (GSGSGS) (EGFP-L-mCherry) and ECFP (donor) coupled to EYFP (acceptor) via a 13-amino acid linker (RGGGGARDPPVAT) (ECFP-L-EYFP) were constructed. Plant protoplasts were transfected as described by Aker and coworkers. (Aker et al. 2007). FLIM measurements on the protoplasts expressing the fusion proteins were imaged by collecting fluorescence using an appropriate band-pass filter. The ECFP fluorescence was detected using a 480-nm (30 nm width) band pass filter from protoplasts expressing the ECFP-L-EYFP fusion protein. For the detection of EYFP fluorescence a band-pass filter of 542 nm (35 nm width) was used and the images were obtained using an acquisition time of 150 s. EGFP fluorescence was detected using a 525 nm band-pass filter (50 nm width) using an acquisition time of 80 s. The fluorescence of mCherry was detected through a 590 nm band-pass filter (30 nm width) using an acquisition time of 300 s. To build up a fluorescence decay with a sufficient amount of counts, decay traces from nine neighboring pixels were summed up resulting in a so-called binning factor of 1. The localization of the fusion proteins could be observed both in the cytoplasm and nucleus of the plant cell because of the absence of a signal peptide. The image size in both case studies was 15 μm x 15 μm.

5.2.3 Summary of FRET theory

The lifetime of a fluorophore τ is the average time that the molecule stays in the excited state after response to an excitation pulse, and is given as a function of the radiative (k_r) and non-radiative (k_{nr}) rate constants:

$$\tau = \frac{1}{k_r + k_{nr}} \tag{1}$$

The fluorescence lifetime strongly depends on the environment of the fluorophore. It can therefore be used for probing the environment that changes under different conditions. The fluorescence lifetimes were determined using the time-correlated single photon counting (TCSPC) methodology spatially resolved using FLIM (for details see Becker (2005)). The time-dependence of fluorescence intensity in the most simple case is described by a single exponential decay $I(t) = I_0 e^{-t/\tau}$, where I_0 is the intensity at $t = 0$.

FRET is a bimolecular process in which the excited-state energy of a donor fluorophore is non-radiatively transferred with rate constant (k_t) to a ground-state acceptor molecule by dipole-dipole interaction (figure 1). For the situation shown in figure 1, the excited state population of the system after excitation of the donor (component D) with a δ-pulse can be described by the following set of equations:

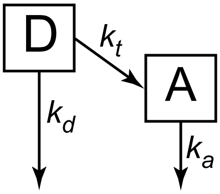

Figure 1. *Compartmental model for a molecular system with FRET. D represents the excited donor population and A the excited acceptor population. The rate constants k_d and k_a correspond to decay to the ground state for donor and acceptor, respectively and k_t is the rate of energy transfer from donor to acceptor.*

$$\begin{cases} \dfrac{dD(t)}{dt} = -(k_d + k_t)D(t) \\ \dfrac{dA(t)}{dt} = D(t)k_t - A(t)k_a \end{cases} \tag{2}$$

where $D(t)$ is the fluorescence intensity (proportional to the number of excited molecules) of the donor molecule, $A(t)$ is the fluorescence intensity (proportional to number of excited molecules) of the acceptor, k_d is the rate constant of donor-molecule de-excitation in the absence of the acceptor and is equal to (k_r+ k_{nr}), k_a is the acceptor de-excitation rate constant and k_t is the rate constant of resonance energy transfer. Solving eqs. 2 results in the following functions describing the decay of fluorescence intensity of the donor and acceptor as:

$$\begin{aligned} D(t) &= D_0 e^{-(k_d+k_t)t} \\ A(t) &= -\frac{D_0 k_t}{k_d + k_t - k_a} e^{-(k_d+k_t)t} + \frac{D_0 k_t}{k_d + k_t - k_a} e^{-k_a t} \end{aligned} \tag{3}$$

where D_0 is the fluorescence intensity of the donor at $t = 0$. The negative term in the expression of $A(t)$ reflects a rise component due to energy transfer from donor to acceptor with rate constant (k_d+ k_t). In the ideal case the absolute value of the ratio between negative and positive amplitudes is equal to 1, when acceptor molecules receive energy only from donor molecules via FRET. In practice, however, this situation is almost never observed because part of the acceptor molecules is excited directly and/or some donor fluorescence is observed in the detection window of acceptor fluorescence. In this case fluorescence, detected in the acceptor channel, besides *A(t)* from eq. 3, will contain more terms with positive amplitudes coming from directly excited acceptor molecules and/or donor molecules. Therefore the absolute value of the ratio between negative and positive amplitudes will be smaller than 1.

The lifetime of donor molecules in the presence of FRET will be shorter in comparison to the lifetime of the donor in the absence of acceptor and can be calculated using

$$\tau_{da} = \frac{1}{k_d + k_t} \tag{4}$$

As is clear from eq. 3 the rate of the rise of acceptor fluorescence is equal to the decay rate of donor fluorescence in the presence of the acceptor, and it can be used for estimation of the transfer rate constant as:

$$k_t = k_{da} - k_d \tag{5}$$

or in lifetime notation:

$$k_t = \frac{1}{\tau_{da}} - \frac{1}{\tau_d} \tag{6}$$

The transfer rate (k_t) is proportional to the inverse 6th power of the distance *R* between donor and acceptor, which makes it an extremely sensitive parameter for obtaining distances less than 10 nm:

$$k_t = k_d \left(\frac{R_0}{R} \right)^6 \tag{7}$$

where R_0 - is the so-called critical or Förster radius (Förster 1949), the distance between donor and acceptor, at which 50% of the donor energy is transferred to the acceptor.

In most cases multi-exponential analysis has to be applied to describe the observed fluorescence in time, and the amplitude-averaged lifetime $<\tau>$ can be useful, being defined as:

$$<\tau> = \sum_i \alpha_i \tau_i \qquad \sum_i \alpha_i = 1 \tag{8}$$

where τ_i- is the lifetime of component *i*, and a_i-is the fractional contribution of component *i*.

5.2.4 FLIM data analysis

For each pixel in a FLIM image, the fluorescence is measured as a function of time. The recording of the decay for each pixel can be considered as separate experiments. The resulting data can be stored as a matrix in which each column represents the fluorescence decay associated with a single pixel *x*, so that

$$\Psi = \left[\begin{array}{c|cccc} & x_1 & x_2 & \cdots & x_n \\ \hline t_1 & \psi(t_1,x_1) & \psi(t_1,x_2) & \cdots & \psi(t_1,x_n) \\ t_2 & \psi(t_2,x_1) & \psi(t_2,x_2) & \cdots & \psi(t_2,x_n) \\ \vdots & \vdots & \vdots & \ddots & \vdots \\ t_m & \psi(t_m,x_1) & \psi(t_m,x_2) & \cdots & \psi(t_m,x_n) \end{array}\right] \tag{9}$$

where $\mathbf{\Psi}(t_i, x_j)$ is the fluorescence intensity at time ti in pixel x_j. In practice, the fluorescence decay can often be described well as a sum of exponential decays convolved with the instrumental response function (IRF), so that the decay model for a single pixel reads as:

$$F(t) = \sum_i a_i \exp\left(-\frac{t}{\tau_i}\right) \otimes g(t) \tag{10}$$

where the summation is over the number of components n_{comp} of the decay, τ_i is the lifetime of component *i*, a_i is the fractional contribution of component *i* to the fluorescence decay, *g(t)* is the instrumental response function and is the convolution operator. Often, the IRF is not represented well by a simple analytical function, and therefore it is usually measured and numerically convolved with the exponential decay model for each component. Various algorithms for numerical convolution of an exponential decay with a measured IRF can be applied. The iterative reference and scatter methods described in (Grinvald and Steinberg 1974; Vos et al. 1987; Boens et al. 1988) have been found to perform well in practice, and are implemented in the package **TIMP** for "The **R** project for statistical computing" that is used in this study (R Development Core Team 2008).

The assumption that the fluorescence lifetime components are spatially invariant is a crucial one for global analysis of a FLIM image, which has been justified by Verveer and co-workers (Verveer et al. 2000). Under this assumption, the matrix dataset associated with a single FLIM image $\mathbf{\Psi}$ is modelled as

$$\mathbf{\Psi} = \mathbf{C}\mathbf{A}^T + \mathbf{Z} = \sum_{i=1}^{n_{comp}} c_i a_i^T + \mathbf{Z} = \sum_{l=1}^{n_{comp}} (\exp(-t/\tau_i) \otimes g(t)) a_i^T + \mathbf{Z} \tag{11}$$

where column *i* of the matrix **C** represents the time profile of component *i* of the fluorescence decay, and column *i* of the matrix **A** represents the amplitude of component *i* over all pixels. The free parameters of the model are the n_{comp} lifetimes τ_i and for each pixel the n_{comp} amplitude parameters describing the fluorescence decay, collated in n_{comp} vectors a_i, each of length npixel.

The stochastic component of the model is assumed to consist of an additive Gaussian noise term **Z** with the same dimensionality as the data matrix. Note that the modeled data represent non-negative counts of the number of photons detected per pixel and per time interval, to which Poissonian noise statistics apply. However, as Maus and coworkers (Maus et al. 2001) have studied in depth, using a Gaussian approximation for the Poisson noise statistics introduces negligible errors to the parameter estimates as long as the data represent mostly a large number of counts, which is the case for the data considered here.

The parameter estimation problem associated with fitting the model for $\mathbf{\Psi}$ is an example of a separable nonlinear least squares optimization problem (Golub and Pereyra 2003). The variable projection algorithm developed by Golub and Pereyra (Golub and Pereyra 1973) has many advantages over other techniques for separable nonlinear least squares problems, and relies on analytically eliminating the conditionally linear amplitude parameters ai from the residual function. Variable projection for application to time-resolved microscopy data has recently been reviewed by Mullen and van Stokkum (Mullen and Stokkum 2008). The applicability of variable projection for fitting FLIM data was demonstrated by a variety of simulation studies (Laptenok et al. 2007). Verveer and co-workers (Verveer et al. 2000) realized that variable projection could be used in principle for fitting models to the FLIM data, but were not able to apply this method due to the large memory requirements of their implementation. A memory-saving version of the algorithm used in this study has been implemented in the **TIMP** package and is discussed in (Mullen and Stokkum 2008).

The properties of the fluorescence decay are expected to be identical in each of the FLIM images that result from the same sample preparation procedure. In order to use all available data to estimate the lifetimes of the fluorescence decay of the components, a global analysis model of multiple datasets has been formulated, in which the same number of fluorescence rise and decay times underlie the decay kinetics across multiple images. Each image is associated with a possibly distinct measured IRF curve. The amplitude parameters of each component of the decay were estimated per pixel. Global analysis models for the simultaneous analysis of multiple FLIM images are discussed in detail in (Mullen and Stokkum 2008). Singular Value Decomposition (SVD) (Golub and Loan 1996) of the residual matrix associated with each FLIM image has been used to diagnose the fit quality and the presence of systematic errors in the data as discussed in (Hoff et al. 1994; van Stokkum et al. 2004). The amplitude of the first right singular vectors of the residuals can be mapped to the pixels analyzed in order to pinpoint regions with bad fitting results. Any misfit in the time-domain will be reflected in the structure and amplitude of the left singular vectors of the residuals. In an ideal model fit, the left singular vectors of the residual matrix show no trends and its singular values are small when compared to those of the data.

5.3 Results and discussion

5.3.1 ECFP-EYFP construct

ECFP is widely used as a donor molecule in FRET studies but it shows bi-exponential fluorescence dynamics even in the absence of FRET (Tramier et al. 2002; Borst et al. 2005). Figure 2 shows the global analysis results for a plant protoplast which is transfected with ECFP molecules. In figure 2A the fluorescence intensity image of the plant protoplast is shown and the brightness of the pixel codes for the number of detected photons. Only the region of the nucleus was selected for further analysis. Fluorescence lifetimes were linked for all pixels within the region of interest in the analysis procedure. A bi-exponential fit leads to a satisfactory description of the data with lifetimes of 0.61±0.02 ns (average contribution 26%) and 2.97±0.01ns (average contribution 74%) which results in an average lifetime calculated with eq. 8 of $<\tau> = 2.36$ ns. The false-color lifetime image of the analyzed area

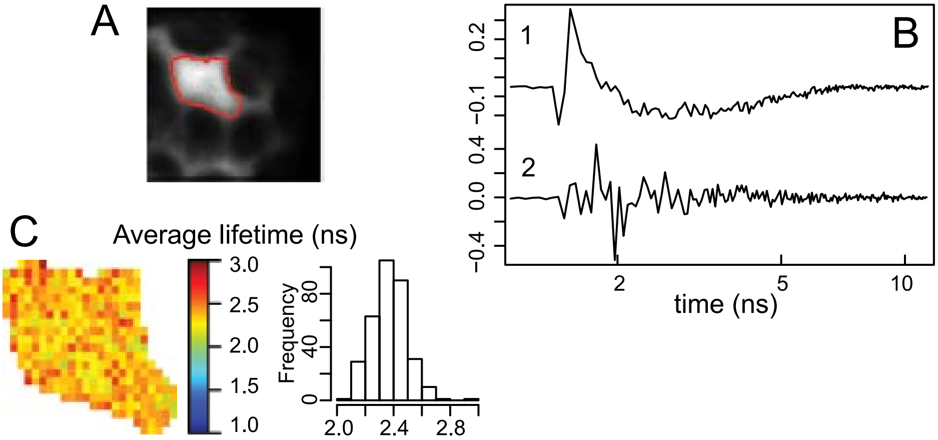

Figure 2. *Results of global analysis of ECFP fluorescence in plant protoplasts; detection at 465 – 495 nm (ECFP). (A) intensity image, red contour indicates region selected for analysis, (B) first left singular vectors of the residuals matrix (1. mono-exponential analysis, 2 bi-exponential analysis). (C) histogram and spatial distribution of average lifetime of ECFP after analysis using a bi-exponential model,*

from the protoplast transfected with ECFP is shown in figure 2C. The color reflects the average fluorescence lifetime calculated with eq. 8 from a bi-exponential fit for each pixel in the region of interest and the frequency of the average lifetimes is shown in the histogram. It is clear that the average fluorescence lifetimes are almost the same for all pixels within the selected region. The first left singular vector of the residual matrix, which serves as an overall fit quality indicator, is given in figure 2B. The noise-like fluctuations around zero in case of bi-exponential analysis shows that the quality of the fit is not systematically biased. Both lifetime components correspond to populations with two different chromophore structures in ECFP (Hyun Bae et al. 2003) yielding a quenched fluorophore (0.61 ns) and an unquenched one (2.97 ns). Both populations can transfer excitation energy to a nearby acceptor. Therefore, in the presence of an acceptor at least a four-exponential model is needed to include both transferring and non-transferring donor molecules (Borst et al. 2008). The estimation of four fluorescence lifetimes and the corresponding amplitudes is impossible given the typical quality of FLIM data. However, analysis of the rise of the acceptor fluorescence can be used for a more accurate determination of FRET efficiency. The fluorescence of plant protoplasts transfected with ECFP-L-EYFP were recorded at two different detection wavelengths. First, images measured with the 542 nm band-pass filter (EYFP fluorescence detection window) were analyzed globally. The global analysis results for one representative protoplast using a bi-exponential model for the fluorescence kinetics are presented in figure 3. It shows the presence of a rise component (i.e. negative amplitude) of 0.58±0.02 ns and a decay component of 3.05±0.01 ns. The rise time of the acceptor fluorescence corresponds to resonance energy transfer and the decay time corresponds to fluorescence of mainly EYFP (Ganesan et al. 2006; Borst et al. 2008). The spatial distribution of the absolute value of the ratio between the negative and positive amplitudes is depicted in pseudo-color code in figure 3B. It shows

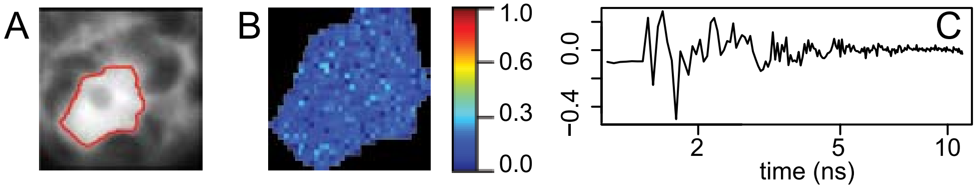

Figure 3. *Global analysis results of a representative image of a protoplast transfected with ECFP-L-EYFP detected with a 542 nm band-pass filter (EYFP fluorescence is detected). Global analysis was performed with a bi-exponential model. (A) fluorescence intensity image where the red contour indicates the region that is analyzed, (B) spatial distribution of the absolute value of the ratio between the negative and positive amplitudes of the fast and slow components, respectively, (C) first left singular vector of residuals.*

a homogeneous and narrow distribution of this value. The ratio is smaller than 1 because of the presence of both fluorescence arising from donor molecules and/or from directly excited acceptor molecules. The first left singular vector of the residual matrix, serving as an overall fit quality indicator in the time dimension, is given in figure 3C and shows the good quality of the fit.

Results of the global analysis of the images observed in the donor detection window are presented in figure 4. The bi-exponential analysis shows fluorescence lifetimes of 0.37±0.01 ns (average contribution 44%) and 2.24±0.01 ns (average contribution 56%),

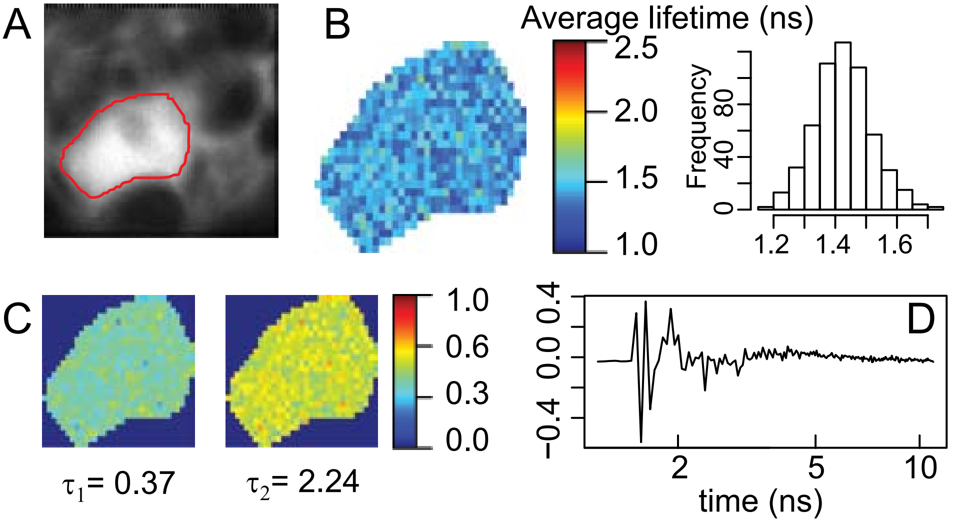

Figure 4. *Results of global analysis of plant protoplasts with expressed ECFP-L- EYFP. Detection at 465-495 nm (ECFP). (A) intensity image, red contour indicates region selected for analysis, (B) histogram and spatial distribution of average lifetime after analysis using a bi-exponential model, (C) fractional contributions of the fast and slow components, (D) first left singular vector of the residual matrix, which is not completely randomly distributed around 0, indicating that the number of components in the fit is not entirely sufficient.*

which results in an average lifetime of 1.42 ns. Figure 4C shows a homogeneous and narrow spatial distribution of the fractional contribution of the components. Although the first left singular vector of the residual matrix (figure 4D) shows the possible presence of an additional decay component, the analysis using a three-exponential model is unstable, whereas one might even expect the presence of four decay components. Therefore, it is impossible to translate the obtained amplitudes directly into percentages of transferring and non-transferring donor molecules. However, the distribution of average lifetimes can be used for a first preliminary qualitative analysis of the images.

Results of global analysis of different images, measured at both detection windows, are shown in figure 5 (1 – detection of donor fluorescence, 2 – detection of acceptor fluorescence). Representative traces with estimated lifetimes for both detection windows are given in figure 5D. Global analysis of the FLIM images detected in both detection windows has provided the possibility to resolve an additional donor decay component and it increases the

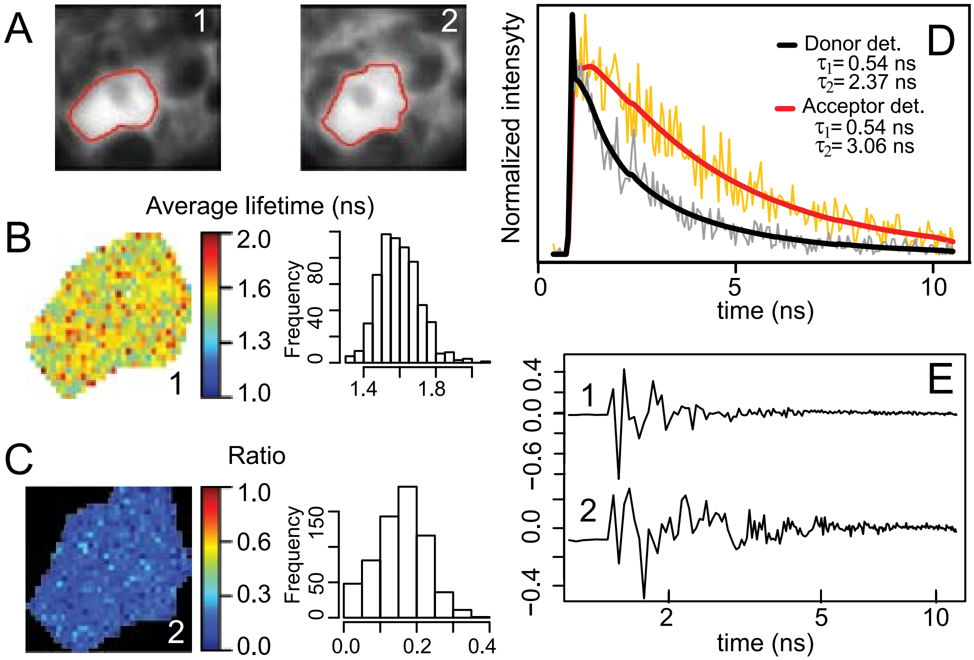

Figure 5. *Results of global analysis of plant protoplasts with expressed ECFP–L-EYFP. (A) intensity images, red contour indicate regions selected for analysis (1-ECFP detection 469 – 495nm, 2 - EYFP detection 524 – 559nm) (B) histogram and spatial distribution of the average fluorescence lifetime of ECFP obtained from a three-exponential fit excluding the component of 91 ps that represents auto-fluorescence, (C) histogram and spatial distribution of the absolute value of the ratio between the negative and positive amplitudes of the EYFP fast and slow kinetics components, respectively, (D) representative traces and fits result for both detection channels, (E) first left singular vectors of the residual matrices for the given cells; the fitting of the donor channel is somewhat better than that of the acceptor channel.*

precision of the fluorescence lifetime estimates. The analysis was performed by applying a bi-exponential model for the acceptor detection window and a three-exponential model for the donor detection window. The FRET component was linked between all images and the fluorescence lifetimes that correspond to the decay times of non-transferring donor molecules and of acceptor molecules were linked only between images measured at the same wavelength. The analysis results in lifetimes for ECFP fluorescence of 0.091±0.04 ns, 0.54±0.2ns and 2.37 ±0.01 ns. The 0.09-ns component probably corresponds to auto-fluorescence; fluorescence stemming from chloroplasts using the same excitation and detection wavelength is characterized by a lifetime of 0.1 ns (data not shown). The 0.09-ns component was therefore excluded from further calculations. Estimates of the fluorescence lifetimes that corresponds to FRET and their amplitudes are summarized in Table 1. Because of the presence of two transferring conformations of the ECFP chromophore with slightly different rate constants one can expect the presence of two different rise times of the acceptor fluorescence. However, given the limited signal to noise ratio and time resolution, two components in the rise part of the acceptor fluorescence cannot be resolved. Moreover, these two rise times become closer at increasing transfer rate, making it impossible to resolve separate components.

The 2.37-ns component in the donor channel represents the average fluorescence lifetime of non-interacting ECFP. This lifetime is nearly identical to the value of 2.36-ns obtained from the analysis of cells with free ECFP expressed (Figure). The 0.54 ns component mainly represents an average lifetime of interacting ECFP molecules (but see also below), and can be used, together with the average lifetime of 2.36 ns for non-interacting ECFP, to calculate a transfer rate constant using eq. 6. This leads to a transfer rate of 1.43 ns^{-1}, which corresponds to an estimated distance between chromophores of 4.0 nm, using R_0=4.9 nm (Borst et al. 2008). More accurate estimates of the transfer rate can be calculated by solving the quadratic eq. 12, which can be derived from eqs. 4 and 8 with the assumption that both

***Table 1** Estimates of fluorescence lifetimes after separate and simultaneous analysis of plant protoplasts containing ECFP linked to EYFP detected at two detection windows*

	τ_1 (ns)	α_1	ρ^*	τ_2 (ns)	α_2
Separate analysis of images from donor and acceptor detection channel					
ECFP detection 469 – 495nm	0.61±0.03	0.26		2.97±0.01	0.74
ECFP-L-EYFP detection 469 – 495nm	0.37±0.01	0.44		2.24±0.01	0.56
ECFP-L-EYFP detection 524 – 559nm	0.58±0.03		0.18	3.05±0.01	
Global analysis of images from donor and acceptor detection channel†					
ECFP-L-EYFP detection 469 – 495nm	0.54±0.02	0.43		2.37±0.01	0.57
ECFP-L-EYFP detection 524 – 559nm			0.18	3.06±0.01	

* ρ - *absolute value of the ration between negative and positive amplitudes estimated from the analysis of the images from acceptor detection channel.*

† *note that in global analysis case the component of 91 ps that represents auto-fluorescence was excluded from the calculation.*

ECFP conformations are transferring excitation energy with the same rate constant.

$$\tau_{da} = \frac{\alpha}{\frac{1}{\tau_1} + k_t} + \frac{1-\alpha}{\frac{1}{\tau_2} + k_t} \tag{12}$$

where τ_1 and τ_2 are lifetimes of the ECFP molecules in the absence of acceptor, α is the relative contribution of the first component, k_t is the transfer rate constant and τ_{da} is the estimated rise time. Solving eq. 12 gives a transfer rate constant $k_t = 1.29\ \text{ns}^{-1}$ and a distance between the chromophores of 4.1 nm. The estimated distances in the case of ECFP-L-EYFP (4.1 nm) is in good agreement with the distance of 3.9 nm obtained by Evers and co-workers (Evers et al. 2006) for the shortest linker of 23 amino acids in their macroscopic measurements and simulations. The linker of 23 amino acids in their study corresponds to a linker of 12 amino acids length linker in the present study (due to a different numbering). On the other hand, the distance calculated from the average donor lifetimes is 5.71 nm, which is too long. The distances estimated using different approaches are summarized in Table 2. It should be noted that the fitted decay time of 0.54 ns for the donor fluorescence is close to the 0.61 ns time that is observed for ECFP that is not linked to EYFP. The presence of some non-transferring ECFP might therefore contribute to the 0.54 ns time. However, the fitted acceptor rise time was very similar when global analysis of the donor decay was included (0.54 ns) or not included (0.58 ns). Therefore, the presence of non-transferring ECFP does not substantially influence the estimated transfer time.

Table 2. *Estimated distances between ECFP and EYFP chromophores*

Calculation method	Calculated distance (nm)
A	4.0
B	4.1
C	5.7
D	3.9

(A) rise time of acceptor fluorescence (0.54 ns), (B) rise time of acceptor fluorescence and assumption that both conformations of ECFP transfer with the same rate, (C) average donor lifetime in the presence and absence of acceptor, (D) distance observed by Evers and co-workers for 12 amino acids length linker.

5.3.2 EGFP-mCherry construct

The quantitative analysis of FLIM data is simplified considerably when donor molecules show single-exponential fluorescence behavior in the absence of acceptor molecules, like is for instance the case for EGFP (Tramier et al. 2006). In order to check the fluorescence kinetics of EGFP in live cells, FLIM images of plant protoplasts transfected with only EGFP were analyzed. The fluorescence decay of EGFP molecules can well be described by a single exponential with a fluorescence lifetime of 2.45±0.01 ns (results not shown). Global analysis of FLIM images of plant protoplasts transfected with EGFP-L-mCherry measured with the 525 nm band-pass filter (EGFP fluorescence detection window) are presented in figure 6.

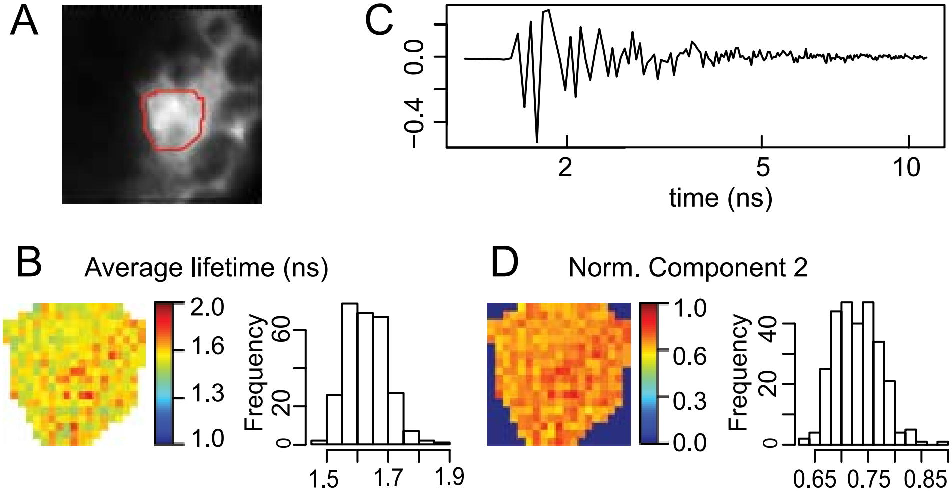

***Figure 6**. Global analysis results of a representative image of a protoplast transfected with EGFP-L-mCherry detected with a 525 nm band-pass filter (EGFP). Global analysis was performed with a bi-exponential model. (A) Fluorescence intensity image where the red contour indicates the region that is analyzed, (B), (D) spatial distribution and histogram of the average lifetimes and fractional contributions of the slow component. The average lifetime is around 1.65 ns with a narrow distribution, whereas the amplitude of the slow component is around 0.70-0.75, (C) first left singular vector of residuals matrix, oscillates around zero, which indicates that the quality of the fit is good.*

The analysis using a bi-exponential model results in fluorescence lifetimes of 0.48±0.02 ns with an average contribution of 28% and 2.05±0.003 ns with an average contribution of 72% (figure 6D, table 3) resulting in an average fluorescence lifetime calculated with eq. 8 of $<\tau>$ = 1.2 ns (figure 6B). The lifetime of 2.05 ns is shorter than the unquenched lifetime of 2.45 ns and therefore the amplitudes of the short and long components cannot be directly ascribed to the fractions of interacting and non-interacting molecules.

FLIM images of the same plant protoplasts were also measured using a 590-nm band-pass filter to detect the rise of the acceptor fluorescence. The images were globally analyzed using a bi-exponential model. Analysis revealed the presence of a rise component of 0.58±0.02 ns, reflecting energy transfer from EGFP to mCherry and a decay component of 2.01±0.003 ns, which can mainly be attributed to mCherry fluorescence. The rise time can be used for calculating the transfer rate (eq. 6). The fluorescence lifetimes after separate analysis of the donor and acceptor detection windows are summarized in table 3. A bi-exponential model was used for the simultaneous analysis of images obtained with both detection windows. The results are presented in figure 7.

The fluorescence lifetime of the shortest component (attributed to the FRET process) was linked between images measured at both detection windows while the lifetime of the long component was only linked between images detected within the same wavelength region. The analysis provides an estimate for the fluorescence lifetime of the short transfer

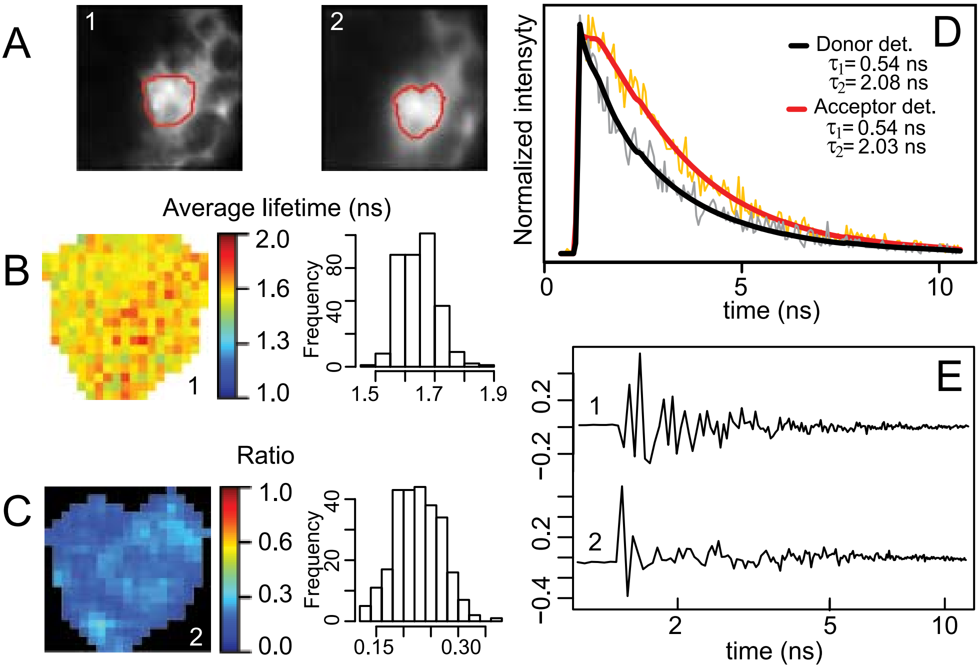

***Figure** 7. Results of global analysis of plant protoplasts with expressed GFP linked to mCherry detected at two detection windows. Note that these are not the same protoplasts. (A) intensity images (1-GFP 525 nm fluorescence detection , 2 - mCherry 590 nm fluorescence detection). Red contours indicate the regions selected for analysis, (B) histogram and spatial distribution of average lifetime of GFP, (C) histogram and spatial distribution of the absolute values of the ratio between the negative and positive amplitudes of the fast and slow components, respectively, detected at 600 nm, (D) representative traces and fit result for both detection channels, (E) first left singular vectors of the residuals for given cells.*

component of 0.54 ns. The longest lifetime is estimated to be 2.08 ns for the donor channel and 2.03 ns for the acceptor channel (Table 3). The lifetime of 2.08 ns is probably an average of 2.45 ns, corresponding to non-transferring EGFP, and a somewhat shorter lifetime, corresponding to slowly transferring EGFP molecules.

The Förster radius R_0 for the FRET pair EGFP-mCherry was calculated as described in (Hink et al. 2003) as

$$R_0 = 0.0211\left\{\kappa^2 n^{-4} Q_D J(\lambda)\right\}^{1/6} \tag{13}$$

with $J(\lambda)$ is the overlap integral of the EGFP emission and mCherry absorption spectra, Q_D is the donor fluorescence quantum yield in the absence of acceptor, which is assumed to be $Q_D=0.60$ (Tsien 1998), n is the refractive index of the medium which is assumed to be $n=1.34$, and which is subject to some uncertainty (Knox and van Amerongen 2002) and κ^2 is the orientation factor, which is assumed to be ⅔. Based on these numbers, a value of R_0 = 5.24 nm is calculated, close to the value of 5.1 nm, which was recently reported by Albertazzi

Table 3. *Estimates of fluorescence lifetimes after separate and simultaneous analysis of plant protoplasts containing EGFP linked to mCherry detected at two detection windows.*

	τ1 (ns)	α1	ρ^*	τ2 (ns)	α2
Separate analysis of images from donor and acceptor detection channel					
EGFP detection 500 – 550nm	2.45±0.01				
EGFP-L-mCherry detection 500 – 550nm	0.48±0.02	0.28		2.05±0.003	0.72
EGFP-L-mCherry detection 585 – 615nm	0.58±0.02		0.25	2.01±0.003	
Global analysis of images from donor and acceptor detection channel					
EGFP-L-mCherry detection 500 – 550nm	0.54±0.01	0.27		2.08±0.01	0.73
EGFP-L-mCherry detection 585 – 615nm			0.25	2.03±0.005	

* ρ - *absolute value of the ratio between negative and positive amplitudes estimated from the analysis of the images from acceptor detection channel.*

and co-workers (Albertazzi et al. 2009). The distance R between the chromophores can now be calculated from eq. 7, using this value of R_0 = 5.24 nm and the transfer time of 0.54 ns. This leads to a distance of R = 4.2 nm. It is very important that the transfer time is being used for this calculation. If one uses the average lifetime of the donor in the presence (1.2 ns) and absence (2.45 ns) of acceptor, one obtains a wrong distance of 5.2 nm.

Despite the fact that the linker is almost twice as long in the case of ECFP-L-EYFP as compared to the case of EGFP-L-mCherry, the estimated distances between the chromophores are almost identical being 4.1 nm and 4.2 nm, respectively. This can be explained by the fact that a flexible linker can give rise to a number of different conformations with different distances and orientations between the chromophores. Even in the case of very long linkers, conformations with short donor-acceptor distances can strongly contribute to the total fluorescence decay (Evers et al. 2006).

5.4 Conclusions

A new methodology has been described for the detection of FRET in living cells. The method allows the accurate determination of the rate of FRET in living cells by globally (both spatially and spectrally) fitting the fluorescence kinetics of donor and acceptor molecules in FLIM measurements. Combining the fitting of the fluorescence kinetics at different detection wavelengths allows to correct for the contribution of molecules that are not able to transfer their excitation energy, whereas the spatial global averaging leads to a substantial reduction of the error margins. In the case of EGFP-L-mCherry the distance between the chromophores is found to be 4.2 nm. In principle, this system is easier to study than the ECFP-L-EYFP construct because isolated EGFP shows a mono-exponential fluorescence decay curve in FLIM, whereas ECFP shows a bi-exponential decay. Nevertheless, an accurate distance determination could also be performed in the latter case, which yields a distance between the chromophores of 4.1 nm.

The main limiting factor of proper analysis of the FLIM data is the signal-to-noise ratio, which at the moment can only be increased by measuring for longer times, However, increasing the acquisition time is in most cases restricted by limited sample stability in live cells. Global analysis is advantageous since it increases the precision of the small number of estimated parameters that are estimated from all data.

Implementation

The data analysis procedures described in the previous sections have been implemented in the package TIMP for the “R project for Statistical Computing (R Development Core Team 2008). TIMP and R are freely available under the terms of the GNU General Public License.

Acknowledgment

This research was funded by the Sandwich Programme of Wageningen University and by the European Community (Marie Curie Research Training Network MRTN-CT-2005-019481 “From FLIM to FLIN”).

References

Aker, J., R. Hesselink, R. Engel, R. Karlova, J. W. Borst, A. J. W. G. Visser and S. C. de Vries (2007). *In vivo* hexamerization and characterization of the Arabidopsis AAA ATPase CDC48A complex using Förster resonance energy transfer-fluorescence lifetime imaging iicroscopy and fluorescence correlation cpectroscopy. *Plant Physiol.* **145**(2): 339-350.

Albertazzi, L., D. Arosio, L. Marchetti, F. Ricci and F. Beltram (2009). Quantitative FRET analysis with the E^{0}GFP-mCherry fluorescent protein pair. *Photochem. and Photobiol.* **85**(1): 287-297.

Barber, P. R., S. M. Ameer-Berg, J. D. Gilbey, R. J. Edens, I. Ezike, and B. Vojnovic 2005. Global and pixel kinetic data analysis for fret detection by multi-photon time-domain flim. *Proc. SPIE.* **5700**:171-181.

Bastiaens, P. I. H. and A. Squire (1999). Fluorescence lifetime imaging microscopy: spatial resolution of biochemical processes in the cell. *Trends Cell Biol* **9**(2): 48-52.

Becker, W. (2005). Advanced time-correlated single photon counting techniques. Berlin, Springer.

Bednarkiewicz, A. and M. P. Whelan (2008). Global analysis of microscopic fluorescence lifetime images using spectral segmentation and a digital micromirror spatial illuminator. *J. Biomed. Opt.* **13**(4).

Beechem, J. M. (1992). Global analysis of biochemical and biophysical data. *Methods in Enzymol*. **210**: 37-54.

Boens, N., M. Ameloot, I. Yamazaki and F. C. De Schryver (1988). On the use and the performance of the delta-function convolution method for the estimation of fluorescence decay parameters. *Chem. Phys.* **121**(1): 73-86.

Borst, J. W., M. A. Hink, A. v. Hoek and A. J. W. G. Visser (2003). Multiphoton microspectroscopy in living plant cells. *Proc. SPIE* **4963**: 231-238.

Borst, J. W., M. A. Hink, A. van Hoek and A. J. Visser (2005). Effects of refractive index and viscosity on fluorescence and anisotropy decays of enhanced cyan and yellow fluorescent proteins. *J Fluoresc* **15**(2): 153-60.

Borst, J. W., S. P. Laptenok, A. H. Westphal, R. Kuhnemuth, H. Hornen, N. V. Visser, S. Kalinin, J. Aker, A. van Hoek, C. A. M. Seidel and A. J. W. G. Visser (2008). Structural changes of yellow cameleon domains observed by quantitative FRET analysis and polarized fluorescence correlation spectroscopy. *Biophys. J.* **95**(11): 5399-5411.

Evers, T. H., E. M. W. M. van Dongen, A. C. Faesen, E. W. Meijer and M. Merkx (2006). Quantitative understanding of the energy transfer between fluorescent proteins connected via flexible peptide linkers. *Biochemistry* **45**(44): 13183-13192.

Förster, T. (1949). Experimentelle und theoretische Untersuchung des zwischenmolekularen Ubergangs von Elektronenanregungsenergie. *Zeitschrift für Naturforschung* **4a**(5): 321-327.

Ganesan, S., S. M. Ameer-Beg, T. T. Ng, B. Vojnovic and F. S. Wouters (2006). A dark yellow fluorescent protein (YFP)-based resonance energy-accepting chromoprotein (REACh) for Förster resonance energy transfer with GFP. *Proc. Natl. Acad. Sci. USA* **103**(11): 4089-94.

Golub, G. and V. Pereyra (2003). Separable nonlinear least squares: the variable projection method and its applications. *Inverse Probl.* **19**(2): R1-R26.

Golub, G. H. and C. F. van Loan (1996). Matrix computations, Johns Hopkins University Press.

Golub, G. H. and V. Pereyra (1973). Differentiation of pseudo-inverses and nonlinear least-squares problems whose variables separate. *Siam J. Numer. Analysis* **10**(2): 413-432.

Grinvald, A., and I. Z. Steinberg. 1974. Analysis of fluorescence decay kinetics by method of least-squares. *Anal. Biochem.* **59**(2):583-598.

Hink, M. A., N. V. Visser, J. W. Borst, A. van Hoek and A. J. W. G. Visser (2003). Practical use of corrected fluorescence excitation and emission spectra of fluorescent proteins in Förster resonance energy transfer (FRET) studies. *J. Fluores.* **13**(2): 185-188.

Hoff, W. D., I. H. van Stokkum, H. J. van Ramesdonk, M. E. van Brederode, A. M. Brouwer, J. C. Fitch, T. E. Meyer, R. van Grondelle and K. J. Hellingwerf (1994). Measurement and global analysis of the absorbance changes in the photocycle of the photoactive yellow protein from Ectothiorhodospira halophila. *Biophys. J.* **67**(4): 1691-1705.

Hyun Bae, J., M. Rubini, G. Jung, G. Wiegand, M. H. J. Seifert, M. K. Azim, J.-S. Kim, A. Zumbusch, T. A. Holak, L. Moroder, R. Huber and N. Budisa (2003). Expansion of the genetic code enables design of a novel “Gold” class of green fluorescent proteins. *J. Mol. Biol.* **328**(5): 1071-1081.

Immink, R. G. H., T. W. J. Gadella, S. Ferrario, M. Busscher and G. C. Angenent (2002). Analysis of MADS box protein-protein interactions in living plant cells. *Proc. Natl. Acad. Sci. USA* **99**(4):2416-2421.

Jares-Erijman, E. A. and T. M. Jovin (2006). Imaging molecular interactions in living cells by FRET microscopy. *Curr. Opin. Chem. Biol.* **10**(5):409-416

Knox, R. S. and H. van Amerongen (2002). Refractive index dependence of the Förster resonance excitation transfer rate. *J. Phys. Chem. B* **106**(20): 5289-5293.

Lakowicz, J. R. (2006). Principles of Fluorescence Spectroscopy 3rd edition, New York, Springer.

Laptenok, S., K. M. Mullen, J. W. Borst, I. H. M. van Stokkum, V. V. Apanasovich and A. J. W. G. Visser (2007). Fluorescence Lifetime Imaging Microscopy (FLIM) data analysis with TIMP. *Journal of Statistical Software* **18**(8).

Maus, M., M. Cotlet, J. Hofkens, T. Gensch, F. C. De Schryver, J. Schaffer and C. A. M. Seidel (2001). An experimental comparison of the maximum likelihood estimation and nonlinear least squares fluorescence lifetime analysis of single molecules. *Anal. Chem.* **73**(9): 2078-2086.

Mullen, K. M., M. Vengris, and I. H. van Stokkum. 2007. Algorithms for separable nonlinear least squares with application to modelling time-resolved spectra. *J. Global Optimization* **38**(2):201-213.

Paul, R. B., M. A.-B. Simon, D. G. Julian, J. E. Richard, E. Ifeome and V. Borivoj (2005). Global and pixel kinetic data analysis for FRET detection by multi-photon time-domain FLIM, SPIE.

Pelet, S., M. Previte, J. R. and T. P. So (2006). Comparing the quantification of Ferster resonance energy transfer measurement accuracies based on intensity, spectral, and lifetime imaging. *J. Biomed. Opt.* **11**(3):034017.

R Development Core Team. (2008). R: a Language and environment for statistical computing. R Foundation for Statistical Computing, Viena. *http://www.R-project.org.*

Shaner, N. C., R. E. Campbell, P. A. Steinbach, B. N. G. Giepmans, A. E. Palmer and R. Y. Tsien (2004). Improved monomeric red, orange and yellow fluorescent proteins derived from Discosoma sp. red fluorescent protein. *Nat Biotech* **22**(12): 1567-1572.

Stryer, L. (1978). Fluorescence energy transfer as a spectroscopic Ruler. *Annu. Rev. Biochem.* **47**(1):819-846.

Tramier, M., I. Gautier, T. Piolot, S. Ravalet, K. Kemnitz, J. Coppey, C. Durieux, V. Mignotte and M. Coppey-Moisan (2002). Picosecond-hetero-FRET microscopy to probe protein-protein interactions in live Cells. *Biophys. J.* **83**(6): 3570-3577.

Tramier, M., M. Zahid, J. C. Mevel, M. J. Masse and M. Coppey-Moisan (2006). Sensitivity of CFP/YFP and GFP/mCherry pairs to donor photobleaching on FRET determination by fluorescence lifetime imaging microscopy in living cells. *Microsc. Res. Techn.* **69**(11): 933-939.

Tsien, R. Y. 1998. The green fluorescent protein. *Annu. Rev. Biochem.* 67(1):509-544.

van Stokkum, I. H. M., D. S. Larsen and R. van Grondelle (2004). "Global and target analysis of time-resolved spectra. *Biochim. Biophys. Acta.* **1657**(2-3): 82-104.

Verveer, P. J., A. Squire and P. I. H. Bastiaens (2000). Global analysis of fluorescence lifetime imaging microscopy data. *Biophys. J.* **78**(4): 2127-2137.

Vojnovic, B. (2007). Application of novel imaging techniques for early clinical trials. *Eur. J Cancer Supplements* **5**(9):19-21.

Vos, K., A. van Hoek and A. J. W. G. Visser (1987). Application of a reference convolution method to tryptophan fluorescence in proteins - a refined description of rotational-dynamics. *Eur. J. Biochem.* **165**(1): 55-63.

Wlodarczyk, J., A. Woehler, F. Kobe, E. Ponimaskin, A. Zeug and E. Neher (2008). Analysis of FRET signals in the presence of free donors and acceptors. *Biophys. J.* **94**(3): 986-1000.

Yan, Y. and G. Marriott (2003). Analysis of protein interactions using fluorescence technologies. *Curr. Opin. Chem. Biol.* **7**(5):635-640.

Chapter 6

Summarizing discussion

Genome sequences collected from various living species do not tell us how the molecular machinery is assembled to living cells and organisms. Imaging specific molecules and their spatio-temporal interactions in an intracellular network may provide a clue to understand how genomes create cells, how cells make organisms and how errant cells cause disease. Many important protein machines and signaling domains have dimensions in the range of 5-500 nm covering the experimental range of optical microscopy. Fluorescence microscopy including the genetically encoded Visible Fluorescent Protein (VFP) technology in particular, has all capabilities for time-lapse registration except that light diffraction limits the spatial resolution to ~250 nm. This is sufficient to observe many features of live cells, but not to disclose structural features of individual biomolecules *in situ*. During the last decade we have observed a revolutionary development in state-of-the-art microspectroscopic techniques, among others Förster Resonance Energy Transfer (FRET) measured in a microscope via Fluorescence Lifetime Imaging Microscopy (FLIM). The applications of these technologies in cell biology have yielded a plethora of novel information on biomolecular interactions and their roles in multiple cellular pathways such as signal transduction networks. However, this is only a first step towards a complete understanding of the regulation of these molecular networks at the level of systems biology. There is a transition occurring in biology from the molecular level to the system level that promises to revolutionize our understanding of complex biological systems (Kitano 2002). We will then be able to understand the mechanisms that systematically control the state of the cell.

Contemporary microspectroscopic experiments are often not sensitive enough to confirm the existence of biomolecular interactions in the cell. Therefore, novel, more sensitive, complementary and faster optical contrast modes are necessary to determine the affinity, competition, dynamics and exact location of protein-protein interactions. The objective is to develop new multidimensional fluorescence analysis methods dedicated to improve the visualization and the quantitative analysis of complex spectral, spatial and time-resolved data sets. Microspectroscopy will then become a platform technology within systems biology.

Combination of cell biology and biophysical techniques is an important step forward for identifying and quantifying biological processes in their natural environment. In particular, FRET methods provide quantitative information about distances (1-10 nm), which are far below the diffraction limit. FRET is a photophysical process, in which the excited-state energy from a donor molecule is transferred non-radiatively to an acceptor molecule at close distance via weak dipole-dipole coupling. FRET is a widely used method for monitoring interactions between or within biological macromolecules conjugated with suitable donor-acceptor pairs. The crucial point in the extraction of information about protein interactions from FRET data is advanced and robust data analysis. This thesis focuses on the study of the application of global and target analysis of FRET phenomena in time-resolved fluorescence techniques obtained with different fluorescence techniques. The global algorithms exploit the knowledge that only a limited number of fluorescent species is present and that some unknown parameters are the same between two or more datasets. Global analysis algorithms fit simultaneously multiple measurements under different experimental conditions thereby recovering the parameters with high accuracy. There are several methods available for quantification of FRET, of which the one based on fluorescence lifetime measurements is the most straightforward method. The fluorescence lifetime is the average time that a molecule remains in the excited state. Donor fluorescence lifetimes in the absence and presence of acceptor molecules are often measured for the observation of FRET. However, these lifetimes may originate from interacting and non-interacting molecules, which hamper quantitative interpretation of FRET data.

The development of biosensors based on FRET technology has provided information about a large variety of biochemical processes. The FRET based calcium sensor Yellow Cameleon 3.60 (YC3.60) has been studied in chapters 2 and 3. YC3.60 changes its conformation upon calcium binding, thereby increasing the FRET efficiency. Most FRET sensors are built like the cameleons, in which two chromophores from a selected FRET pair are coupled with a linker. The composition of the linker defines the specificity of the sensor.

A methodology for the detection of FRET that monitors the rise time of acceptor fluorescence upon donor excitation is described in chapter 2. The large advantage of this method, as compared to more commonly used donor fluorescence quenching methods, is that only those molecules are monitored that are involved in the energy-transfer process. Moreover, the transfer rate of FRET can be accurately determined even in cases where the FRET efficiencies approach 100% yielding highly quenched donor fluorescence. A number of simulation studies has been performed in order to study the effect of cross-talk and presence of the directly excited acceptor in the experimental data on the resolvability of the rise components in the time-dependence of acceptor fluorescence. It is found that the rise components can be retrieved by global analysis even in presence of significant amount of cross-talk and/or presence of the directly excited acceptor. Therefore the estimated rise times of the acceptor were used to calculate distances between chromophores in calcium free and calcium bound conformations of YC3.60. Furthermore, the relative orientation between donor and acceptor chromophores is obtained from time-dependent fluorescence anisotropy measurements performed under identical conditions of donor excitation and acceptor detection. After mapping distances and orientation angles between the FRET moieties in YC3.60, cartoon models of this FRET sensor with and without calcium have been created.

The exact location of the spectral maximum of a fluorescent molecule is dependent on the direct environment. At the same time the fluorescence lifetime is strongly influenced by the environment via electron or proton transfer, variable refractive index changes, excitonic interactions, FRET, etc. The experimental system with femtosecond resolution consisting of a femtosecond laser and a polychromator and synchroscan streak camera in the detection channel is suitable to measure emission intensity across time and wavelength dimensions in a single experiment. The streak images of purified YC3.60 in aqueous solution have been studied in chapter 3. Global target analysis of the images of YC3.60 in calcium-free and calcium-bound conformations yields detailed insight in the kinetics of the FRET process.

Several fluorescence FRET-based sensors have been developed in a recent years. They are used as indicators for a variety of cellular processes. Therefore good analysis protocols for FLIM-FRET image analysis are necessary. FLIM is a widely used imaging technique, which allows the fluorescence lifetime to be imaged at 250 nm spatial resolution and at (sub)nanosecond temporal resolution. Often a small number of kinetic processes underlie the observed fluorescence at all pixels, but the intensity of the fluorescence associated with each process varies per pixel. Then the challenge is a statistical, global analysis of the image: use of the fluorescence decay at all pixels to estimate the lifetimes associated with the kinetic processes, as well as the amplitude of each kinetic process at each location. Given that typical FLIM images represent on the order of 10^3 time points and 10^3 locations, meeting this challenge is computationally intensive. The use of separable nonlinear models and the applicability of the partitioned variable projection algorithm to analyze FLIM data is described in chapter 4. It has been found through a number of simulation studies and control experiments that this approach is promising for modelling FLIM data.

A methodology for the detection of FRET in live cells by monitoring the rise time of the acceptor fluorescence using FLIM is described in chapter 5. The method relies on global analysis of FLIM images. As a result, a more accurate characterization of the amount of FRET occurring in a given system is obtained as compared to more commonly used donor fluorescence quenching methods. The commonly used methods rely on estimation of the decay rate of donor fluorescence, which usually consists of a mixture of the populations of donor molecules that are involved in FRET and those that are fluorescent but not involved in FRET. Alternatively, parameters describing the rise of acceptor fluorescence and the decay of the donor fluorescence can be determined via simultaneous global analysis of multiple FLIM images, thereby increasing the reliability of the analysis. In chapter 5, plant protoplasts transfected with fusions of visible fluorescent proteins are used to illustrate the new data analysis method. It is demonstrated that the distances estimated with the present method are substantially smaller than those estimated from the average donor lifetimes. Although results require further investigation, the experiment demonstrates the possibility of this approach to study FRET in living cells. The methodology seems to be more accurate in estimating donor-acceptor distances, although no one knows beforehand, without structural biology knowledge, what the true donor-acceptor distances are. However, the method does result in distance calculations that are likely to be more precise, because they are consistent with both the rate of donor decay and the rate of acceptor rise. Still, the acceptor and donor fluorescence is measured sequentially from the same cell using the same excitation wavelengths and intensities. Therefore photo-bleaching or photo-activation of VFP's might be an issue in data analysis. It would be much better, if the acceptor rise is simultaneously measured as the donor decay (by splitting the emission light beam in the detection channel and using two detectors, for example).

The major goal of this thesis was to develop an advanced data analysis approach to improve the analysis of complex biological systems studied with time-resolved microspectroscopy techniques. The global and target analysis is dedicated to improve the visualization and the quantitative analysis of complex spectral, spatial and time-resolved data. In general, global and target analysis is capable to obtain model-based description of the data in terms of small number of precisely estimated parameters that mathematically well represent the experimental dataset. However, it is the responsibility of the researcher to discriminate between candidate models. There is no data analysis technique that is suitable to substitute a good understanding of the physical processes underlying the experiment.

Software to reproduce the presented results is provided in an open-source and freely available package called "TIMP" for "The R project for Statistical Computing" (http://timp.r-forge.r-project.org). A Java-based graphical user interface (GUI) for the TIMP package is currently under development (http://timpgui.org). The GUI is meant for simplifying the model specification for global and target analysis of time-resolved microspectroscopy data, improving the interactivity of the analysis and visualization of the results.

References

Kitano, H. (2002). “Systems Biology: A Brief Overview.” *Science* **295**(5560): 1662-1664.

Nederlandse samenvatting

Informatie over het genoom van verschillende organismes geeft niet direct inzicht in hoe de moleculaire machines van het leven geassembleerd worden tot levende cellen en organismes. Het meten van specifieke moleculen en hun spatiële en temporele interacties in een intercellulaire netwerk geeft wellicht aanwijzingen hoe cellen organismes kunnen maken en hoe defecte cellen ziektes veroorzaken. Veel belangrijke eiwit machines en signaal domeinen hebben dimensies in het gebied tussen de 5 en 500 nm, hetgeen deels binnen het bereik van de experimentele optische microscopie valt. Fluorescentie microscopie, in het bijzonder de “genetically encoded Visible Fluorescent Protein (VFP)” technologie, heeft al mogelijkheden voor tijdsopgeloste registratie, behalve dat de spatiële resolutie tot ca. 250 nm beperkt blijft. Dit is genoeg om de meeste kenmerken van levende cellen waar te nemen, maar niet genoeg om de structurele kenmerken te ontsluiten of de individuele biomoleculen in situ te bestuderen.

Gedurende de laatste eeuw hebben we een revolutionaire ontwikkeling van state-of-the-art microscopie technieken kunnen zien, waaronder ook Förster Resonance Energy Transfer (FRET) gemeten in een microscoop middels Fluorescence Lifetime Imaging Microscopy (FLIM). De toepassingen van deze technologieën in celbiologie hebben een overvloed aan nieuwe informatie opgeleverd over biomoleculaire interacties en hun rol in meervoudige cellulaire interactieroutes zoals die van signaal transductie. Echter, dit is pas de eerste stap naar een volledig begrip hoe deze moleculaire netwerken werken en gereguleerd worden op het niveau van de systeembiologie. Er vindt een verschuiving plaats binnen de biologie van het moleculaire niveau naar het systeem niveau hetgeen mogelijk tot een revolutie kan leiden bij het begrijpen van complexe biologische systemen (Kitano 2002). Dit zal ons in staat stellen om de mechanismes te begrijpen die de toestand van de cel controleren.

Hedendaagse microscopische experimenten zijn vakk niet voldoende gevoelig om het bestaan van biomoleculaire interacties aan te tonen binnen de cel. Daarom zijn er nieuwe, meer gevoelige, aanvullende en snellere optische contrast methodes nodig om de affiniteit, competitie, dynamica en de exacte locatie van eiwit-eiwit interacties te bepalen. Het doel is om nieuwe multidimensionale fluorescentie analyse methodes te ontwikkelen, bij uitstek geschikt voor de visualisatie en de kwantitatieve analyse van complexe spectrale, ruimtelijke en tijdsopgeloste datasets.

De combinatie van cel biologie en biofysische technieken is een belangrijke stap in het identificeren en kwantificeren van biologische processen in hun natuurlijke omgeving. In het bijzonder leveren op FRET gebaseerde methodes kwantitatieve informatie over afstanden (1-10nm), welke ver onder de diffractie limiet zitten. FRET is een fotofysisch proces, waarbij de energie van de aangeslagen toestand van een donor molecuul stralingsloos wordt overgedragen naar een acceptor molecuul via de zwakke dipool-dipool koppeling. FRET is een veel gebruikte methode om de interacties tussen of binnen biologische macromoleculen die verbonden zijn met geschikte donor-acceptor paren te volgen.

De extractie van informatie over eitwit interacties middels FRET vereist een geavanceerde en robuuste data analyse. Dit proefschrift richt zich op de studie van de toepassing van globale en target analyse van FRET resultaten verkregen middels diverse tijdsopgeloste fluorescentie technieken. Het globale algoritme gebruikt het gegeven dat slechts een beperkt aantal fluorescentie componenten aanwezig is en dat enkele onbekende parameters hetzelfde zijn in twee of meer datasets. Globale analyse algoritmes fitten simultaan verschillende metingen onder verschillende experimentele condities, waarbij de onderliggende parameters met hoge nauwkeurigheid worden bepaald. Er zijn verschillende methodes beschikbaar voor het kwantificeren van FRET, waarbij de methode gebaseerd op de fluorescentie levensduur de meest recht-toe-recht-aan methode is. De fluorescentie levensduur is de gemiddelde tijd dat een molecuul zich in de aangeslagen toestand bevindt. Donor fluorescentie levensduren in de aan- en afwezigheid van acceptor moleculen worden vaak gemeten voor de bepaling van FRET. Echter, deze levensduren kunnen zowel afkomstig zijn van moleculen die wel interactie vertonen als van moleculen die geen interactie vertonen, hetgeen de kwantitatieve interpretatie van FRET data zal beïnvloeden.

De ontwikkeling van biosensoren gebaseerd op FRET technologie heeft informatie opgeleverd over de werking van een grote variëteit aan biochemische processen. De op FRET gebaseerde calcium sensor Yellow Cameleon 3.60 (YC3.60) wordt in de hoofdstukken 2 en 3 behandeld. YC3.60 verandert van conformatie wanneer het zich bindt aan calcium, waarbij de FRET efficiëntie toeneemt. De meeste FRET sensoren zijn geconstrueerd zoals de cameleons, waarin 2 chromoforen van een geselecteerd FRET-paar gekoppeld zijn via een linker. De compositie van de linker bepaalt de specificiteit van de sensor.

Een methode om FRET te detecteren door het bepalen van de stijgtijd van de acceptor fluorescentie na donor excitatie wordt beschreven in hoofdstuk 2. Het grote voordeel van deze methode, vergeleken met de meer gebruikte donor fluorescentie dovings methodes, is dat alleen die moleculen gevolgd worden die daadwerkelijk betrokken zijn bij het energie-overdracht proces. Verder kan de mate van overdracht van FRET nauwkeurig worden bepaald, zelfs in die gevallen waar de FRET efficiëntie de 100% benadert, hetgeen leidt tot een hoge mate van doving van de donor fluorescentie. Diverse simulatie studies zijn uitgevoerd om het effect te bestuderen van “cross-talk” en de aanwezigheid van direct aangeslagen acceptor moleculen op de mogelijkheid om de stijgende componenten te extraheren uit de acceptor fluorescentie. Er is gevonden dat de fluorescentie stijgtijd kan worden achterhaald middels globale analyse, zelfs in de aanwezigheid van een significante hoeveelheid cross-talk en/of de aanwezigheid van een direct aangeslagen acceptor moleculen. Daardoor kunnen de geschatte stijgtijden van de acceptor fluorescentie worden gebruikt om de afstanden tussen chromoforen in YC3.60 te bepalen in de aan- en afwezigheid van gebonden calcium. Verder kan de relatieve oriëntatie tussen donor en acceptor chromoforen worden afgeleid uit de tijdsafhankelijke fluorescentie anisotropie metingen. Gebruikmakend van geschatte afstanden en oriëntaties tussen de FRET chromoforen in YC3.60 zijn er cartoon modellen van deze FRET sensor met en zonder calcium geconstrueerd.

De exacte locatie van het spectrale maximum van een fluorescerend molecuul is afhankelijk van de direct omgeving. Tegelijkertijd wordt de fluorescentie levensduur sterk beïnvloed door de omgeving via electron of proton overdracht, veranderingen in de brekingsindex, exciton interacties, FRET, etc. De gebruikte experimentele opstelling, bestaande uit een femtoseconde laser, een polychromator en een synchroscan streak camera, is geschikt om in een enkel experiment met (sub)picoseconde tijdsresolutie de verandering in fluorescentiespectra te registreren na excitatie met een femtoseconde laserpuls.

De steak camera afbeeldingen van gezuiverd YC3.60 in een waterige oplossing zijn bestudeerd in hoofdstuk 2. Globale target analyse van de afbeeldingen van YC3.60 in calcium-vrije en een calcium-gebonden conformatie geven gedetailleerd inzicht in de kinetiek van het FRET proces.

Gedurende de laatste jaren zijn er verschillende op FRET-gebaseerde sensoren ontwikkeld. Ze worden gebruikt als indicatoren voor een scala aan cellulaire processen. Daarom zijn goede analyse protocollen voor FLIM-FRET analyse noodzakelijk. FLIM is een veelgebruikte "imaging" techniek, waarmee het mogelijk is om de fluorescentie levensduur te "imagen" met 250 nm ruimtelijke resolutie en (sub)nanoseconde tijdsresolutie. Vaak liggen er slechts een klein aantal kinetische processen ten grondslag aan de fluorescentie. Dit resulteert in een verschillende fluorescentielevensduren waarbij de bijbehorende amplitudo's kunnen variëren van pixel tot pixel. De uitdaging bestaat er dan uit om met behulp van een globale analyse van de afbeelding, de levensduren te bepalen die geassocieerd zijn met de onderliggende kinetische processen, evenals de amplitudo's van elk kinetisch proces op elke locatie. Gegeven het feit dat typische FLIM afbeeldingen circa 103 tijdspunten en 103 plaatspunten bevat kan deze analyse zeer rekenintensief zijn. Het gebruik van niet-lineaire modellen en de toepasbaarheid van het gepartitioneerde variabele-projectie algoritme om FLIM data te analyseren wordt beschreven in hoofdstuk 4. Door het uitvoeren van een aantal simulatie studies en controle experimenten is gevonden dat deze aanpak zeer veelbelovend is voor het modelleren van FLIM data.

Een methode voor de detectie van FRET in levende cellen door het observeren van de stijgtijd van de acceptor fluoresentie middels FLIM is beschreven in hoofdstuk 5. Deze methode berust op de globale analyse van FLIM afbeeldingen en verschaft een meer nauwkeurige bepaling van de hoeveelheid FRET die plaatsvindt in een gegeven systeem dan de tot nu toe meer gebruikte donor fluorescentie-doving methode. Deze laatste methode gebruikt de mate van verval van de donor fluorescentie, welke normaal gesproken bestaat uit een mix van de populaties van de donor moleculen die betrokken zijn bij het FRET proces en die moleculen die fluoresceren maar niet betrokken zijn bij het FRET proces.

Als alternatief kunnen parameters die de stijging van de acceptor fluorescentie en het verval van de donor fluorescentie bepalen, worden verkregen via simultane globale analyse van verschillende FLIM afbeeldingen, waardoor de betrouwbaarheid van de analyse toeneemt. In hoofdstuk 5 worden plant protoplasten getransfecteerd met fluorescerende eiwitten om deze nieuwe data analyse methode te illustreren. Er wordt aangetoond dat de afstanden die geschat worden met de nieuwe analysemethode substantieel kleiner zijn dan die welke geschat worden op grond van de gemiddelde levensduren van de donor fluorescentie.

Alhoewel verder onderzoek vereist is, toont dit experiment wel de mogelijkheid aan om met deze aanpak FRET in levende cellen te bestuderen. De gebruikte methodologie lijkt nauwkeuriger te zijn voor het schatten van donor-acceptor afstanden. Wel moet de kanttkening gemaakt worden dat de acceptor en donor fluorescentie sequentieel worden gemeten. Daardoor kan "photobleaching" van VFP's wellicht een probleem vormen. Het zou veel beter zijn wanneer de acceptor stijgtijd tegelijkertijd zou worden gemeten met de donor vervaltijd.

Het hoofddoel van dit proefschrift was om een geavanceerde methode te ontwikkelen om de analyse van complexe biologische systemen, bestudeerd met tijdsopgeloste microscopische technieken, te verbeteren. De globale en target analyse is er op gericht om de visualisatie en de kwantitatieve analyse van complexe spectrale-, spatiële- en tijds-opgeloste data te verbeteren. In het algemeen is de globale en target analyse in staat om een model-gebaseerde beschrijving van de data te geven in termen van een klein aantal precies geschatte parameters die de experimentele data goed representeren. Echter, het is en blijft de verantwoordelijkheid van de onderzoeker om onderscheid te maken tussen verschillende kandidaat modellen. Er is geen enkele data analyse techniek die geschikt is om een goed begrip van de fysiche processen die ten grondslag liggen aan het experiment te vervangen.

Software om de gepresenteerde resultaten te reproduceren wordt aangeboden in een open-source en vrij te verkrijgen pakket genaamd "TIMP" voor The R project for Statistical Computing" (http://timp.r-forge.r-project.org). Een Java-gebaseerde graphical user interface (GUI) is momenteel onder ontwikkeling (http://timpgui.org). De GUI is bedoel om de model specificatie te versimpelen voor globale en target analyse van tijdsopgeloste microscopische data, om zo de interactiviteit van de analyse en visualisatie van de resultaten te verbeteren.

References

Kitano, H. (2002). "Systems Biology: A Brief Overview." *Science* **295**(5560): 1662-1664.

Acknowledgements

This dissertation represents the result of several years of work. Obviously these results would never have been reached without the assistance of other people. Therefore I would like to thank all of the people who make this thesis possible.

First of all I would like to thank my supervisors Ton Visser and Herbert van Amerongen. Very few times in life is it possible to find such a combination of professional capacity and human quality. Thank you for always finding time to discuss things. I am also very grateful to my supervisor at the department of System Analysis in Belarusian State university, Vladimir V. Apanasovich, who helped me to start the project, and who was always ready to help in any situation.

Many thanks to Jan Willem Borst and Ivo van Stokkum for their feedback and guidance. You were always ready to discuss any topic. I will always remember our discussions, from which I got more knowledge than from any book. It was pleasure to work under yours supervision.

Rob Koehorst, Arie van Hoek, and Adrie Westphal, I've learned a lot from you about fluorescence, photo-physical and photo-chemical processes. You was always helpful with any technical questions. Frank de Weerd, thanks for always been ready to help with any computer problems.

I also want to thank Netty Hoefackker and Laura van Egmond, secretaries of the Biophysics and Biochemistry groups. With your support all bureaucratic issues became much easier.

Bart van Oort, thank you for always been very helpful. I enjoyed our scientific and general discussions no matter where we had them, from in a basement during fights with a streak camera, or in the pub having a nice beer.

Sashka Krumova, it was great to be you office-mate and friend. I wish you all the best in you life and career.

Kate Mullen thanks for introducing me to the world of R. I was really pleased with our meetings and discussions during developing TIMP. I'm sure that TIMP will become a widely used tool for data analysis.

A special thanks to Joris Snellenburg for all his efforts in translating the summary of my thesis in to Dutch.

I'm grateful to all colleagues from Biophysics and Biochemistry groups of Wageningen university and in the department of System Analysis in Belarusian State university for being great co-workers and creating a fantastic atmosphere for work.

I was fortunate to make a lot of new friends during my stay in Wageningen. Masha, Natasha, Petia, Katia, one more Petia, Lesha, Kazbek, Lena, Sergey, Ania, Magda, Justin, Marjon, Bart and many more. Thanks for the great times, diners, parties and fun we had during this years. I hope this friendship will continue in future years. A special thanks for Nicky. You always have good wine in your "wine-cellar" and you are always ready to receive guests. Thanks for the nice time we spent in your place having BBQ on the balcony and tasting wines. Yura and Ronald you were always ready to join for a pint of Guinness and not only Guinness.

I will never forget our football team CCCP. Sasha, Ilya, Yura, Bahtior, Antanas, Dima, another Ilya, Roman and everybody who ever joined our team it was pleasure to play with all of you. Thanks to all members of Wageningen floorball club "Stick Together" for fantastic games and time we spent together. Sasha and Ilya, we had a great experience and a lot of fun organizing Russian parties in "International club".

Thanks to all crew in the best pub of Wageningen "De Vlaamsche Reus" for a great time, nice beers and all of the inspiration I got in your place.

My warmest thanks goes to my family, and in particular to my father Piotr Laptenok, my mother Irina Laptenok and my younger sister Olga Laptenok. This thesis would never have been possible without them.

The last but not least words of thanks are to my wife, Dasha. Dasha I'm very happy that we found each other. Without you, writing this thesis would be million times harder. Thanks for your support, love and understanding.

Sergey P. Laptenok
Wageningen, 2009

Curriculum Vitae

Sergey Laptenok was born on the 16th of August 1981 in Bobruisk, Belarus. His elementary studies were completed at the Lyceum of Belarusian State University (Minsk) in 1998.

After following the undergraduate studies in the Belarusian State University in the period 1998-2003, he graduated from the faculty of Radiophysics and Electronics with qualification Radiophysicist. In the last year of his university studies he has completed his diploma work entitled: "Development of methods, algorithms and software tools for wavelet based signature verification."

In 2004 he received his M.Sc. degree at the department of System Analysis, Belarusian State University with a master thesis entitled "Computer simulation of rotational diffusion for complex molecules and molecular aggregates in solutions".

In November 2004 he started his Ph.D. study at the laboratories of Biophysics and Biochemistry, Wageningen University, as a sandwich PhD-fellow under the supervision of Prof. Dr. H. van Amerongen, Prof. Dr. A.J.W.G. Visser and Prof. Dr. V.V. Apanasovich. His research focused on the development of new multidimensional fluorescence analysis methods dedicated to improve the visualization and quantitative analysis and physical interpretation of complex spectral, spatial and time-resolved data sets.

During his doctoral study he has attended a variety of international meetings and in-depth courses.

The Ph.D. project finished in June 2009.

Overview of completed training activities

Discipline specific activities

Courses

Biophysical imaging Wageningen UR	2005
International advanced course Bio-nanotechnology, VLAG Wageningen UR	2005, 2006
Inter-University Course Photophysics, Photochemistry and Photobiology, HRSMC Amstrdam VU	2007
Time resolved microspectroscopy in the life sciences Wageningen UR	2008
International School-Seminar “Spectroscopy of molecules and crystals” Kiev, Ukraine	2005
Caput Series “Structure and dynamics of biomolecules in vitro and in vivo” Wageningen UR	2006

Meetings

Modern methods in computational chemistry, Synthetic Organic Chemistry and fluorescence Spectroscopy, Prague, Czech Republic	2008
Midterm meeting Marie Curie Research Training Network “From FLIM to FLIN Edinburg UK	2008
The R User Conference “Use R! 2008” Dortmund, Germany	2008
EPW Lunteren meeting	2008

General courses

PhD course “Philosophy and Methodology of Science” Belarusian State University, Minsk.	2006-2007

Optionals

Seminar series, Laboratory of Biochemistry Wageningen UR	2004-2005
Seminar series, Laboratory of Biophysics Wageningen UR	2006-2008
Seminar series, Department of system analysis Faculty of Radiophysics and Electronics, Belarusian State University	2005-2007
Farewell Symposium Antonie J.W.G. Visser “Microspectroscopy in Biology”	2008

Cover design by Yury Tikunov

Printed by Wöhrmann Print Service, Zutphen